

**Numerical investigations of bio-inspired blade designs to reduce broadband noise in aircraft
engines and wind turbines**

by

Andrew Lee Bodling

A dissertation submitted to the graduate faculty
in partial fulfillment of the requirements for the degree of
DOCTOR OF PHILOSOPHY

Co-majors: Aerospace Engineering; Wind Energy Science, Engineering and Policy

Program of Study Committee:
Anupam Sharma, Major Professor
Alberto Passalacqua
Leifur Leifsson
Alric Rothmayer
Partha Sarkar

The student author, whose presentation of the scholarship herein was approved by the program of study committee, is solely responsible for the content of this dissertation. The Graduate College will ensure this dissertation is globally accessible and will not permit alterations after a degree is conferred.

Iowa State University

Ames, Iowa

2019

Copyright © Andrew Lee Bodling, 2019. All rights reserved.

TABLE OF CONTENTS

LIST OF TABLES	vi
LIST OF FIGURES	vii
ABSTRACT	xvii
CHAPTER 1. INTRODUCTION	1
CHAPTER 2. NUMERICAL INVESTIGATION OF NOISE REDUCTION MECHANISMS IN A BIO-INSPIRED AIRFOIL	9
2.1 Introduction	10
2.2 Numerical Methodology	12
2.3 Geometry Modeling, Meshing, and Boundary Conditions	13
2.3.1 Baseline Airfoil Mesh	14
2.3.2 Finlet Fence Geometry and Mesh	15
2.3.3 Boundary Layer Trip	16
2.3.4 Removal of Transients	17
2.4 Results	18
2.4.1 Baseline Validation	18
2.4.2 Surface Pressure Spectra	21
2.4.3 Far field Aeroacoustics	22
2.4.4 Noise Reduction Mechanisms	26
2.5 Conclusions	30
CHAPTER 3. NUMERICAL INVESTIGATION OF LOW-NOISE AIRFOILS INSPIRED BY THE DOWN COAT OF OWLS	33
3.1 Introduction	34

3.2 Numerical Methodology	38
3.2.1 Compressible Flow Solver	38
3.2.2 Prediction of Farfield Noise	40
3.2.3 Kato's Correction	40
3.3 Geometry Modeling, Meshing, and Boundary Conditions	41
3.3.1 Baseline Airfoil Mesh	42
3.3.2 Finlet Fence Geometry and Mesh	42
3.3.3 Boundary Layer Trip	46
3.3.4 Removal of Transients	47
3.4 Results	47
3.4.1 Baseline Validation	47
3.4.2 Aerodynamic Performance	51
3.4.3 Aeroacoustic Performance	53
3.4.4 Noise Reduction Mechanisms	57
3.5 Conclusions	66
CHAPTER 4. NUMERICAL INVESTIGATION OF BIO-INSPIRED FINLETS FOR THE REDUCTION OF AIRCRAFT AND WIND TURBINE NOISE	69
4.1 Introduction	70
4.2 Numerical Methodology	72
4.3 Geometry Modeling, Meshing, and Boundary Conditions	72
4.3.1 Baseline Airfoil Mesh and Spatial Resolution Study	73
4.3.2 Finlet Fence Geometry and Mesh	75
4.3.3 Boundary Layer Trip	78
4.4 Results	80
4.4.1 Baseline Validation	81
4.4.2 Baseline and Fence Aerodynamic Comparison	85
4.4.3 Baseline and Fence Aeroacoustic Comparison	89
4.4.4 Noise Reduction Mechanisms	91
4.5 Conclusions	100

CHAPTER 5. CONCLUSIONS AND FUTURE WORK	104
5.1 Conclusions	104
5.2 Future Work	107
BIBLIOGRAPHY	109
ACKNOWLEDGEMENTS	116
APPENDIX A. HIGH ORDER FILTERING AND COMPACT FINITE DIFFERENCING IN FDL3DI	117
A.1 Theory and Implementation of Filtering Schemes	117
A.1.1 Spectral Function of the Interior Filters	117
A.1.2 Derivation of the Coefficients of the Interior Filters	119
A.1.3 Spectral Response of the Interior Filters	120
A.1.4 Spectral Function of the Boundary Filters	122
A.1.5 Derivation of the Boundary Filter Coefficients	123
A.1.6 Spectral Response of the Near-Boundary Filters	124
A.2 Compact Finite Differencing Derivations	126
A.2.1 Boundary Point Finite Difference Scheme	126
A.2.2 Interior Point Finite Difference Scheme	131
APPENDIX B. VERIFICATION OF ACOUSTICS SOLVER	133
APPENDIX C. FILTERING ALGORITHM NEAR FENCE BOUDNARIES	138

LIST OF TABLES

Table 2.1	Baseline grid metrics	15
Table 3.1	The baseline grid dimensions and non-dimensional cell sizes in wall units. Average and max values are obtained over the turbulent flow region.	42
Table 3.2	Drag coefficient (C_D) comparisons between the baseline and fence simulations	53
Table 3.3	Difference in L_{pb} between baseline and fences at $\theta = 90^\circ$	57
Table 3.4	Difference in L_{pb} between baseline and fences at $\theta = 45^\circ$	57
Table 3.5	Difference in L_{pb} between baseline and fences at $\theta = 135^\circ$	57
Table 3.6	Difference in L_{pb} between baseline and fences after integrating over all azimuth angles.	58
Table 4.1	The baseline nested O-grid dimensions and spatial extent.	73
Table 4.2	The baseline grid dimensions and non-dimensional cell sizes in wall units for the coarse, medium and fine inner-most grid block. Average and max values are obtained over the turbulent flow region.	75
Table 4.3	Drag (C_D) and lift (C_L) coefficient comparisons between the baseline and fence simulations.	88
Table 4.4	Drag (C_D) and lift (C_L) coefficient comparisons between the baseline and fence experiment from Clark [1].	88

LIST OF FIGURES

Figure 1.1	Chord based Reynolds number (Re_c) of various species compared with different aircraft	2
Figure 1.2	The owl hush kit: unique feather adaptations that enable the owl to fly silently. Top: barn owl wing specimen. Bottom: Photographs through a microscope of (a) leading edge comb, (b) downy coat on flight feathers, and (c) trailing edge fringe. Images (b) and (c) are from Refs. [2, 3].	3
Figure 1.3	Idealized representations of the a) finlet fence and b) finlet rail designs which were experimentally investigated in Ref. [4]. The struts to support the finlet rails are omitted for clarity.	5
Figure 2.1	Idealized schematics of the two finlet designs used by Clark <i>et al.</i> [4].	11
Figure 2.2	Schematics highlighting the differences in the fence geometries between the experiments and the current simulations.	12
Figure 2.3	The O-grid topology used in the simulations; shown here for the baseline airfoil. The trailing edge is rounded and the mesh near the TE ($0.90 \leq x/c \leq 1.04$) is shown in (b). Every third point along each axis is shown for clarity.	15
Figure 2.4	Cross-sectional (zoom) views ($0.861 \leq x/c \leq 1.005$) of the computational meshes used to simulate the single-step and stair-step fence geometries. Every other grid point along each axis is shown for clarity.	17
Figure 2.5	Top views ($0.865 \leq x/c \leq 0.885$) of the baseline and single-step fence meshes. Each fence element is modeled to be two cells thick in the simulations.	18

Figure 2.6	Mesh points that are blanked out to simulate the boundary layer trip wires (locations indicated with red squares in (a)). The nodes adjacent to the blanked-out points are assigned the no-slip wall boundary condition. The trip is applied across the entire length of the airfoil.	19
Figure 2.7	Iso-surfaces of the Q-criterion ($Q = 10$) of forced boundary layer transition from the geometry-resolved trip wire.	20
Figure 2.8	Time- and span-averaged C_p and C_f distributions from FDL3DI predictions ($Re_c = 5 \times 10^5$) compared with experiments ($Re_c = 4 \times 10^5$ and 2.9×10^6) and XFOIL simulations ($Re_c = 5 \times 10^5$).	21
Figure 2.9	Baseline mean velocity profiles normalized by friction velocity plotted in wall units at different chord locations. Measurements are from Lee and Kang [5]. . .	22
Figure 2.10	Comparison of FDL3DI predictions of normalized Reynolds stresses for the baseline airfoil with DNS results of a turbulent boundary layer in an adverse pressure gradient from Spalart and Watmuff [6], and an LES of a NACA 0012 at $Re = 4 \times 10^5$, $\alpha = 0^\circ$ from Wolf and Lele [7].	23
Figure 2.11	Spanwise coherence squared (γ^2) on the upper surface of the baseline airfoil at $x/c = 0.794$, 904, and 0.994 for $f = 500$, 2500, and 5000 Hz.	24
Figure 2.12	Qualitative comparison between the predicted and measured surface pressure spectra at the trailing edge $x/c = 0.975$. Measurements are from Ref. [1].	25
Figure 2.13	Fluid dilatation contours for the baseline simulation. The FWH integration surface is marked with the red curve. Observer angle (θ) is measured from downstream.	26
Figure 2.14	The shear layer behind the trip wire visualized using contours of vorticity magnitude.	26
Figure 2.15	Qualitative comparison between the FDL3DI predicted and measured farfield noise spectra at an observer located at $\theta = 90^\circ$	27
Figure 2.16	Contours of $C_{p,\text{rms}}$ on a cross-stream plane immediately upstream of the fence leading edge ($x/c = 0.87$).	27

Figure 2.17 Comparison of unsteady surface pressure spectra at $x/c = 0.87$ between the baseline, single-step fence, and stair-step fence. The spectra has been averaged over the span.	28
Figure 2.18 Normalized turbulent kinetic energy (k/u_τ^2) contours for the baseline, single-step fence, and stair-step fence simulations at $x/c = 0.85$ (upstream of the fence).	29
Figure 2.19 Normalized turbulent kinetic energy (k/u_τ^2) contours for the baseline, single-step fence, and stair-step fence simulations at $x/c = 0.975$ near the airfoil trailing edge.	29
Figure 2.20 Span-averaged normalized turbulent kinetic energy (k/u_τ^2) profiles compared between the baseline and fence simulations: (a) upstream of the fence at $x/c = 0.85$, and (b) near the airfoil trailing edge at $x/c = 0.975$	30
Figure 2.21 Spanwise coherence, $\gamma^2(\omega)$ of unsteady surface pressure at the trailing edge $x/c = 0.97$ for a) low, and b) high frequencies.	31
Figure 2.22 Measured farfield noise spectra from Clark <i>et al.</i> [4] showing the effect of fence spacing. For all cases, the maximum height of the fences, $H = 4$ mm.	32
Figure 3.1 Idealized representations of the a) finlet fence and b) finlet rail designs which were experimentally investigated in Ref. [4]. The struts to support the finlet rails are omitted for clarity.	36
Figure 3.2 Geometry of the two fence configurations used in the simulations with maximum normalized fence heights, H/δ^* = a) 1.0 and b) 2.26. The maximum fence height occurs at $x/c = 0.971$	38
Figure 3.3 O-grid topology of the baseline mesh used in the simulation. The trailing edge is rounded and the mesh near the TE is shown in (b). Every fourth point along each axis is shown for clarity.	43
Figure 3.4 Schematic of the fence geometry as modeled: P is the fence pitch, d is fence thickness, c is airfoil chord length, and S is the airfoil span.	44

Figure 3.5	Cross-sectional (zoom) views of the computational meshes used to simulate the $H/\delta^* = 1.0$ and $H/\delta^* = 2.26$ stair-step fence geometries. Every other grid point along each axis is shown for clarity.	45
Figure 3.6	Top views of the baseline and fence meshes (the two fence meshes are identical from the top view). Each fence element is modeled to be two-cell thick in the simulations.	46
Figure 3.7	Time- and span-averaged C_p and C_f distributions from FDL3DI predictions ($Re_c = 5 \times 10^5$) compared with experiments ($Re_c = 4 \times 10^5$ & $Re_c = 2.9 \times 10^6$) and XFOIL simulations ($Re_c = 5 \times 10^5$).	48
Figure 3.8	Predicted span-averaged surface pressure spectrum for the baseline airfoil at $x/c = 0.98$; the spectrum is normalized by the inner variables.	49
Figure 3.9	Baseline time- and span-averaged velocity profile comparisons of the current LES predictions and experiment from a) Lee and Kang [5] and b) Sagrado <i>et al.</i> [8].	50
Figure 3.10	Baseline time- and span-averaged velocity and turbulence intensity comparisons of the simulation and experiment from Sagrado <i>et al.</i> [8] at $x/c = 1.02$. . .	50
Figure 3.11	Baseline time- and span-averaged velocity and turbulence intensity comparisons of the simulation and experiment from Sagrado <i>et al.</i> [8] at $x/c = 1.05$. . .	51
Figure 3.12	Time- and span-averaged C_p and C_f distributions compared between the baseline and the two fence simulations.	52
Figure 3.13	Predicted wall-normal velocity profiles at $x/c = 0.975$. The profiles are averaged over the span. The horizontal dashed lines represent the top of the fences. .	52
Figure 3.14	Azimuthal angle, θ measured from downstream. The origin of the coordinate system is at the airfoil trailing edge.	54
Figure 3.15	Predicted farfield noise spectra at an observer located at $\theta = 90^\circ$	54
Figure 3.16	Measured farfield sound spectra from Clark <i>et al.</i> [4]. The nondimensional fence pitch, $P/\delta^* = 0.69$ in the experiment.	55
Figure 3.17	Predicted farfield noise spectra at observer locations: a) $\theta = 45^\circ$ and b) $\theta = 135^\circ$. .	56

Figure 3.18 Normalized turbulent kinetic energy, TKE/u_τ^2 at $x/c = 0.975$ for a) baseline, b) $H/\delta^* = 1.0$ fence, and c) $H/\delta^* = 2.26$ fence	58
Figure 3.19 Predicted normalized turbulent kinetic energy, TKE/u_τ^2 profiles at $x/c = 0.975$. The profiles are averaged over the span. The horizontal dashed lines represent the location of the top of the fences.	59
Figure 3.20 Measured profiles of u_{rms}/U_∞ from the flat plate experiment by Afshari <i>et al.</i> [9]. The profiles are measured downstream of the fences. The horizontal dashed lines represent the maximum height of the fences.	60
Figure 3.21 Qualitative comparison between the predicted and measured surface pressure spectra near the airfoil trailing edge ($x/c = 0.975$). Measured data is from Clark [1] with a scaled fence pitch $P/\delta^* = 0.77$	61
Figure 3.22 Measured surface pressure spectra from Afshari <i>et al.</i> [9]. The profiles are mea- sured downstream of the fences. Measurements are for a nondimensional fence pitch, $P/\delta^* =$ a) 0.30 and b) 1.03.	62
Figure 3.23 FDL3DI predicted velocity fluctuation spectra in the a) vertical and b) hori- zontal directions within the viscous sublayer ($y/\delta^* = 0.045$) at the trailing edge $x/c = 0.975$. Predictions are averaged along the span with the points within the fences removed from the averaging procedure.	63
Figure 3.24 Spanwise coherence, $\gamma^2(\omega)$ of unsteady surface pressure at the trailing edge $x/c = 0.975$ for a) low, and b) high frequencies.	65
Figure 3.25 Measured farfield noise spectra from Clark <i>et al.</i> [4] showing the effect of fence spacing. For all cases, the normalized maximum height of the fences, $H/\delta^* =$ 0.62 on the suction side.	65
Figure 3.26 A schematic illustrating the effect of increasing the maximum fence height on the angle between the oncoming boundary layer turbulence wavenumber vec- tor (\vec{k}) and the fence normal (\hat{e}_n). Highest sound radiation from the fence edge would occur when \vec{k} and \hat{e}_n are parallel.	66
Figure 4.1 Idealized schematics of the two finlet designs used by Clark <i>et al.</i> [4].	71

Figure 4.2	The O-grid topology used in the simulations; shown here for the baseline airfoil. The trailing edge is rounded and the mesh near the TE ($0.90 \leq x/c \leq 1.04$) is shown in (b). Every third point along each axis is shown for clarity.	73
Figure 4.3	The nested O-grid topology used in the simulations.	74
Figure 4.4	Time- and span-averaged (a) x^+ and (b) y^+ distributions using three different spatial resolutions.	75
Figure 4.5	Time- and span-averaged C_p distributions on baseline airfoil using three different spatial resolutions.	76
Figure 4.6	Time- and span-averaged C_f distributions on (a) pressure side and (b) suction side of baseline airfoil using three different spatial resolutions.	77
Figure 4.7	Schematics highlighting the differences in the fence geometries between the experiments and the current simulations.	78
Figure 4.8	Schematic of the fence geometry as modeled: P is the fence pitch, d is fence thickness, c is airfoil chord length, and S is the airfoil span.	78
Figure 4.9	Cross-sectional (zoom) views of the computational meshes used to simulate the fence geometry. Every other grid point along the radial axis and every 3rd point along the circumferential axis is shown for clarity. Fence meshes for thin and thick fence are identical from the side.	79
Figure 4.10	Top views of the (a) baseline (b) thin and (c) thick fence meshes. The thin and thick fences are 2 and 4-cells thick, respectively, in the simulations.	80
Figure 4.11	Iso-surfaces of the Q-criterion ($Q = 10$) for the unsteady tangential reverse blowing boundary layer tripping mechanism.	81
Figure 4.12	Time- and span-averaged C_p and C_f distributions from FDL3DI predictions ($Re_c = 6 \times 10^5$) compared with experiments ($Re_c = 2.5 \times 10^6$) and XFOIL simulations ($Re_c = 6 \times 10^5$).	83
Figure 4.13	XFOIL predictions ($Re_c = 2.5 \times 10^5$) compared with experiments ($Re_c = 2.5 \times 10^6$) for both natural and forced transition.	84
Figure 4.14	Baseline time- and span-averaged velocity profiles compared with the expected trends in the near-wall and log-law regions.	84

Figure 4.15 Comparison of FDL3DI predictions of normalized Reynolds stresses for the baseline airfoil with DNS results of a turbulent boundary layer in an adverse pressure gradient from Spalart and Watmuff [6]. The Reynolds stresses are at an x location corresponding to $\beta = 1$	85
Figure 4.16 Predicted span-averaged surface pressure spectrum for the baseline airfoil at $x/c = 0.99$ on the suction side for two different time-steps; the spectrum is normalized by the inner variables.	86
Figure 4.17 Low frequency ($f = 543$ Hz) γ^2 along chordwise direction on suction side.	86
Figure 4.18 Spanwise coherence squared (γ^2) on the a) pressure and b) suction surface of the baseline airfoil at $x/c = 0.70, 90$, and 0.99 for $f = 500, 2500$ and 5000 Hz.	87
Figure 4.19 Time- and span-averaged C_p distributions for the baseline and fence geometry from a) FDL3DI predictions ($Re_c = 6 \times 10^5$) compared with b) experiment ($Re_c = 2.5 \times 10^6$). Measured data is from Clark [1].	88
Figure 4.20 Comparison of the baseline and fence time- and span-averaged C_f distribution on the (a) pressure side and (b) suction side.	89
Figure 4.21 Farfield noise spectra at $\theta =$ a) 25° , b) 45° , c) 90° , and d) 135°	90
Figure 4.22 Farfield noise spectra at $\theta =$ a) 335° , b) 315° , c) 270° , and d) 225°	91
Figure 4.23 Farfield noise directivity at $f =$ a) 638 Hz, b) 850 Hz, c) 1487 Hz, and d) 2549 Hz. Baseline is in black, $d/\delta^* = 0.107$ fence is in red and $d/\delta^* = 0.214$ fence is in blue.	92
Figure 4.24 Comparison of the baseline and fence surface pressure spectra at $x/c = 0.971$ on the (a) pressure side and (b) suction side.	93
Figure 4.25 Comparison of the baseline and fence surface pressure spectra at $x/c = 0.971$ on the (a) pressure side and (b) suction side. Measurements are from Clark [1].	94
Figure 4.26 Comparison of the NACA 0012 baseline and fence surface pressure spectra at a) $x/c = 0.971$ and b) $x/c = 0.994$. Predictions are from Bodling <i>et al.</i> [10].	95
Figure 4.27 Comparison of the baseline and fence surface pressure spectra at $x/c = 0.994$ on the (a) pressure side and (b) suction side.	96

Figure 4.28 Measured profiles of (a) velocity, (b) velocity gradient and (c) farfield noise from the flat plate experiment by Millican [11]. The profiles are measured at the trailing edge of the flat plate. The horizontal dashed lines represent the maximum height of the fences.	97
Figure 4.29 Comparison of the NACA 0012 baseline and fence span-averaged (a) surface pressure spectra, (b) wall normal velocity profiles and (c) z-vorticity and (d) k/U_∞^2 at $x/c = 0.994$. Predictions with $P/\delta^* = 1.49$ are from Bodling <i>et al.</i> [10].	98
Figure 4.30 Comparison of the baseline and fence time- and span-averaged velocity distribution on the suction side of the (a) NACA 0012 and (b) DU96-W-180 close to the trailing edge at $x/c = 0.994$	99
Figure 4.31 Comparison of the baseline and fence time- and span-averaged z-vorticity distribution on the suction side of the (a) NACA 0012 and (b) DU96-W-180.	100
Figure 4.32 Comparison of the baseline and fence time- and span-averaged velocity distribution on the (a) pressure side and (b) suction side of the DU96-W-180 at $x/c = 0.994$	101
Figure 4.33 Comparison of the baseline and fence time- and span-averaged k/U_∞^2 distribution on the (a) NACA 0012, (b) DU96-W-180 pressure side and (c) DU96-W-180 suction side at $x/c = 0.994$	102
Figure 4.34 Comparison of the baseline and fence time- and span-averaged k/U_∞^2 distribution near the wall on the (a) NACA 0012, (b) DU96-W-180 pressure side and (c) DU96-W-180 suction side at $x/c = 0.994$	102
Figure 4.35 FDL3DI predicted vertical velocity fluctuation spectra for the (a) NACA 0012, (b) DU96-W-180 pressure side and (c) DU96-W-180 suction side at $x/c = 0.994$. Spectra is taken within the viscous sublayer ($y^+ = 0.5$). Predictions are averaged along the span with the points within the fences removed from the averaging procedure.	103
Figure 4.36 Comparison of the baseline and fence surface pressure spectra at the top of the middle fence (4th fence) at $x/c = 0.98$ on the (a) pressure side and (b) suction side.	103

Figure A.1	2nd Order Interior Filter	121
Figure A.2	4th Order Interior Filter	121
Figure A.3	6th Order Interior Filter	121
Figure A.4	8th Order Interior Filter	121
Figure A.5	10th Order Interior Filter	121
Figure A.6	4th Order Near-Boundary Filter at Node 2	127
Figure A.7	5th Order Near-Boundary Filter at Node 2	127
Figure A.8	6th Order Near-Boundary Filter at Node 2	127
Figure A.9	7th Order Near-Boundary Filter at Node 2	127
Figure A.10	8th Order Near-Boundary Filter at Node 2	127
Figure A.11	5th Order Near-Boundary Filter at Node 3	128
Figure A.12	6th Order Near-Boundary Filter at Node 3	128
Figure A.13	7th Order Near-Boundary Filter at Node 3	128
Figure A.14	8th Order Near-Boundary Filter at Node 3	128
Figure A.15	7th Order Near-Boundary Filter at Node 4	129
Figure A.16	8th Order Near-Boundary Filter at Node 4	129
Figure A.17	9th Order Near-Boundary Filter at Node 5	129
Figure A.18	10th Order Near-Boundary Filter at Node 5	129
Figure B.1	Structured grid used for validation of the FW-H solver; every 4th grid line is shown for clarity. The red inner circle is the FW-H integration surface; noise is predicted at the observer locations shown with the blue outer circle.	134
Figure B.2	The process by which the 3-D FW-H solver is used on the 2-D grid.	135
Figure B.3	Dilatation fields for the monopole, dipole and quadrupole sources that are used for verification of the FW-H solver.	136
Figure B.4	Directivity comparisons of PSD for a point source radiating in a moving medium between the FDL3DI predicted value (solid black lines) in the far field and the FW-H predicted value (open circles). All polar plots are shown at the frequency of the harmonic source.	137

Figure C.1	Filters used at boundary points (BP) 2-5	138
Figure C.2	$\hat{e}_\eta \times \hat{e}_\zeta$ slice taken at an arbitrary location along the fence height.	139
Figure C.3	The points where the fences are located are first treated as interior points and are assigned 8th order central filters.	139
Figure C.4	I-blanking and boundary condition procedure for modeling fences	140
Figure C.5	The plot shows how the solutions are filtered near the holes in the original FDL3DI code. The solution is given a boundary filter before and after the start of the holes in all directions.	140
Figure C.6	The figure shows the problem that arises with the original FDL3DI code at planes throughout the fence height. The filter is not applied correctly near the corners of the fence, which leads to instabilities.	141
Figure C.7	Filter implementation corrected for planes throughout the height of the fences.	141
Figure C.8	$\hat{e}_\eta \times \hat{e}_\zeta$ slice taken at the top of a fence step.	141
Figure C.9	The figure shows the problem that arises with the original FDL3DI code at planes at the top of a fence step. The filter is not applied correctly near all four walls, which leads to large instabilities.	142
Figure C.10	Filter implementation corrected for planes at the top of a fence step.	142

ABSTRACT

This work presents numerical analysis of airfoil geometries inspired by the down coat of the night owl. The objective is to understand the mechanisms of airfoil trailing edge noise reduction that has been observed with such designs in previous experiments. To reduce the computational complexity, first the NACA 0012 airfoil is selected as the baseline airfoil. The bioinspired geometry consists of an array of “finlets” that are applied near the trailing edge of the baseline airfoil and are aligned with the flow direction. Wall-resolved large eddy simulations are performed over the baseline and the bioinspired airfoil geometries and the aerodynamic and aeroacoustic performance of the two geometries are contrasted. Both models are simulated at chord-based Reynolds number, $Re_c = 5 \times 10^5$, flow Mach number, $M = 0.2$, and angle of attack, $\alpha = 0^\circ$. The boundary layer in the simulations is tripped with a geometry-resolved trip wire in order to compare with experiments that are at much higher Re_c (of the order of 2 M).

Comparisons with experimental data show good agreement for aerodynamic pressure coefficient (C_p) and skin friction coefficient distributions (C_f) for the baseline airfoil. The time-averaged wall-normal velocity and Reynolds stresses for the baseline airfoil also agree well with experimental and direct numerical simulations (DNS) data. Farfield noise spectra comparisons between the baseline and the bioinspired airfoil near the airfoil trailing edge show reductions of up to 10 dB with the finlets. The simulations reveal that the finlets lift turbulence eddies away from the airfoil trailing (scattering) edge hence reducing the scattering efficiency. These findings suggest that one of the mechanisms of noise reduction is the increased source-scattering edge separation distance. Reductions in the unsteady surface pressure and velocity fluctuations near the airfoil surface are observed primarily at high frequencies which suggests that the increased source-scattering edge separation distance mainly influences the high-frequency noise. The simulations also show that the finlets reduce spanwise coherence, particularly at low frequencies. This is attributed to be the mechanism of low-frequency noise reduction with the finlets.

Two additional finlet designs are tested on the NACA 0012 airfoil. In one design, the leading edge of the finlet is changed so that the final height is reached in a single “step”. In the other design, the finlet height is increased from $H = 1.00\delta^*$ to $H = 2.26\delta^*$, where δ^* is the displacement thickness. The lack of farfield noise reduction from the single-step finlet demonstrates the importance of having a finlet leading edge that is highly skewed to the incoming flow. Increasing the finlet height is shown to further reduce the high-frequency noise, but with a higher aerodynamic drag penalty.

The finlets are then applied to a DU96-W-180 baseline airfoil at a non-zero lift condition to permit direct comparisons with the experimental data and to evaluate the hypotheses of the noise reduction mechanisms at realistic operating conditions. Two fences with nondimensional thicknesses, $d/\delta^* = 0.107$ and 0.214 are investigated. Wall-resolved large eddy simulations are performed at chord-based Reynolds number, $Re_c = 6 \times 10^5$, flow Mach number, $M = 0.146$, and angle of attack, $\alpha = -0.2^\circ$. The simulation results suggest that the fences should be as thin as possible to minimize the adverse impact on drag and lift. On the suction side near the maximum fence height, there are reductions in the high-frequency surface pressure spectra. However, close to the trailing edge the simulations show no reductions in the high-frequency surface pressure spectra and therefore, no high-frequency farfield noise reduction is predicted. This shows that the reductions in the surface pressure fluctuations *closest* to the trailing edge are ultimately what leads to farfield noise reductions. Larger velocity deficit below the fence height is shown to lead to more reductions in the surface pressure fluctuations. The velocity deficit and source-trailing edge separation distance is shown to work in tandem to reduce the pressure fluctuations near the trailing edge. Although both the pressure and suction side has an increase in velocity near the airfoil surface, since the source-trailing edge separation distance on the pressure side is larger (or large enough), there are still reductions in the surface pressure fluctuations on the pressure side. Higher farfield noise of thicker fence is attributed to scattering of sound from the top surfaces of the fences. Thinner fences are therefore both aerodynamically and aeroacoustically better than thicker fences.

CHAPTER 1. INTRODUCTION

The continued increase in air travel and the recent exponential growth in wind energy is bound to exacerbate the noise pollution problem. The detrimental effects on the hearing health of humans due to aircraft noise [12, 13] is well known. The effects from wind turbine noise [14, 15] have also been investigated. The consequent economic implications are severe; e.g., the U.S. Department of Veterans Affairs spends over \$1 billion per year for hearing loss! With noise affecting many peoples lives, reducing noise is no longer a luxury, but a critical technology that must be incorporated into the designs of wind turbines and aircraft in the future.

Airfoil self noise in wind turbines and aircraft is due to the interaction of flow unsteadiness with the airfoil surface. Airfoil “self noise” can be generated via multiple mechanisms. As described in detail in Ref. [16], these are separation stall noise, laminar boundary layer-vortex shedding noise, tip vortex formation noise and trailing edge noise. In this dissertation, we will focus on the reduction of airfoil trailing edge noise. Trailing edge broadband aerodynamic noise in an airfoil results from the interaction of the surface boundary layer turbulence with the trailing edge. The fluctuating eddies in turbulence are a source of noise by themselves, but it is their close proximity to an edge such as the airfoil trailing edge that amplifies the sound produced [17]. When the flow Mach number is small (≤ 0.2), unsteady surface pressure resulting from the interaction of turbulence with the trailing edge is the primary aerodynamic noise source.

Reducing trailing edge noise is an important problem for many different applications. Trailing edge noise is an important aspect of noise generation from civil aircraft while landing and approaching the ground. Controlling trailing edge noise is critical to achieving the long term goal of the aviation industry, which is to reduce aircraft noise by 20 dB [18]. It is important to control trailing edge noise from propellers and hydrofoils so that the stealthiness of surface and underwater craft

is increased [19]. The major noise generation mechanism for helicopters [20], and wind turbine blades [21] is trailing edge noise, which limits their use in urban areas.

A relevant research question is how do we reduce trailing edge noise? One interesting approach, known as biomimicry, is to create trailing edge noise reduction designs that emulate nature's time-tested patterns and strategies. A variety of engineering applications have used biomimicry to create many great innovations, [22] e.g., temperature-regulated buildings inspired by termite mounds, [23] self-cleaning paints using the lotus leaf effect, [24] etc. However, the flight of nocturnal owls is yet to find its due engineering application. The only bird known to man that is capable of almost silent flight is the owl. [25, 26] It can not be heard until it is within 3 meters of its prey. [2] Owls use the acoustic stealth to aurally locate their prey in the dark and also avoid aural detection by the prey. [27] One species of nocturnal owls - the barn owl (*Tyto alba*) - is particularly skilled at silent flight. Hereinafter, we shall refer to the barn owl as "the owl".

During gliding flight the owl's chord-based Reynolds number is between 50,000 – 90,000. A similar Reynolds number range is operated in by small-scale micro- and unmanned aerial vehicles (MAVs/UAVs). Figure 1.1 illustrates the range of Reynolds number over which various flying machines and animals, including the owl, operate. Bio-inspired designs based off of the owl anatomy would therefore apply to UAVs and MAVs where the flow is expected to be mainly laminar across the blades/wings. The objective of this dissertation, however, is to start exploring if similar bio-inspired designs at much higher Reynolds numbers (10^5 – 10^7), where the flow is expected to be turbulent, will also lead to noise reductions. Therefore, knowledge gained from this dissertation will assist in the development of trailing edge noise-quelling designs for applications with high Reynolds number regimes such as aircraft engines and wind turbines.

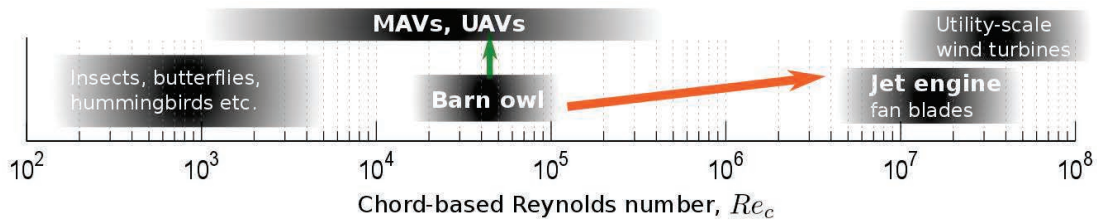


Figure 1.1: Chord based Reynolds number (Re_c) of various species compared with different aircraft

Previous investigations [25, 26, 2] have shown three key anatomical features unique to the nocturnal owl that play a role in reducing noise during flight:

1. Stiff comb-like structure at the leading edge (LE) of the wing,
2. Flexible fringe like structure at the trailing edge (TE) of the wing, and
3. Soft, thick downy coat on the flight feathers.

The stiff comb-like structures (referred as serrations) at the leading edge consists of the barbs that are extended from the 10th primaries of the owl. The fringes at the trailing edge, which are present on each primary feather, is formed by the barbs that extend from the posterior part of the vane. The downy coat, the layer of fine feathers found under the tougher exterior feathers, acts as a poroelastic surface. These features are visualized in Fig. 1.2 using images of barn owl wing specimens. Each of these features contributes towards making the owl flight silent. The owl *hush kit* refers to these three features of the owl [28].

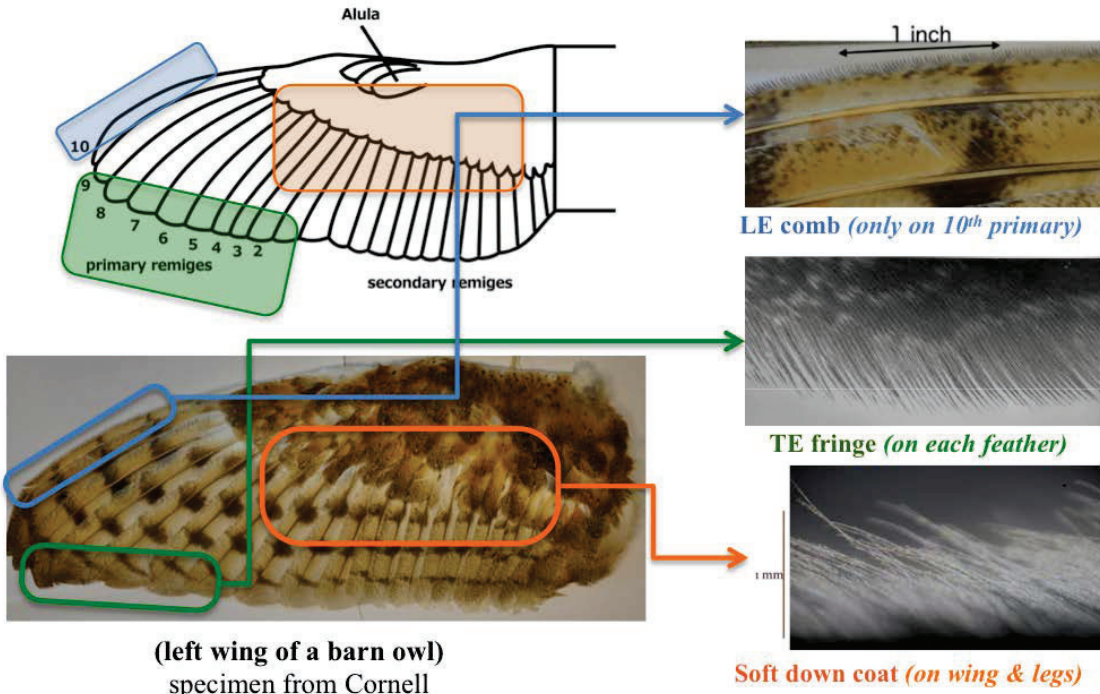


Figure 1.2: The owl hush kit: unique feather adaptations that enable the owl to fly silently. Top: barn owl wing specimen. Bottom: Photographs through a microscope of (a) leading edge comb, (b) downy coat on flight feathers, and (c) trailing edge fringe. Images (b) and (c) are from Refs. [2, 3].

Owl-inspired LE and TE designs (serrations) have been developed and investigated extensively in laboratory [29, 30, 31, 28] and in the field [32]. This paper focuses on the third owl feather feature in the list above – the down coat, which has not received as much research attention until recently. Geyer *et al.* [33] related the down coat to the porosity of a wing. By doing a series of experiments that used airfoils made out of different porosity materials, they found that at the frequencies less than about 10 kHz, porous airfoils were able to attenuate the trailing edge broadband noise by over 10 dB. However, the aerodynamic performance decreased as the resistivity of the airfoils increased with porosity. Jaworski and Peake [34, 35] analyzed the trailing-edge condition and found that the fifth-power (M^5) dependency of the radiated acoustic power of a trailing edge was weakened by both porosity and flexibility. However, they did not investigate the effect of the feather structure formed by the hairs on the flight feathers of the owl.

Microscopic observations by Clark *et al.* [3] revealed that hairs on owl feathers rise vertically up from the feather substrate (lifting surface of the wing) and then plateau out in the streamwise direction, forming a structure similar to a forest/plant canopy. [3] Fluid flow in plant canopies has been investigated elsewhere [36]. Clark *et al.* [3] found that the owl canopy has an open area ratio of about 70% and is suspended approximately 0.5 mm above the feather substrate. Based on these observations, they designed artificial canopies with different open area ratios and performed wall-jet wind tunnel experiments to examine the effect of the canopies on surface roughness noise. The canopies were designed using a large number of parallel fibers made from the material used for fishing lines. These fibers were oriented in the direction of the flow and located just above the flow surface. The canopies were found to reduce both the surface pressure fluctuations (by as much as 30 dB!) and the radiated farfield noise.

This exciting discovery motivated them to develop trailing edge noise reduction designs. These designs also used the concept of canopy, but were designed to be robust enough for industrial application, e.g., on wind turbine blades. The designs presented in Clark *et al.* [4] achieved the canopy effect by attaching small structures (height less than the boundary layer) near the trailing edge, which they called “finlets”. Figure 3.1 shows schematics of two finlet designs, finlet fence and finlet rail, used in these experiments. Twenty different configurations of these two designs were tested in the experiments by changing the height, spacing, thickness, and extension of the fences and rails. Com-

pared to the unmodified (baseline) airfoil, these configurations were found to reduce the trailing edge noise by up to 10 dB [4].

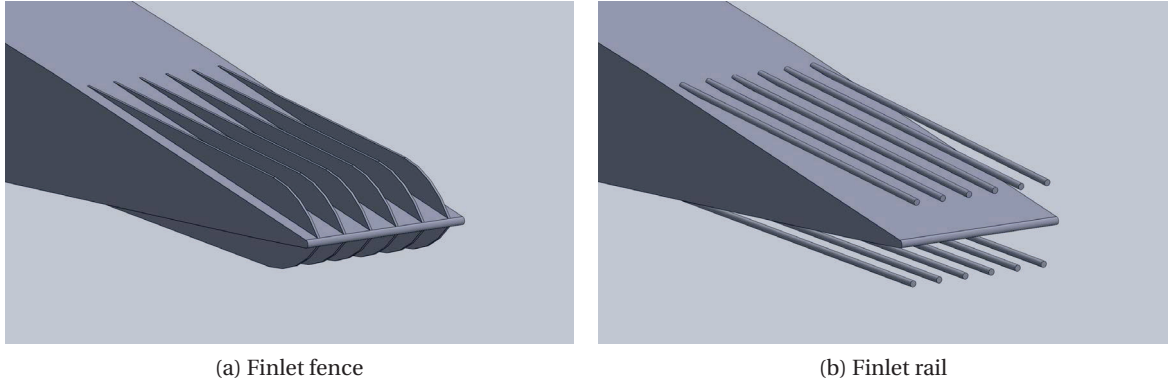


Figure 1.3: Idealized representations of the a) finlet fence and b) finlet rail designs which were experimentally investigated in Ref. [4]. The struts to support the finlet rails are omitted for clarity.

Based on the results of the different configurations tested, the finlets are believed to: (a) lift the energetic eddies in the turbulent boundary layer away from the airfoil trailing edge, thereby reducing the scattering efficiency, and (b) reduce spanwise coherence in the boundary layer. These are the working hypotheses behind the observed noise reduction. The objective of this dissertation is to use high-fidelity aeroacoustics simulations to determine the mechanisms behind the observed noise reduction to verify or disprove the working hypotheses. This dissertation also seeks to better understand how the finlets affect the aerodynamic performance of the airfoil.

Trailing Edge Noise Theory

This section will explain the theoretical framework for the noise reduction hypotheses. The basic equation that describes aerodynamic noise generation and propagation is due to Lighthill [37]. Lighthill's equation can be written as the following inhomogeneous Helmholtz equation,

$$\nabla^2 p^* + k^2 p^* = - \left[\frac{\partial^2 \rho v_i v_j}{\partial y_i \partial y_j} \right]^* \quad (1.1)$$

where k is the acoustic wave number $k = \omega/c$, p is the pressure in the fluid, ρ is the fluid density, c is the speed of sound, and v is the fluid velocity. The superscript denotes the general Fourier trans-

form of a quantity. Ffowcs-Williams and Hall [38] solved this equation for a rigid, vanishingly thin, half-plane immersed in an otherwise unbounded flow. The rigid half-plane gives the boundary condition that the normal velocity vanishes at the surface. Using this boundary condition, the solution to Eqn. 1.1 can be written in terms of the Green's function, G , whose normal derivative is zero on the half-plane. The solution is:

$$p^*(\mathbf{x}, \omega) = \frac{1}{4\pi} \iint \left[\frac{\partial^2 \rho v_i v_j}{\partial y_i \partial y_j} \right]^* G dV(\mathbf{y}) + \frac{1}{4\pi} \iint \frac{\partial p^*}{\partial n} G dS, \quad (1.2)$$

where,

$$(\nabla^2 + k^2)G = -4\pi\delta(\mathbf{x} - \mathbf{y}), \quad (1.3)$$

with

$$\frac{\partial G}{\partial n} = 0 \quad (1.4)$$

on the half-plane. Ffowcs-Williams and Hall [38] solved the above integral for the case where a cylindrical eddy (region of the turbulence over which fluctuations of velocity are highly correlated) is centered on the edge and is well within an acoustic wavelength of the edge, $2kr_o \ll 1$, where r_o is the distance between the center of the eddy to the edge. Using some simplifications and farfield approximations, Ffowcs-Williams and Hall [38] derived the following analytical expression for the farfield sound intensity emanating from the edge of the half-plane:

$$I = \frac{k\rho U^4 \alpha^2 V^2 \eta}{\pi^3 c R^2 r_o^3} \quad (1.5)$$

where δ is the radius of the cylindrical eddy (which can be thought of as the turbulence length-scale), U is a typical fluid velocity, α is the normalized turbulence intensity, η is directionality terms, R is the distance between the observer and source, and V is the volume of the eddy. Noting that the typical frequency of the turbulent source is on the order $\frac{U}{\delta}$ so that $k \approx \frac{U\pi}{c\delta}$, and the volume of the eddy V is on the order of $V \approx \delta^3$, the sound intensity can be written as,

$$I \sim \frac{U^5 \alpha^2 \delta^2}{(r_o/\delta)^3}. \quad (1.6)$$

This is the well known result in acoustics that shows the sound intensity from an edge scales with the fifth power of the fluid velocity. Therefore, for low flow speeds trailing edge noise is the dominant noise source. Trailing edge noise is stronger than the noise emanating from turbulence in the free stream ($I \sim U^8$) or near an acoustically compact surface ($I \sim U^6$) [39]. This result also gives insight into possible noise reduction designs. We see from Eqn. 1.6 that theoretically if the flow velocity, turbulence intensity or turbulence lengthscale decreases, the farfield sound will also decrease. We can also see from Eqn. 1.6 that if the distance between the turbulence (source) and the scattering (airfoil trailing) edge increases, then the farfield sound will decrease.

Following this work, Amiet [40] developed a relation for the farfield noise from the edge of a half-plane in a free-stream flow. The farfield noise is given as:

$$S_{pp}(x, 0, z, \omega) = \left(\frac{\omega b z}{2\pi c_\infty \sigma^2} \right) l_y(\omega) d |L|^2 S_{qq}(\omega, 0). \quad (1.7)$$

In this relation, b is the airfoil semichord, ω is angular frequency, x is position in the streamwise direction, z is position in the vertical direction, c_∞ is the speed of sound, $\sigma^2 = x^2 + \beta^2 z^2$, $\beta = 1 - M^2$, d is the airfoil semispan, L is the airfoil lift response function, $S_{qq}(\omega, 0)$ is the surface pressure power spectral density at a point, and $l_y(\omega)$ is the spanwise correlation length scale of the turbulent pressure fluctuations, given as:

$$l_y(\omega) = \frac{1}{S_{qq}(\omega, 0)} \int_0^\infty S_{qq}(\omega, y) dy \quad (1.8)$$

The relation derived by Amiet [40] shows us that reductions in the unsteady surface pressure fluctuations and coherence length at the airfoil trailing edge will lead to a reduction in the farfield noise.

Outline of Dissertation

The remainder portion of the dissertation is organized as follows. The second chapter investigates the aeroacoustic impact of the shape of the leading edge of the finlets. This is studied by modeling the finlet fences with a “single-step” and “stair-step” configuration. The finlet fences are applied to the trailing edge of a NACA 0012 airfoil at the no-lift condition.

The third chapter studies the effect of varying the height of the finlet fences to bolster our understanding of the noise reduction mechanisms. It also analyzes the drag impact when using different fence heights. The baseline airfoil and flow conditions are the same as used in the second chapter.

The fourth chapter seeks to understand how the thickness of the finlet fences effect the aerodynamic and aeroacoustic performance of the airfoil. Unlike the second and third chapters, this chapter applies the finlets to the same airfoil used in the experiment and at a non-zero lift condition. This is done to permit direct comparisons with the experimental data and to evaluate the hypotheses of the noise reduction mechanisms at realistic operating conditions. This chapter also investigates the effect of finlet spacing by repeating the analysis from chapter three with a larger fence spacing.

The fifth and final chapter presents some conclusions drawn from the study and lays a path forward for future research.

CHAPTER 2. NUMERICAL INVESTIGATION OF NOISE REDUCTION MECHANISMS IN A BIO-INSPIRED AIRFOIL

This chapter was published in the Journal of Sound and Vibration in 2019. [41]

Abstract

This paper presents a numerical analysis of an airfoil geometry inspired by the down coat of the night owl. The objective is to understand the mechanisms of airfoil trailing edge noise reduction that has been observed with such designs in previous experiments. The bioinspired geometry consists of an array of finlet “fences” that are applied near the trailing edge of the baseline (NACA 0012) airfoil. Wall-resolved large eddy simulations are performed over the baseline and the bioinspired airfoil geometries and the aeroacoustic performance of the two geometries are contrasted. Both models are simulated at chord-based Reynolds number $Re_c = 5 \times 10^5$, flow Mach number, $M_\infty = 0.2$, and angle of attack, $\alpha = 0^\circ$. Unsteady surface pressure spectra near the airfoil trailing edge show large reductions at high frequencies but an increase in low frequencies with the bioinspired airfoil, consistent with previous measurements. Farfield noise spectra comparisons between the baseline and the bioinspired airfoil show reductions of up to 10 dB with the fences. The simulations reveal that the fences lift the turbulence eddies away from the airfoil trailing (scattering) edge hence reducing the scattering efficiency. These findings suggest that one of the mechanisms of noise reduction is the increased source-scattering edge separation distance. Two-point correlations show that the fences reduce the spanwise coherence at low frequencies for separation distances greater than a fence pitch. Reduction in spanwise coherence is another potential mechanism of farfield noise reduction at low frequencies.

2.1 Introduction

One biological feature that has yet to be used in engineering innovations is the silent flight of nocturnal owls. One species of nocturnal owls - the barn owl (*Tyto alba*) - is particularly adept at silent flight. In this paper, we refer to the barn owl as ‘the owl’. The owl has unique feather features – the leading edge (LE) comb, the down coat on flight feathers, and the trailing edge (TE) fringes – which are collectively referred to as the “hush kit”. There has been considerable research on using LE and TE features, modeled as serrations, to reduce airfoil noise [29, 30, 31]. The down coat has been investigated analytically [34, 42] and experimentally [3, 4]. However, little to no numerical research has been performed to investigate the acoustic impact of the owl down coat. This paper uses high-resolution large eddy simulations to perform diagnosis of sound sources in blade designs inspired by the down coat of owl feathers.

The particular bioinspired blade designs that form the focus of this paper were first discussed by Clark *et al.* [3]. They suggested that the down coat (made of hairs that rise up vertically and plateau in the flow direction) forms a canopy and makes the flow behave similarly to forest canopy flows. They attempted to reproduce this canopy effect using “finlets” which were constructed in two different ways - (a) using an array of sharp edge fences, and (b) using tiny cylindrical rails. Clark *et al.* [3, 4] presented aeroacoustics measurements of trailing edge noise from airfoils with these finlets (fences and rails) installed using a substrate near the trailing edge of the baseline airfoil. The DU96-W-180 airfoil, commonly used in wind turbine applications, was selected as the baseline in these experiments.

Figure 3.1 shows the schematics of the two finlet designs used in the experiments [3, 4]. Plots (a) and (b) in the figure are the fence and rail configurations, respectively. Farfield sound measurements made using acoustic beamforming [43] showed that the finlet designs were significantly quieter than the baseline airfoil [4].

This paper presents results of highly-resolved large eddy simulations of a baseline airfoil as well as the baseline airfoil fitted with two different designs of finlet fences. It should be noted that the baseline airfoil used in this study is NACA 0012 while the experiments of Ref. [4] used the DU96-W-180 airfoil. Also, the simulations are performed at a chord-based Reynolds number $Re_c^{(\text{sim})} = 5 \times 10^5$,

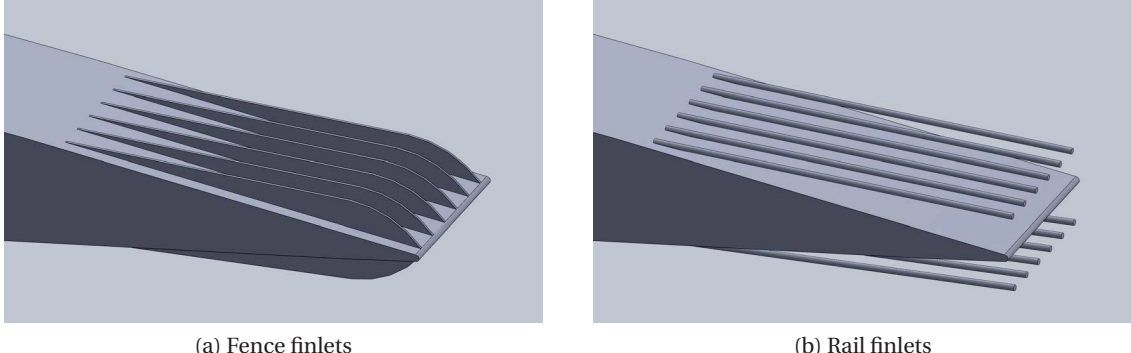


Figure 2.1: Idealized schematics of the two finlet designs used by Clark *et al.* [4].

which is smaller than that of the experiments $Re_c^{(\text{exp})} = 2.1 \times 10^6$. These simplifications are made to manage the complexity and the computational requirements to solve the problem. Nevertheless, the simulations reveal several interesting flow physics that shed new light on the potential mechanisms of the observed noise reduction, thus supplementing the experimental results of Ref. [4]. This research builds upon authors' previous studies in simulating finlet fences [44, 45]. Bodling *et al.* [44, 45] modeled the finlet fences as a single-step geometry by varying the height of the fences in a single discrete step (as opposed to a continuous variation in the experiment model). Although the single-step design was successful in reducing the unsteady surface pressure fluctuations on the airfoil surface near the airfoil trailing edge, it did not result in the farfield noise reduction observed in the experiments of Ref. [4]. In this article, we focus on the aeroacoustic impact of the geometry of the leading edge of the finlet fences. Results from three sets of simulations are presented and compared: (a) baseline airfoil (NACA 0012), and the baseline airfoil with finlet fences installed where the leading edge of the fence is modeled as a (b) single-step, and (c) as a stair-step. Figure 3.2 contrasts the geometries of the fences used in the experiments with those used in the simulations.

In the experiments, the leading edge of the fence is nearly parallel to the flow while in the “single-step” geometry, the leading edge is orthogonal to the flow. Potential problems with the orthogonal leading edge in the single-step simulation include a) scattering of the boundary layer turbulence into radiated sound, and b) production of turbulence at the sharp edge. To alleviate this problem and to better match the experimental geometry, the fence is modeled using a “stair-step” geometry in this paper. While the simulated stair-step geometry is still an approximation to the smooth edge

in the experiments, the smaller vertical jumps are de-correlated by spatial separation and hence not as efficient in acoustic scattering.

The objective is to make *qualitative* comparisons between the measurements and the predictions with the stair-step leading edge fence geometry to gain confidence in the simulations, and then perform source diagnostics using the highly-resolved flowfield to enhance understanding of the noise reduction mechanisms of finlets.

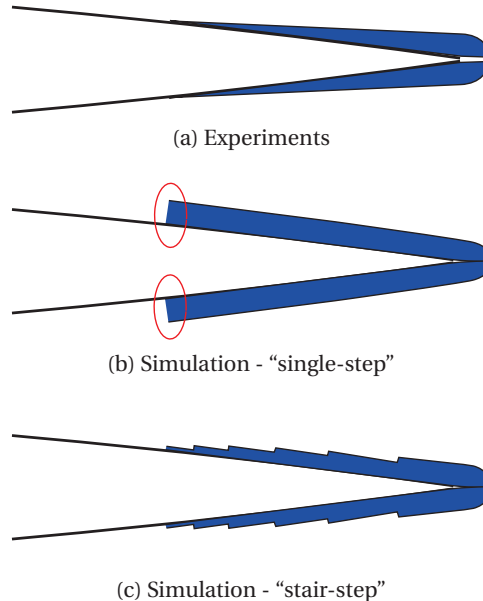


Figure 2.2: Schematics highlighting the differences in the fence geometries between the experiments and the current simulations.

2.2 Numerical Methodology

A two-step approach is used for farfield noise prediction. Fluid flow simulations are first carried out using a computational fluid dynamics (CFD) solver and subsequently, an integral method (acoustic analogy) is used with the CFD data to compute the radiated noise in the far-field. The compressible Navier-Stokes solver, FDL3DI [46] is used for the fluid flow simulations. The numerical approach used here has been previously validated by the authors and utilized to assess noise reduction ability of leading edge serrations [28, 31]. Brief descriptions of the flow solver and the noise radiation solver are provided below for completeness.

The compressible Navier-Stokes solver, FDL3DI [46], is used for the fluid flow simulations. The governing fluid flow equations (solved by FDL3DI), after performing a time-invariant curvilinear coordinate transform $(x, y, z) \rightarrow (\xi, \eta, \zeta)$, are written in a strong conservation form as

$$\frac{\partial}{\partial t} \left(\frac{\mathbf{U}}{J} \right) + \frac{\partial \hat{\mathbf{F}}_I}{\partial \xi} + \frac{\partial \hat{\mathbf{G}}_I}{\partial \eta} + \frac{\partial \hat{\mathbf{H}}_I}{\partial \zeta} = \frac{1}{Re} \left[\frac{\partial \hat{\mathbf{F}}_v}{\partial \xi} + \frac{\partial \hat{\mathbf{G}}_v}{\partial \eta} + \frac{\partial \hat{\mathbf{H}}_v}{\partial \zeta} \right], \quad (2.1)$$

where J is the Jacobian of the coordinate transformation, $\mathbf{U} = \{\rho, \rho u, \rho v, \rho w, \rho E\}$; the expressions for inviscid flux terms, $\hat{\mathbf{F}}_I, \hat{\mathbf{G}}_I, \hat{\mathbf{H}}_I$ and viscous flux terms, $\hat{\mathbf{F}}_v, \hat{\mathbf{G}}_v, \hat{\mathbf{H}}_v$ are provided in Ref. [46]. We perform ‘implicit’ LES (ILES) simulations using FDL3DI by employing sixth-order spatial accuracy, eighth-order low pass filters, and a second order, implicit time integration scheme.

Far-field sound propagation is performed using the Ffowcs Williams-Hawkins (FW-H) acoustic analogy [47]. For low-Mach number flows ($M \leq 0.2$) the volume sources are much weaker than the surface sources and can be neglected. Using this assumption, the following integral equation is obtained for far-field acoustic pressure, p' at location \mathbf{x} and time t :

$$p'(\mathbf{x}, t) = \frac{1}{4\pi|1 - M_r||\mathbf{x}|} \left(\frac{\partial}{\partial t} \iint [\rho_0 u_i n_i + \rho'(u_i - U_i) n_i] d\Sigma + \frac{x_i}{c|\mathbf{x}|} \frac{\partial}{\partial t} \iint [p' n_i + \rho u_i (u_j - U_j) n_j] d\Sigma \right), \quad (2.2)$$

Solving Eq. 3.3 requires integrating over a surface Σ that encloses all sound sources. In the above, n_i is normal to the surface Σ , p' and ρ' are pressure and density fluctuations, ρ_0 is mean density, u_i is perturbation flow velocity and U_i is the velocity of the surface Σ . The source is at the origin, and \mathbf{x} denotes the observer location. We choose a “porous” surface around the airfoil defined by one of the gridlines ($\xi = \text{constant} > 1$; $\xi = 1$ is the airfoil surface) of the O-mesh around the airfoil. The FW-H solver has been validated previously against canonical problems (point monopole, dipole, and quadrupole) as well as against experimental data for aerodynamic noise from propellers [48].

2.3 Geometry Modeling, Meshing, and Boundary Conditions

The NACA 0012 airfoil is selected as the baseline airfoil. For the bioinspired airfoil, finlet fences are added near the airfoil trailing edge. The span length of the airfoil model in the simulations is 5.85% of the airfoil chord. A single-block, O-grid is used to generate a 2-D mesh around the baseline

airfoil, which is repeated in the span direction to obtain the 3-D grid. The O-grid in the physical space (x, y, z) maps to an H-grid in the computational domain (ξ, η, ζ). The following orientation is used: \hat{e}_ξ points radially out, \hat{e}_η is in the circumferential direction, and \hat{e}_ζ is along the span direction such that the right-hand rule, $\hat{e}_\zeta = \hat{e}_\xi \times \hat{e}_\eta$, is obeyed. In the baseline grid used in this study, the distributions in the radial and circumferential directions of the O-mesh around the airfoil are similar to that described in Ref. [49], which was an LES of flow over an airfoil at $Re_c = 5 \times 10^5$. Based on the mesh sensitivity study performed in Ref. [49] and the recommendations from Georgiadis *et al.* [50], the grid spacing on the suction side was found to be appropriate for LES. In Ref. [49], only the suction side of the airfoil was resolved. To create the grid used in this study, the suction-side grid from Ref. [49] is mirrored on to the pressure side to resolve the flow over both surfaces of the airfoil.

Periodicity is imposed in the span direction (\hat{e}_ζ). The periodic boundary conditions are implemented using the Overset grid approach in FDL3DI. A minimum of five-point overlap is required by FDL3DI to ensure high-order accurate interpolation between individual meshes. The airfoil surface is modeled as a no-slip, adiabatic wall. Freestream conditions are prescribed at the outer boundary and the grid is coarsened away from the airfoil surface in order for the filtering procedure to remove all perturbations from the flow before they reach the outer boundary. The computational time step, $\Delta\tau$ is chosen to be very small ($= 4 \times 10^{-5}$). Based on the study by Choi and Moin [51], in the turbulent flow region the computational time step in terms of wall units, $\Delta t^+ = \Delta t u_\tau^2 / \nu \leq 0.048$, should be sufficiently accurate to resolve the near-wall turbulence. In the above, $\tau = t U_\infty / c$ is non-dimensional time ($\tau = 1$ is the time it takes for the flow to go past the airfoil), where c is the airfoil chord, t is the dimensional time, and U_∞ is the freestream flow speed.

2.3.1 Baseline Airfoil Mesh

The baseline is the NACA 0012 airfoil with a rounded trailing edge. The simulations are carried out at the chord-based Reynolds number, $Re_c = 5 \times 10^5$, the angle of attack, $\alpha = 0^\circ$, and the flow Mach number, $M_\infty = 0.2$. The choice of the first cell height with these flow conditions gives an average y^+ of 0.567 for the baseline geometry. The turbulent boundary layer is highly resolved. As an example, the boundary layer at $x/c = 0.85$ contains 110 grid points with approximately 15 points in the viscous sublayer. The max grid stretching ratio at the top of the boundary layer is 1.04. Figure 2.3

shows close-up, cross-sectional views of the O-grid around the baseline airfoil. For clarity, every third point in the radial and circumferential direction is shown in Fig. 2.3. Table 2.1 provides the grid metrics averaged over the turbulent flow region of the baseline simulation. The metrics are also averaged along the span.

Table 2.1: Baseline grid metrics

$N_\xi \times N_\eta \times N_\zeta$	y^+ avg, max	x^+ avg, max	z^+ avg, max
$410 \times 1937 \times 101$	0.567, 0.665	28.7, 37.1	14.9, 17.3

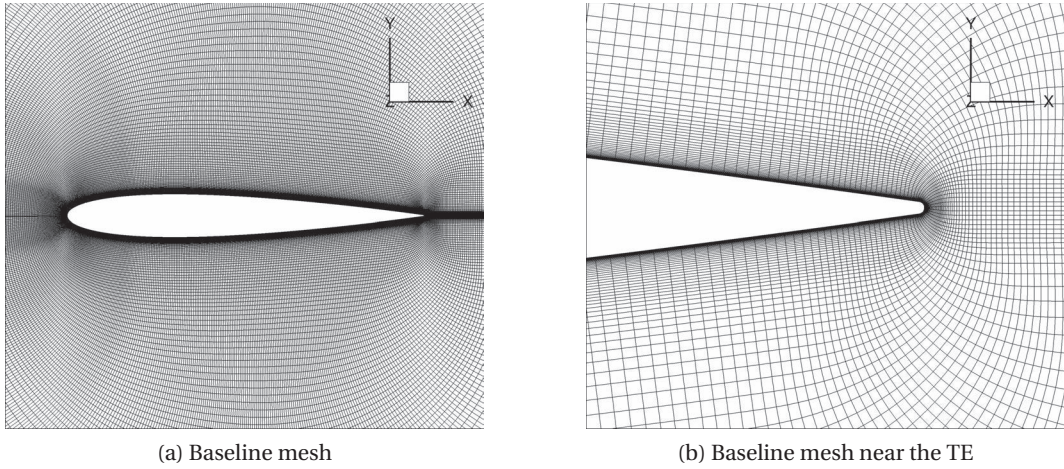


Figure 2.3: The O-grid topology used in the simulations; shown here for the baseline airfoil. The trailing edge is rounded and the mesh near the TE ($0.90 \leq x/c \leq 1.04$) is shown in (b). Every third point along each axis is shown for clarity.

2.3.2 Finlet Fence Geometry and Mesh

The meshes for the one-step and stair-step fence simulations are obtained from the baseline mesh by performing *hole-cutting* (also called point-blanking). Hole-cutting involves removing mesh points that lie inside a solid. In the simulations presented in this work, the regions occupied by the fences (defined by specifying ranges $\xi_1 - \xi_2$, $\eta_1 - \eta_2$, and $\zeta_1 - \zeta_2$) are cut out as holes from the baseline grid and the no-slip condition is applied to the new boundaries thus created. The PEGASUS software [52] is used to perform hole-cutting.

Figure 2.4 shows cross-sectional views of the single-step and stair-step finlet fence meshes; the views are zoomed in on the fence region to clearly show the geometric differences. The mesh points

in the grey regions between the blue lines and the airfoil surface are marked as holes and removed from the calculation. Figure 2.5 shows top views of the baseline mesh and the single-step fence mesh. The blue lines are the no-slip boundaries. The stair-step mesh is modeled in the same way except for the height of the fence which is varied in discrete steps with distance along the chord. The fence meshes were not further refined in the direction normal to the fence walls as the maximum z^+ with the baseline mesh is approximately 30.6 (located at the fence leading edge at the maximum height), which is not significantly greater than the span-averaged baseline z^+ value near the airfoil surface. Furthermore, we are not interested in precisely resolving the boundary layer on the surfaces of the fences. The working hypothesis is that the noise is reduced due to the displacement of energy-containing turbulence eddies away from the trailing edge, which can be captured even if the fence surfaces are modeled as inviscid walls. By not resolving the boundary layer on the sides of the fence walls, the near-fence-wall boundary layer flow physics may not be accurately captured. However, we believe that this level of resolution is not necessary to capture the observed noise reduction.

A 3-D mesh containing a single fence element is created and then repeated six times along the span to obtain the full 3-D mesh with a span of 5.85% chord. The dimensions (height and spacing) of the two finlet fence geometries simulated are similar to configuration *F3* in the experiments of Ref. [4], with the exception of the LE shape. The leading edge of the fence is at $x/c = 0.872$. The stair-step fence reaches the max height (H) at $x/c = 0.97$, where the height of the fence is about 19% of the boundary layer thickness ($y^+ \sim 110$). The x/c positions of the fence leading edge and maximum height are the same as in the experiment. The pitch of the fences is $1.5 \times H$ and the thickness is $0.17 \times H$. It should be emphasized that other than the holes (point blanking) introduced in the fence meshes, the grids for all three cases (baseline and two fences) are identical. This eliminates grid-to-grid differences in the simulation results when comparing the different designs.

2.3.3 Boundary Layer Trip

Since the simulation Re_c ($= 5 \times 10^5$) is smaller than that of the experiments ($\approx 2 \times 10^6$), the boundary layer on the airfoil surface is numerically tripped in the simulations. It should be noted that the boundary layer was also tripped in the experiments using a serrated tape. In the simulations, boundary layer tripping is achieved by placing a geometry-resolved “trip wire” at $x/c = 0.05$, measured from

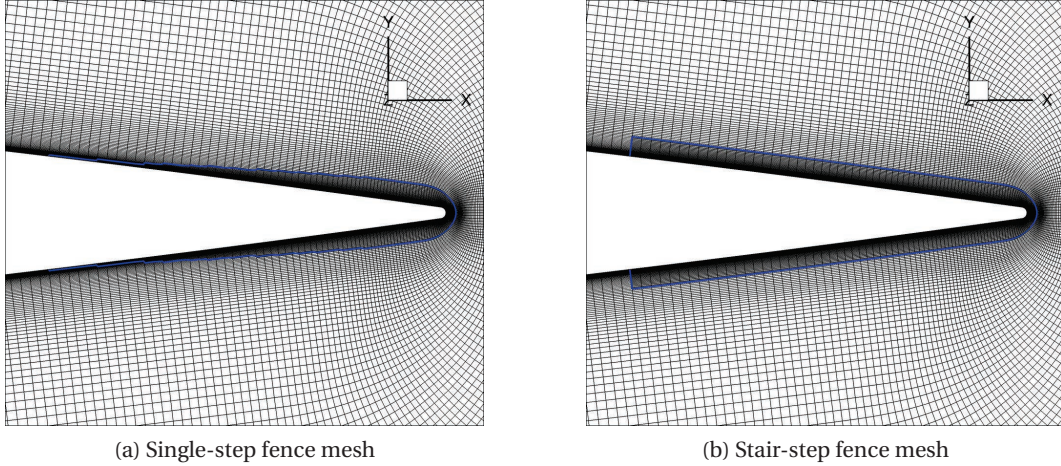


Figure 2.4: Cross-sectional (zoom) views ($0.861 \leq x/c \leq 1.005$) of the computational meshes used to simulate the single-step and stair-step fence geometries. Every other grid point along each axis is shown for clarity.

the leading edge of the airfoil. The trip wire is a square cylinder that extends throughout the span and is defined by blanking out cells in the regions occupied by the wire (see Fig. 2.6). The dimensions of the wire are defined by specifying ranges of the grid indices in the ξ , η and ζ directions; no-slip wall boundary condition is applied to the boundaries of the trip wire.

Figure 2.7 shows the iso-surfaces of the Q -criterion ($Q = 10$) on the suction surface of the baseline airfoil for the tripped simulation. The trip wire successfully forces the boundary layer to transition well upstream, compared to where it transitions naturally, thereby achieving a turbulent boundary layer similar to what would occur via natural transition at high Re_c .

2.3.4 Removal of Transients

Several techniques are employed to reduce the computational cost of the simulations. Each simulation is initiated in 2-D, with a potential flow solution as the initial condition. The Navier-Stokes equations are then solved for the 2-D problem until statistical convergence is achieved; this typically takes about 10τ , where $\tau (= c/U_\infty)$ is the characteristic flow time. The solution is then replicated in the span direction to obtain an initial 3-D solution for the baseline geometry. Transients in the 3-D simulation are then removed, which takes between 3τ to 5τ . For the 3-D simulations with fences, the solution is obtained in two steps. First the 2-D solution is replicated over a single-fence span

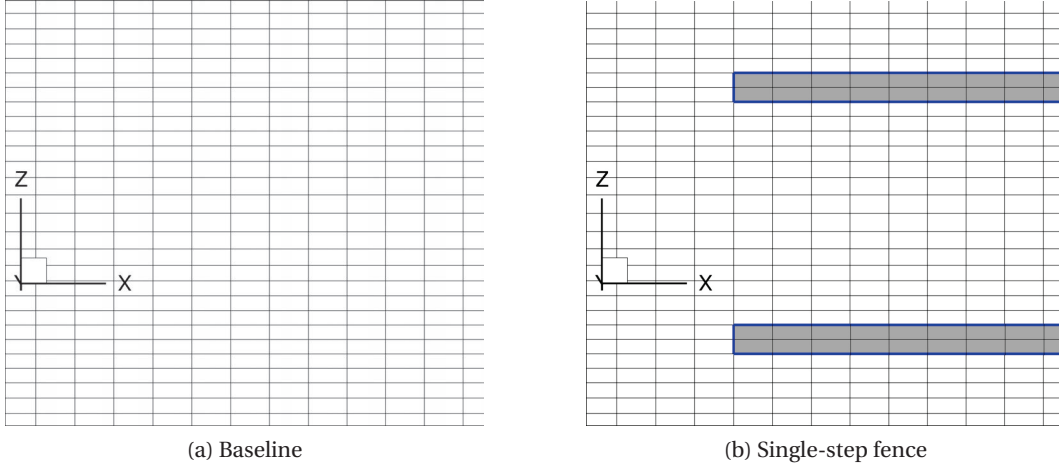


Figure 2.5: Top views ($0.865 \leq x/c \leq 0.885$) of the baseline and single-step fence meshes. Each fence element is modeled to be two cells thick in the simulations.

width and simulated with the fences modeled in the computation, and the solution is allowed to reach a statistically stationary state ($\approx 10\tau$). This solution is then repeated for as many fences as required (= 6 here) to fit in the 5.85% span length of the full 3-D geometry simulated. Transients are then removed in the full 3-D simulation (with the array of fences) by simulating the flow for another 5τ , before collecting data for noise analysis. Several methods are used to ensure the removal of transients. Each simulation is run until the integrated drag and lift forces become statistically stationary as well as the surface pressure spectra in the turbulent boundary layer is converged.

2.4 Results

This section presents the baseline validation and aeroacoustics results of the numerical simulations followed by a discussion on the noise reduction mechanisms with the fence finlet designs.

2.4.1 Baseline Validation

Once the transients are removed from the 3-D simulations, the simulation data is averaged in time for approximately 2.5τ with 63,000 samples to predict the aerodynamic performance. Figure 3.7 (a) compares the predicted time- and span-averaged aerodynamic pressure coefficient (C_p) distributions of the baseline airfoil with experimental data and with XFOIL [53] predictions. The

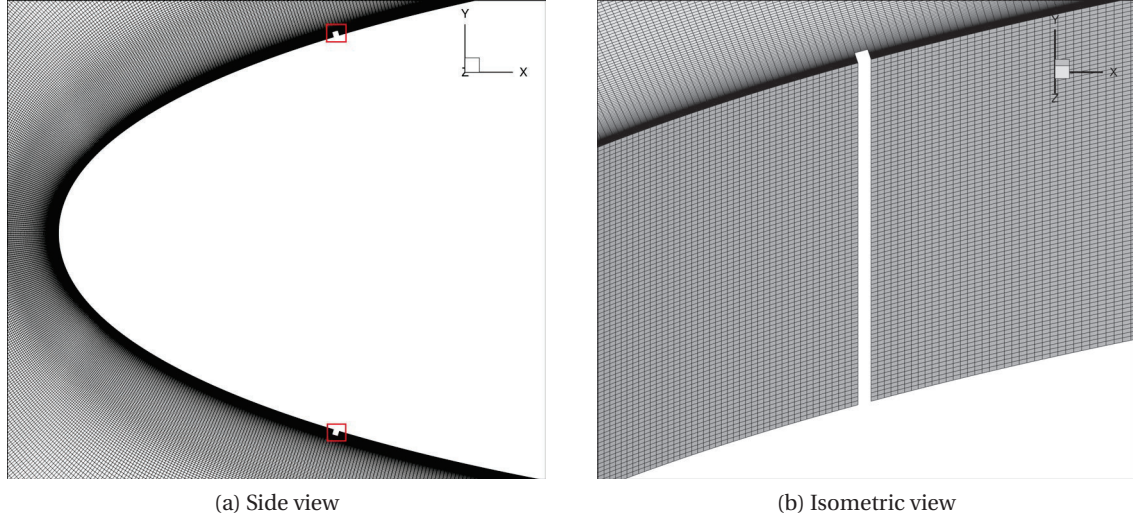


Figure 2.6: Mesh points that are blanked out to simulate the boundary layer trip wires (locations indicated with red squares in (a)). The nodes adjacent to the blanked-out points are assigned the no-slip wall boundary condition. The trip is applied across the entire length of the airfoil.

experimental measurements are for the NACA 0012 airfoil at $AOA = 0^\circ$ from Sagrado *et al.* [8] and Gregory *et al.* [54] at Re_c of 4×10^5 and 2.9×10^6 , respectively. The boundary layer is tripped on both surfaces of the airfoil. The trip is located at $x/c = 0.127$ in Sagrado *et al.* [8] and at $x/c = 0.05$ in Gregory *et al.* [54]. XFOIL results are also obtained with the boundary layer tripped at $x/c = 0.05$ and $Re_c = 5 \times 10^5$, which are the same conditions as in the FDL3DI simulation. The FDL3DI-predicted C_p agrees very well with the measured data over the entire airfoil except at the trip wire location where a spike is observed in the FDL3DI result. The agreement is better with the higher Re_c measurements. XFOIL does remarkably well in predicting the C_p distribution.

Figure 3.7 (b) compares the FDL3DI-predicted skin friction coefficient (C_f) distribution over the airfoil surface with the measured data from Sagrado *et al.* [8] and XFOIL, where excellent agreement is seen with both the measured data and XFOIL.

Figure 2.9 compares the baseline span-averaged normalized velocity profile, U^+ , for different chord locations on the upper side of the airfoil from $x/c = 0.58$ to $x/c = 0.95$. The viscous sublayer is well resolved. The slope in the log-law region is found to be $1/0.34$. While this value is slightly larger than the von Kármán constant ($= 1/0.41$), it is consistent with the measurements of Lee and Kang [5] of a turbulent flow over the NACA 0012 airfoil at $Re_c = 600,000$.

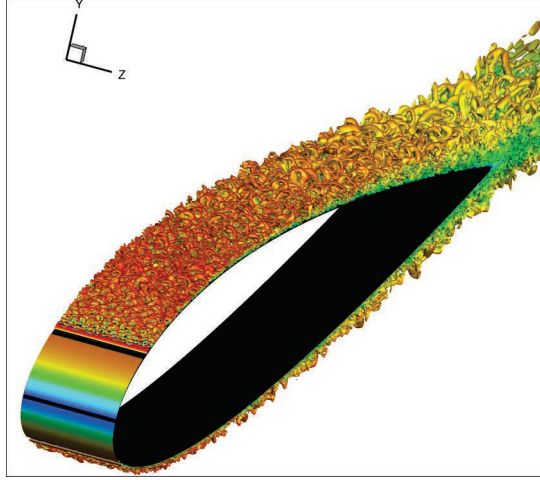


Figure 2.7: Iso-surfaces of the Q-criterion ($Q = 10$) of forced boundary layer transition from the geometry-resolved trip wire.

Figure 2.10 compares the normalized Reynolds stresses for the baseline airfoil as computed using a) the current FDL3DI simulations, b) the DNS of a turbulent boundary layer with an adverse pressure gradient by Spalart and Watmuff [6], and c) the LES of the NACA 0012 at $Re = 4 \times 10^5$ and $\alpha = 0^\circ$ by Wolf and Lele [7]. In the DNS, the Reynolds number based on the x -coordinate in the flow direction is $Re_x = 3.4 \times 10^5$. The pressure gradient parameter ($\beta = (\delta^*/\tau_w)dp/dx$), varies from 0 to 2 in the x direction, where the Reynolds stresses are at an x location corresponding to $\beta = 1$. The data from Ref. [7] and the current LES has a $\beta \approx 1$ at $x/c = 0.85$. Aside from the $\overline{u_1 u_1}$ peak near the wall in the DNS, good agreement is seen with the DNS results of Ref. [6] and with the LES results of Ref. [7].

Coherence squared, γ^2 , between two points \mathbf{x} and \mathbf{y} is defined as

$$\gamma_{xy}^2(\omega) = \frac{|S_{xy}(\omega)|^2}{S_{xx}(\omega)S_{yy}(\omega)}, \quad (2.3)$$

where $S_{xx}(\omega)$ is pressure spectral density, $S_{pp}(\omega)$ evaluated at point \mathbf{x} and $S_{yy}(\omega)$ is $S_{pp}(\omega)$ evaluated at point \mathbf{y} . For spanwise coherence, points \mathbf{x} and \mathbf{y} are at a given chordwise location (x/c) but separated in the span direction such that $\mathbf{y} = \mathbf{x} + \Delta z \hat{e}_k$, where \hat{e}_k is a unit vector along the span direction. The reference location to compute spanwise coherence is varied along the span. Each grid point is selected as a reference to compute one instance of coherence. All the instances of coherence so computed (101 in total) are then averaged to obtain the γ^2 reported here.

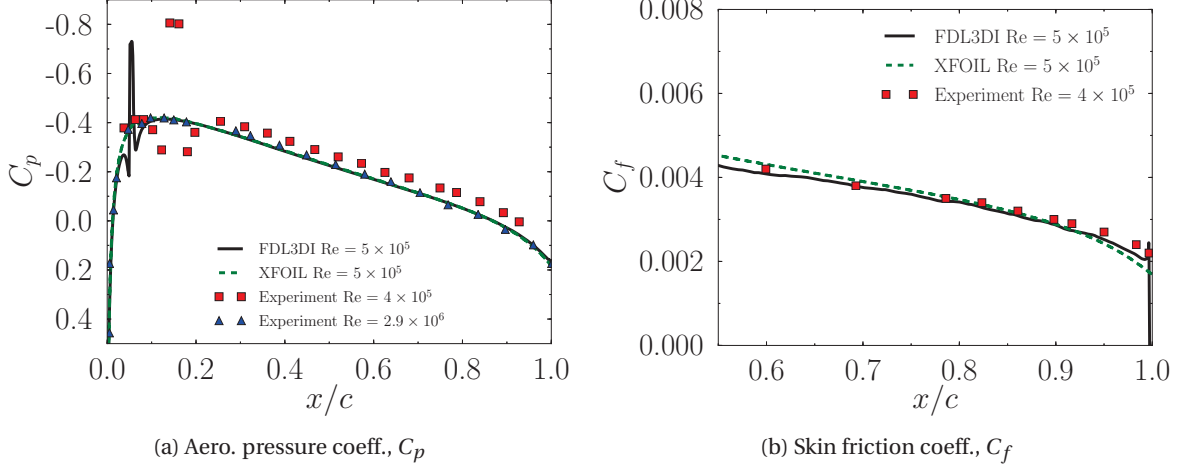


Figure 2.8: Time- and span-averaged C_p and C_f distributions from FDL3DI predictions ($Re_c = 5 \times 10^5$) compared with experiments ($Re_c = 4 \times 10^5$ and 2.9×10^6) and XFOIL simulations ($Re_c = 5 \times 10^5$).

Spanwise coherence is typically used to assess if a simulated span in an LES is sufficient for all sources of sound to radiate independently. For the baseline simulation, $\gamma_{xy}^2(\omega)$ is computed using Eq. 4.6 and the Welch method [55] with 2000 samples of data ($\approx 7\tau$) divided into 20 segments with a 50% overlap. The Hanning window is applied over each segment. Zero padding is not used in computing Fourier Transforms. Figure 2.11 plots the $\gamma^2(\omega)$ evaluated at three frequencies and at three x/c locations along the airfoil. The spanwise coherence decays to near zero suggesting that the span in the simulations is sufficient.

2.4.2 Surface Pressure Spectra

The primary noise generation mechanism in this low Mach number flow is the scattering into radiating sound of the hydrodynamic energy in the boundary layer turbulence by the airfoil trailing edge. Unsteady surface pressure near the trailing edge is therefore a measure of noise source strength. Surface pressure spectra are computed at $x/c = 0.975$. Numerical data is collected for approximately 5τ . Welch averaging is used with 1400 samples divided into 20 segments to reduce the scatter in the spectra. The spectra are also averaged over the span. The points that lie within the fences (marked as holes in the FDL3DI simulations) are removed in the averaging procedure.

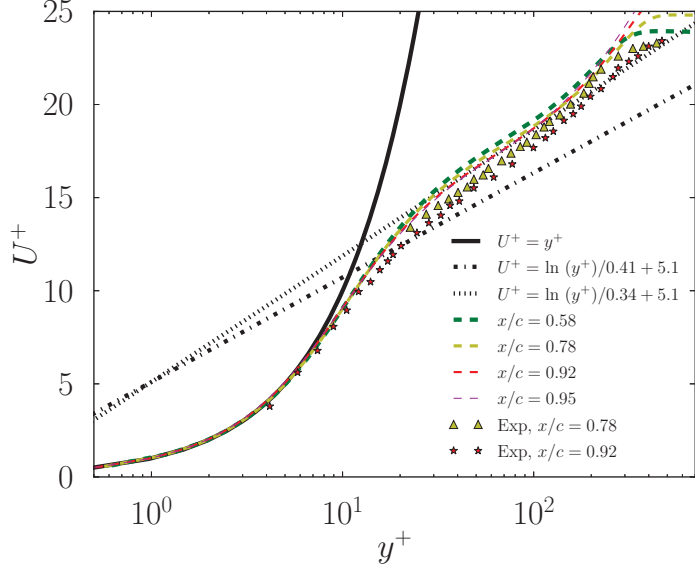


Figure 2.9: Baseline mean velocity profiles normalized by friction velocity plotted in wall units at different chord locations. Measurements are from Lee and Kang [5].

Figure 2.12 (a) compares the predicted surface pressure spectra near the airfoil trailing edge from the three simulations - one baseline and two fence simulations. Compared to the baseline, a measurable reduction at high frequencies and an increase at low frequencies are observed in the predicted surface pressure spectra with both the single-step and stair-step fence geometry. These observations are compared *qualitatively* with measured surface pressure spectra from Ref. [1] (Fig. 2.12 (b)). The figures show that the predictions agree qualitatively with the measurements – reduction is observed at high frequencies and an increase in spectral magnitude is observed at low frequencies. Interestingly, the surface pressure reductions near the airfoil trailing edge are found to be almost insensitive to the leading edge geometry of the fence.

2.4.3 Far field Aeroacoustics

Fluid dilatation ($\nabla \cdot v$) is representative of instantaneous acoustic perturbations. Figure 2.13 shows the dilatation field for the baseline simulation, where the broadband noise from the airfoil trailing edge can be seen. A clear tonal noise signature is visible in the simulation, which emanates from the trip wire located on the airfoil surface at $x/c = 0.05$. The tonal noise from the trip wire is present in all three simulations. Vorticity contours near the trip wire are shown in Fig. 2.14. The

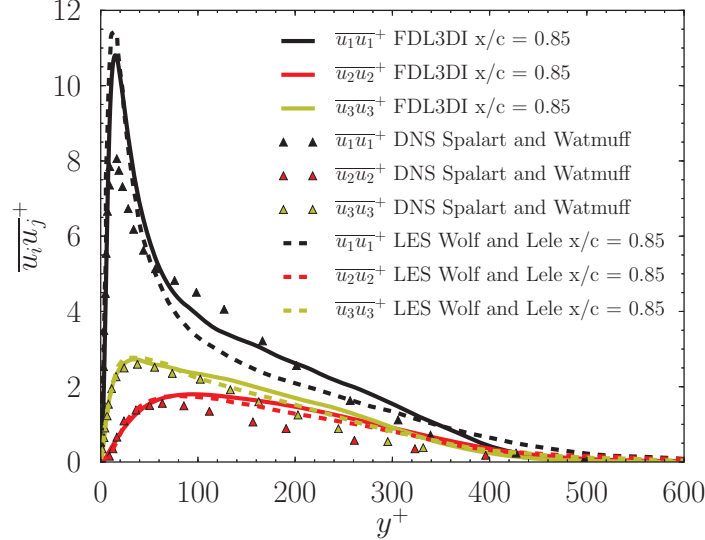


Figure 2.10: Comparison of FDL3DI predictions of normalized Reynolds stresses for the baseline airfoil with DNS results of a turbulent boundary layer in an adverse pressure gradient from Spalart and Watmuff [6], and an LES of a NACA 0012 at $Re = 4 \times 10^5$, $\alpha = 0^\circ$ from Wolf and Lele [7].

contour plot shows the flapping shear layer downstream of the trip wire that causes the extraneous noise. While this noise source is undesirable in the simulations, the frequency of this tone is much higher than the broadband noise frequencies of interest. In a linearized acoustics sense, the effect of this extraneous tone on the relevant broadband noise spectrum is ignored in the current predictions.

The in-house FW-H solver is used to calculate the far field noise. For the baseline airfoil, the integration (Kirchoff) surface can be selected as the airfoil surface. However, for the fence geometries, the FW-H surface has to include the walls of each fence to ensure that noise contributions from all surfaces are included. Sampling data on the fence surfaces is quite tedious as they cannot be defined as constant ξ , η , or ζ boundaries. A permeable surface is therefore selected that encloses the fences and the airfoil. Furthermore, the location of the permeable FW-H surface (marked with the red curve in Fig. 2.13) is chosen so that it is outside the undesired, high-frequency waves emanating from the trip wire. The integration surface extends from $-0.6 < x/c < 1.6$ and $-0.5 < y/c < 0.5$. Although the surface is not close to the airfoil, the grid is stretched very slowly up to the integration surface (stretching ratio < 1.06 near the FW-H surface). Therefore, the amount of numerical dissipation in the frequencies of interest is expected to be small.

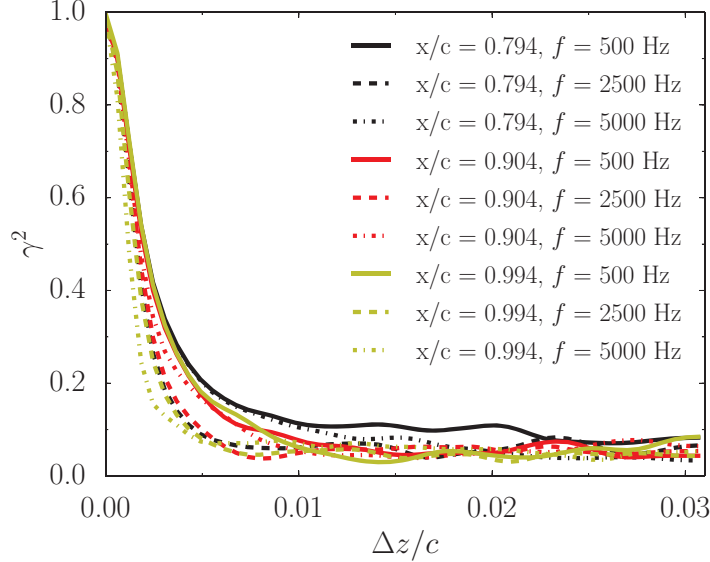


Figure 2.11: Spanwise coherence squared (γ^2) on the upper surface of the baseline airfoil at $x/c = 0.794$, 904, and 0.994 for $f = 500$, 2500, and 5000 Hz.

Figure 2.15 shows the predicted far field noise for the baseline and the two fences at polar angle, $\theta = 90^\circ$. The polar angle is measured from downstream and is positive in the counter-clockwise direction (see Fig. 2.13). The Power Spectral Density (PSD) is computed using the Welch method with 1200 samples ($\approx 4\tau$) divided into 13 segments and a 50% overlap between segments. Commensurate with the observed reductions in surface pressure spectra, the stair-step fence yields a substantial reduction in the farfield noise compared to the baseline between 500 Hz – 5 kHz. However, despite similar reductions in surface pressure spectra near the airfoil trailing edge with the single-step fence, no reduction is observed in the far field noise in the single-step simulation.

To investigate why the single-step fence does not yield farfield noise reduction, normalized unsteady surface pressure ($C_{p,\text{rms}}$) is investigated at $x/c = 0.87$, which is immediately upstream of the fence leading edge location. Figure 2.16 shows contours of $C_{p,\text{rms}}$ for the baseline, single-step, and stair-step fence simulations on a cross-stream plane at $x/c = 0.87$. Figure 2.17 quantitatively compares the span-averaged surface pressure spectra between the three geometries at $x/c = 0.87$. The single-step fence clearly has much higher unsteady surface pressure near the fence leading edge than the stair-step fence or the baseline airfoil. Contrasting this with the spectra comparisons near the airfoil trailing edge (see Fig. 2.12), we note that while the single-step fence geometry success-

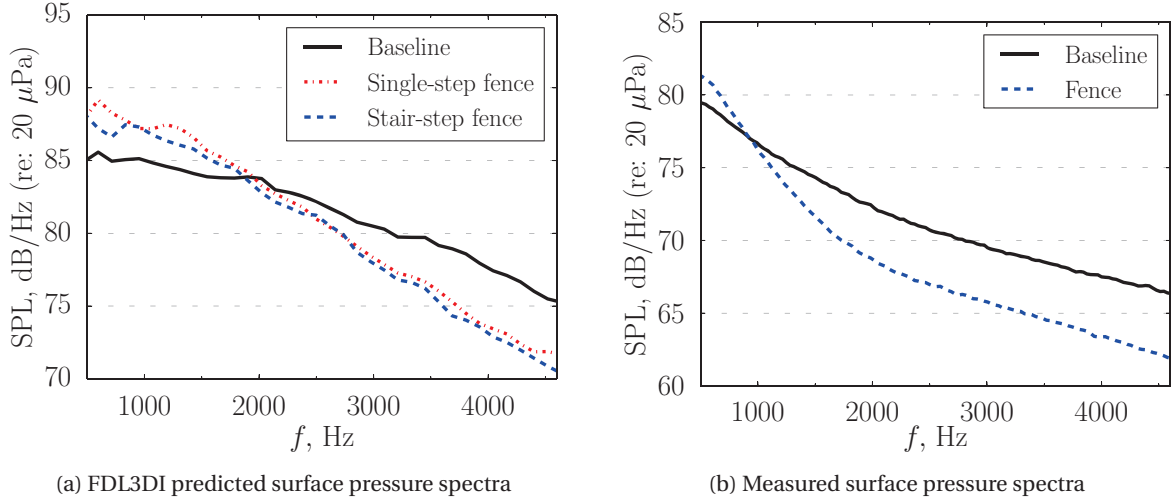


Figure 2.12: Qualitative comparison between the predicted and measured surface pressure spectra at the trailing edge $x/c = 0.975$. Measurements are from Ref. [1].

fully reduces the unsteady surface pressure near the airfoil trailing edge, it actually increases the unsteady pressure near the leading edge of the fences. We hypothesize that this unsteady pressure acts as localized lift on the leading edges of the fences in the single-step fence geometry and radiates as sound. This additional noise source offsets the benefit of reduced airfoil trailing edge noise due to the observed reduction in unsteady surface pressure there.

The predicted results for the stair-step fence geometry can be compared qualitatively with the measured farfield noise spectrum from Ref. [1] shown in Fig. 2.15 (b). The measured farfield noise was obtained using beamforming and integrating the one-twelfth octave band spectra over a two-dimensional area near the trailing edge. Although the difference in span lengths between the simulation and experiment is accounted for using Kato's correction [56], due to the difference in the baseline airfoil used between the simulations and the experiment, the SPL of the predicted and measured noise cannot be quantitatively compared. However, the predicted noise-reduction trends are consistent with the measurements. Little to no noise reduction is observed above 4 kHz and a noise reduction of up to 10 dB is observed between 1 kHz and 4 kHz. Clark [1] have suggested that the low frequencies (below 1 kHz) may have a facility noise contribution and hence any potential reduction in noise due to finlets at those frequencies will not be captured by the measurements. This may explain the differences in noise reduction with the finlets for frequencies below 1 kHz.

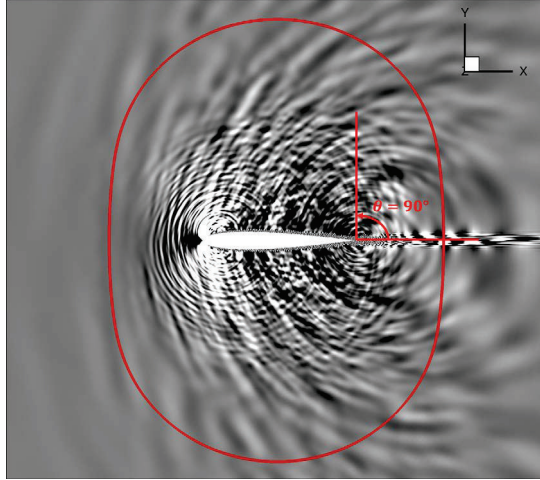


Figure 2.13: Fluid dilatation contours for the baseline simulation. The FWH integration surface is marked with the red curve. Observer angle (θ) is measured from downstream.

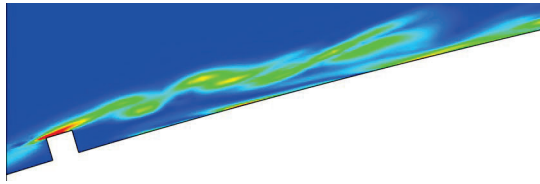


Figure 2.14: The shear layer behind the trip wire visualized using contours of vorticity magnitude.

2.4.4 Noise Reduction Mechanisms

Two hypotheses are put forth to explain the observed farfield noise reduction with the fence finlets: (1) the fences lift the turbulence eddies away from the scattering (airfoil trailing) edge, and (2) the fences reduce the spanwise correlation length. These hypotheses are investigated using the simulation results in this section.

Turbulence Kinetic Energy

To assess the first hypothesis, normalized turbulence kinetic energy (TKE) is obtained by averaging over 2.5τ . The TKE does not significantly change if more than 2.5τ of data is used for the averaging process. Contour plots of normalized TKE are compared between the baseline and the two fence simulations on cross-stream planes at two chordwise locations in Figs. 2.18 and 2.19. The plots show isometric views with the cross-stream cut planes. At $x/c = 0.85$, which is upstream of the

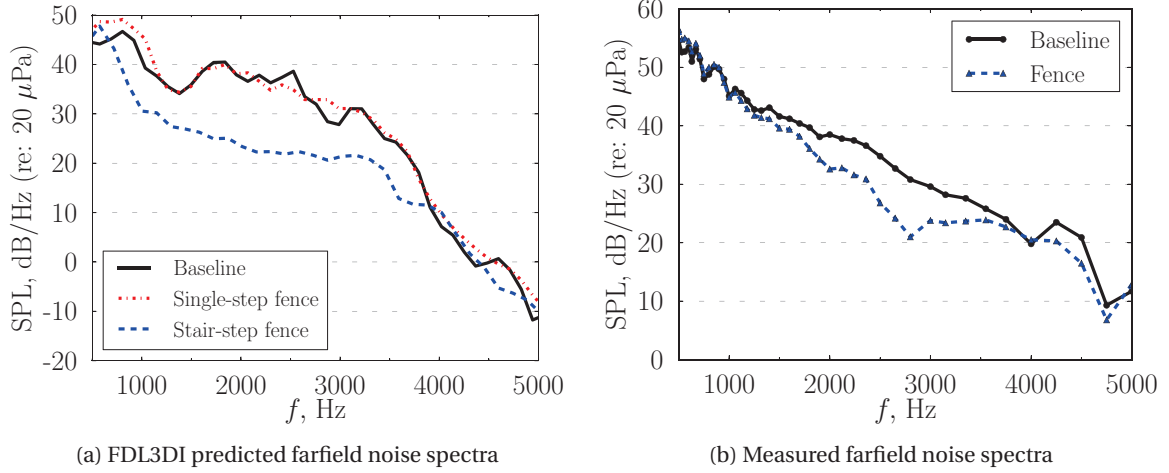


Figure 2.15: Qualitative comparison between the FDL3DI predicted and measured farfield noise spectra at an observer located at $\theta = 90^\circ$.

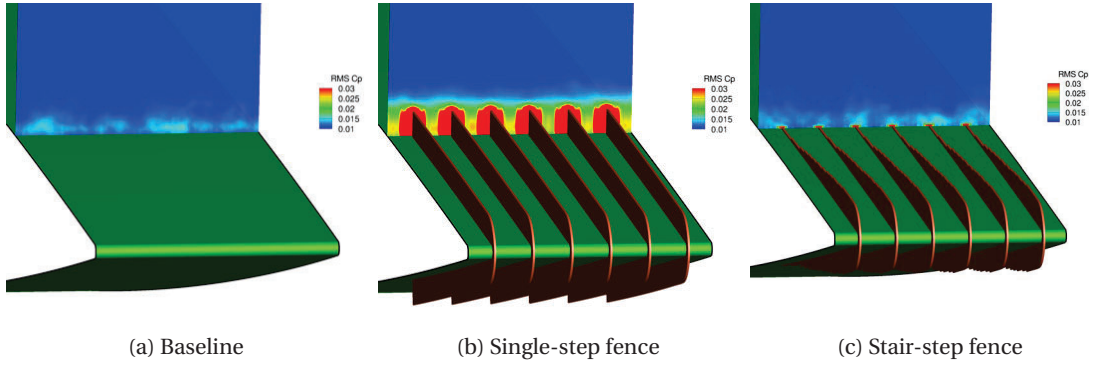


Figure 2.16: Contours of $C_{p,\text{rms}}$ on a cross-stream plane immediately upstream of the fence leading edge ($x/c = 0.87$).

fences, the TKE is concentrated in the boundary layer close to the airfoil surface in all three simulations (see Fig. 2.18). However, at the airfoil trailing edge, the TKE close to the airfoil surface (trailing edge) is substantially reduced with the fences, and appears to be concentrated above the fences (see Fig. 2.19). Figure 2.19 clearly shows that the separation distance between the source (unsteadiness in the turbulence) and the scattering airfoil trailing edge is increased. Afshari *et al.* [57] conducted an experiment with a similar finlet fence geometry installed over a flat plate at zero incidence. They observed similar trends as seen in the current predictions for turbulence intensity (TI); with the fences, the TI decreased near the flat plate and increased above the fences.

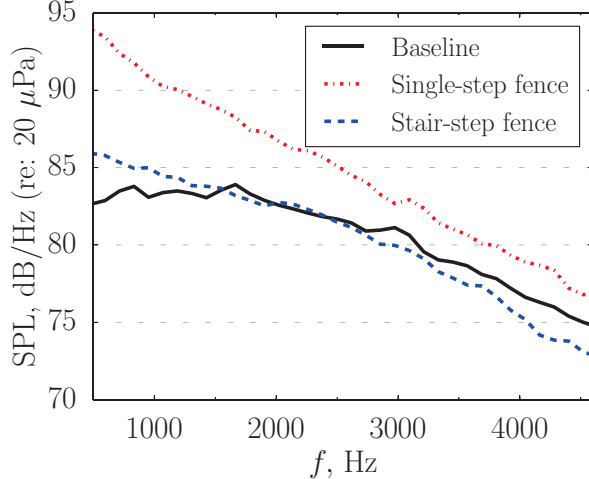


Figure 2.17: Comparison of unsteady surface pressure spectra at $x/c = 0.87$ between the baseline, single-step fence, and stair-step fence. The spectra has been averaged over the span.

Figure 2.20 compares the span-averaged TKE profiles between the baseline and the fence geometries at the two cross-stream locations corresponding to the plots in Figs. 2.18 and 2.19. The line plots quantitatively show the reduction in TKE near the surface and concentration of TKE above both the single-step and stair-step fences. Note that the ordinate in Fig. 2.20 is normalized by the maximum fence height, H . These results substantiate the first hypothesis for the observed reduction in unsteady surface pressure and the farfield noise with the fence finlets. While the TKE redistribution to the top of the fences also occurs with the single-step fence, the overall farfield noise is not reduced due to the additional noise source at the fence leading edge, as discussed earlier.

Spanwise Coherence

Amiet [40] provides an analytical expression for the farfield pressure PSD, $S_{pp}(\omega)$ of the sound radiated from a turbulent flow past the trailing edge of a half-plane. Per Amiet [40], $S_{pp}(\omega) \propto l_y(\omega) S_{qq}(\omega)$, where ω is the angular frequency, $S_{qq}(\omega)$ is the surface pressure PSD, and $l_y(\omega)$ is the spanwise correlation length of the pressure fluctuations. A reduction in spanwise coherence ($\gamma_{xy}^2(\omega)$), which is a measure of $l_y(\omega)$, can reduce the farfield noise even if the surface pressure PSD remains unchanged.

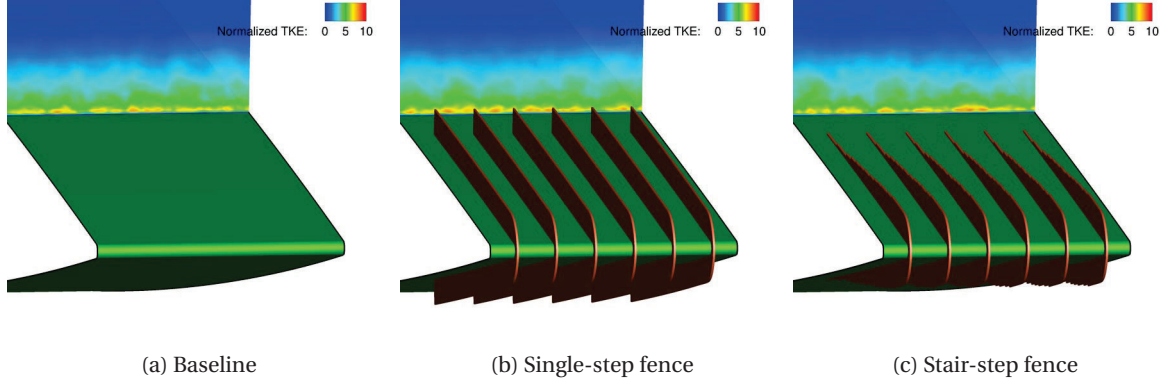


Figure 2.18: Normalized turbulent kinetic energy (k/u_t^2) contours for the baseline, single-step fence, and stair-step fence simulations at $x/c = 0.85$ (upstream of the fence).

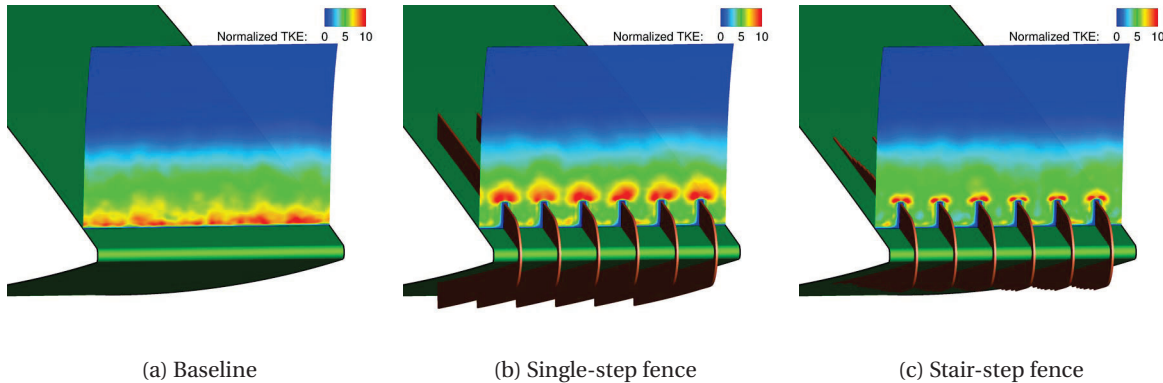


Figure 2.19: Normalized turbulent kinetic energy (k/u_t^2) contours for the baseline, single-step fence, and stair-step fence simulations at $x/c = 0.975$ near the airfoil trailing edge.

The procedure described in Section 3.4.1 is followed and Eq. 4.6 is used to compute $\gamma_{xy}^2(\omega)$ for the baseline and stair-step fence simulations. A total of 7.34τ of data, consisting of 2039 samples divided into 30 segments for spectral averaging is used for the calculations. Figure 2.21 compares γ^2 of the unsteady surface pressure near the trailing edge ($x/c = 0.97$) as a function of the spanwise separation distance ($\Delta z/c$) for the baseline and stair-step fence simulations. Coherence plots are drawn for two example frequencies to highlight the characteristics in the low- and high-frequency regions. The vertical dashed lines in the plots represent the spanwise location of the fences. The fences are equidistant and the fence pitch (distance between adjacent fence walls) is P .

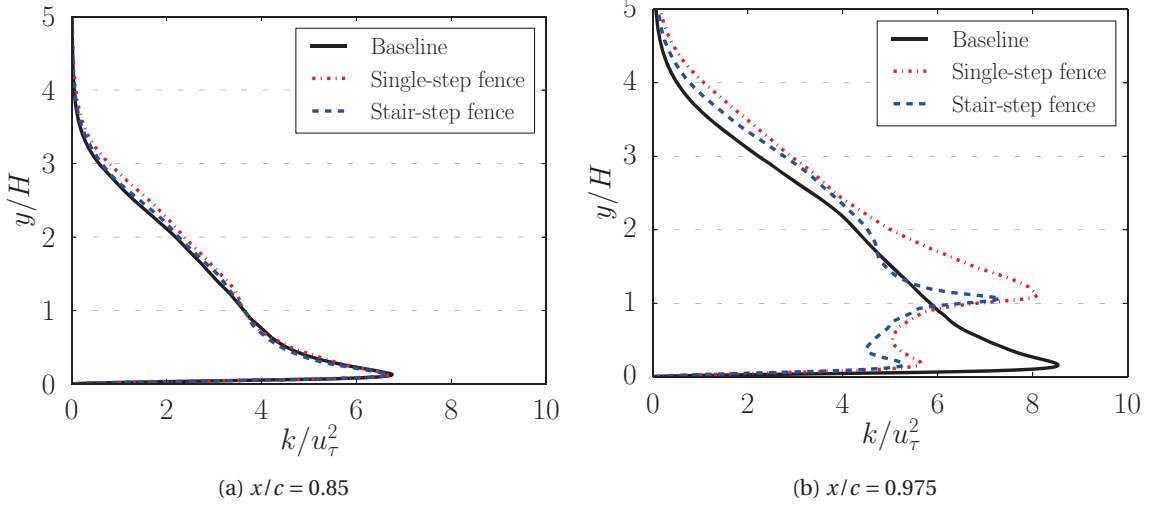


Figure 2.20: Span-averaged normalized turbulent kinetic energy (k/u_τ^2) profiles compared between the baseline and fence simulations: (a) upstream of the fence at $x/c = 0.85$, and (b) near the airfoil trailing edge at $x/c = 0.975$.

For separation distances greater than the fence pitch, i.e., $\Delta z > P$, we note that the fences reduce γ^2 at low frequencies (Fig. 2.21 (a)). At high frequencies, the coherence is already small for $\Delta z > P$ and the fences do not reduce it any further (Fig. 2.21 (b)). The simulation results show a farfield noise reduction at low frequencies with the stair-step fence despite an increase in the unsteady surface pressure PSD (see Figs. 2.12 (a) and 2.15). This analysis suggests that the reduction in spanwise coherence is responsible for the reduction in farfield noise at low frequencies.

This argument is supported by the following observation of the measurements by Clark [4]. Low-frequency noise reduction was observed in the experiments when the fence pitch was reduced (see Fig. 3.25). Since fences reduce γ^2 for spanwise distances greater than the fence pitch, a tighter pitch implies a reduction in span correlation length, and consequently a reduction in farfield noise.

2.5 Conclusions

This paper presents numerical investigations of airfoil geometries inspired by the down coat of the owl. The canopy effect of the down coat is achieved using the finlet fences proposed by Clark *et al.* [3]. Large eddy simulations are performed for the baseline (NACA 0012) airfoil and two airfoils with the finlet fences. The baseline simulation results are validated against measured data avail-

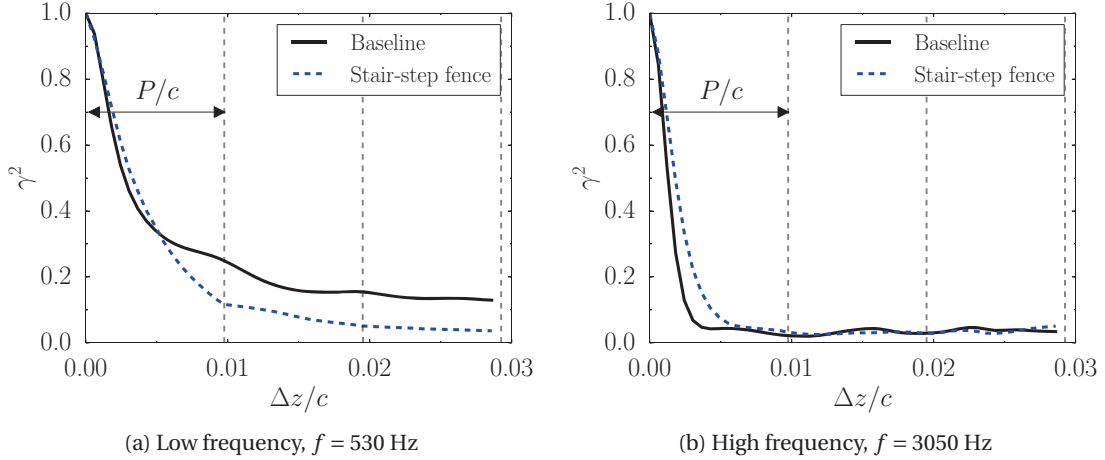


Figure 2.21: Spanwise coherence, $\gamma^2(\omega)$ of unsteady surface pressure at the trailing edge $x/c = 0.97$ for a) low, and b) high frequencies.

able in the literature for aerodynamic pressure coefficient (C_p) and boundary layer profiles, and against previous DNS and LES results for Reynolds stresses. Qualitative comparisons are drawn with experiments with the fences to verify the trend prediction ability of the approach. The following conclusions are drawn from the study.

1. Comparisons of surface pressure spectra show a reduction at high frequencies and a slight increase in the low frequencies near the airfoil trailing edge with the fences.
2. Farfield noise spectra comparisons show reductions of up to 10 dB at frequencies ranging from 500 – 5000 Hz for the stair-step fence simulation; no reductions are observed for the single-step fence simulation.
3. Contour plots and span-averaged profiles of normalized turbulence kinetic energy (TKE) show a clear redistribution of TKE away from the airfoil trailing edge.
4. A comparison of the spanwise coherence of the unsteady surface pressure shows that the stair-step fence reduces γ^2 at low frequencies for normalized separation distances $\Delta z/c > P/c$.

The results show that one of the reasons for the observed noise reduction with the fences is the increased source-scattering edge separation distance, which makes the edge scattering process less efficient. Another mechanism of farfield noise reduction at low frequencies is identified to be

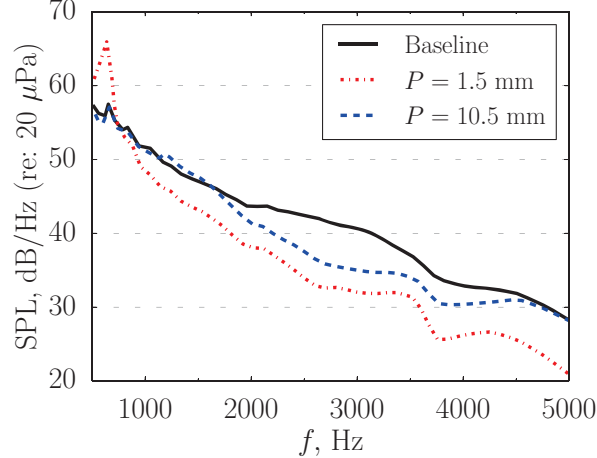


Figure 2.22: Measured farfield noise spectra from Clark *et al.* [4] showing the effect of fence spacing. For all cases, the maximum height of the fences, $H = 4 \text{ mm}$.

a reduction in spanwise coherence. The lack of farfield noise reduction from the single-step fence demonstrates the importance of having the fence leading edge nearly aligned with the incoming flow.

CHAPTER 3. NUMERICAL INVESTIGATION OF LOW-NOISE AIRFOILS INSPIRED BY THE DOWN COAT OF OWLS

This chapter was published in the Bioinspiration and Biomimetics Journal in 2018. [10]

Abstract

Numerical analysis of airfoil geometries inspired by the down coat of the night owl is presented. The bioinspired geometry consists of an array of “finlet fences”, which is placed near the trailing edge of the baseline (NACA 0012) airfoil. Two fences with maximum nondimensional heights, $H/\delta^* = 1$ and 2.26 are investigated, where δ^* is the displacement thickness at 2.9% chord upstream of the airfoil trailing edge. Wall-resolved large eddy simulations are performed at chord-based Reynolds number, $Re_c = 5 \times 10^5$, flow Mach number, $M = 0.2$, and angle of attack, $\alpha = 0^\circ$. The simulation results show significant reductions in unsteady surface pressure and farfield radiated noise with the fences, in agreement with the measurements available in the literature. Analysis of the results reveals that the fences increase the distance between the boundary layer turbulence (source) and the airfoil trailing (scattering) edge, which is identified to be the mechanism behind high-frequency noise reduction. These reductions are larger for the taller fence as the source-scattering edge separation is greater. Two-point correlations show that the fences reduce the spanwise coherence at low frequencies for separation distances greater than a fence pitch (distance between two adjacent fences) and increase the coherence for smaller distances, the increase being higher for the taller fence. This increase in coherence and the reduced obliqueness of the leading edge of the fence are hypothesized to be responsible for the small increase in farfield noise at low frequencies observed in the simulations with the taller fence.

3.1 Introduction

Noise generated due to fluid flow and its interaction with solid surfaces is termed aerodynamic noise. Aerodynamic noise due to the interaction of the turbulence in the boundary layer over a blade with the blade surface is often referred to as “self” noise [16]. Self noise can be generated via different mechanisms: separation stall noise, laminar boundary layer-vortex shedding noise, tip vortex formation noise and trailing edge noise. This paper focuses on trailing edge noise; specifically on its mitigation through bioinspired blade designs.

Trailing edge noise is broadband in nature and is generated by scattering of the hydrodynamic energy in a turbulent boundary layer into acoustic radiation. The turbulent fluctuations in the boundary layer can radiate sound directly (with a sound power scaling of M^8 , where M is the flow Mach number), but it is their close proximity to the airfoil surface that amplifies the sound produced in subsonic flow (sound power scaling becomes M^6) [39]. This amplification is due to the unsteady surface pressure on the airfoil surface (generated by the turbulent boundary layer) which radiates more efficiently than free turbulence when the flow Mach number is small (≤ 0.2). Furthermore, when the surface has a singularity, such as at the airfoil leading and trailing edges, the sound radiation becomes even more efficient (sound power scaling of M^5) [38, 40, 58]. Trailing edge noise is therefore a dominant noise source in blades operating in clean flow (low inflow turbulence) at low Mach number. These conditions are realized in wind turbine blades [21], civil aircraft during approach and takeoff, underwater vehicles [59], household fans, HVAC blowers, etc. The long term goal of the aviation industry to reduce aircraft noise by 20 dB [18] cannot be achieved without mitigating trailing edge noise. Growth of the wind energy industry is also curtailed due to the annoyance caused by rotor blade noise, which is predominantly trailing edge noise.

A variety of innovative technologies have been developed using biomimicry [22], e.g., self-cleaning paints using the lotus leaf effect, [24] temperature-regulated buildings inspired by termite mounds, [23] etc. Nature has also provided a solution for silent flight in night owls [26, 25]. Night owls require the acoustic stealth to avoid aural detection by the prey and also to aurally locate their prey in the dark. [27] A night owl can not be heard until it is within three meters of its prey. [2] One species of night owls – the barn owl (*Tyto alba*) – is particularly skilled at silent flight. Hereinafter, we shall refer

to the barn owl as “the owl”. While this biological marvel has been known to mankind for almost a century, it is yet to find its due engineering application.

Previous investigations [25, 26, 2] have found three important anatomical features that presumably play a role in reducing noise during owl flight. These features are collectively referred to as the owl “hush kit”. The hush kit comprises of

1. A stiff comb-like structure (referred as serrations) at the leading edge (LE) of the wing,
2. A flexible fringe like structure at the trailing edge (TE) of the wing, and
3. A soft, thick down coat on the flight feathers.

It is emphasized that the chord-based Reynolds number for the owl in flight is between 50,000 – 90,000. The applications of interest, such as aircraft wings and wind turbine blades, operate at much higher Reynolds number. The objective therefore is to take inspiration from the night owl, rather than replicate its anatomy, to design ultra-quiet blade designs.

Owl-inspired LE and TE designs (serrations) have been developed and investigated extensively in laboratory [29, 30, 31, 28] and in the field [32]. This paper focuses on the third owl feather feature in the list above – the down coat, which has not received as much research attention until recently. Geyer *et al.* [33] related the down coat to the porosity of a wing. By doing a series of experiments that used airfoils made out of different porosity materials, they found that at the frequencies less than about 10 kHz, porous airfoils were able to attenuate the trailing edge broadband noise by over 10 dB. However, the aerodynamic performance decreased as the resistivity of the airfoils increased with porosity. Jaworski and Peake [34, 35] analyzed the trailing-edge condition and found that the fifth-power (M^5) dependency of the radiated acoustic power of a trailing edge was weakened by both porosity and flexibility. However, they did not investigate the effect of the feather structure formed by the hairs on the flight feathers of the owl.

Microscopic observations by Clark *et al.* [3] revealed that hairs on owl feathers rise vertically up from the feather substrate (lifting surface of the wing) and then plateau out in the streamwise direction, forming a structure similar to a forest/plant canopy. [3] Fluid flow in plant canopies has been investigated elsewhere [36]. Clark *et al.* [3] found that the owl canopy has an open area ratio of about 70% and is suspended approximately 0.5 mm above the feather substrate. Based on these

observations, they designed artificial canopies with different open area ratios and performed wall-jet wind tunnel experiments to examine the effect of the canopies on surface roughness noise. The canopies were designed using a large number of parallel fibers made from the material used for fishing lines. These fibers were oriented in the direction of the flow and located just above the flow surface. The canopies were found to reduce both the surface pressure fluctuations (by as much as 30 dB!) and the radiated farfield noise.

This exciting discovery motivated them to develop trailing edge noise reduction designs. These designs also used the concept of canopy, but were designed to be robust enough for industrial application, e.g., on wind turbine blades. The designs presented in Clark *et al.* [4] achieved the canopy effect by attaching small structures (height less than the boundary layer) near the trailing edge, which they called “finlets”. Figure 3.1 shows schematics of two finlet designs, finlet fence and finlet rail, used in these experiments. Twenty different configurations of these two designs were tested in the experiments by changing the height, spacing, thickness, and extension of the fences and rails. Compared to the unmodified (baseline) airfoil, these configurations were found to reduce the trailing edge noise by up to 10 dB [4].

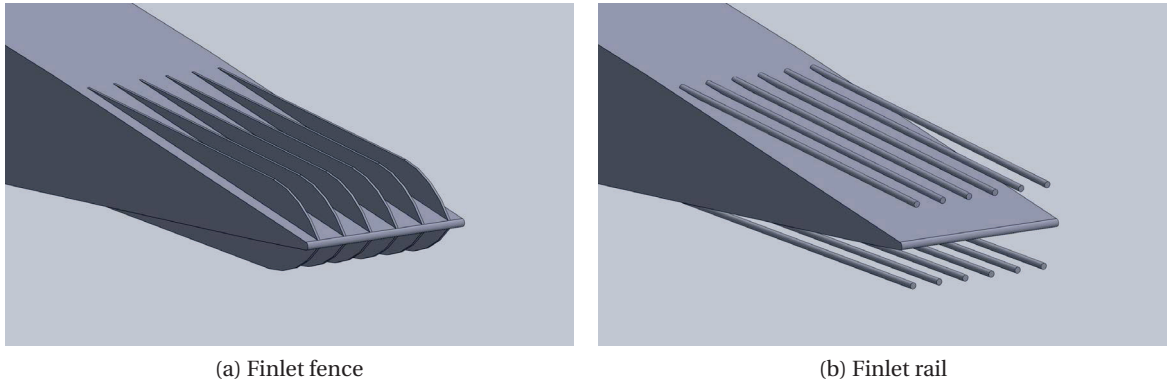


Figure 3.1: Idealized representations of the a) finlet fence and b) finlet rail designs which were experimentally investigated in Ref. [4]. The struts to support the finlet rails are omitted for clarity.

Based on the results of the different configurations tested, the finlets are believed to: (a) lift the energetic eddies in the turbulent boundary layer away from the airfoil trailing edge, thereby reducing the scattering efficiency, and (b) reduce spanwise coherence in the boundary layer. These are the working hypotheses behind the observed noise reduction. The objective of this paper is to use

high-fidelity aeroacoustics simulations to determine the mechanisms behind the observed noise reduction to verify or disprove the working hypotheses.

Highly-resolved large eddy simulations are conducted for the baseline airfoil (NACA 0012) as well as the baseline airfoil fitted with two different fence finlet designs. It should be noted that the baseline airfoil in the experiments of Ref. [4] was different. The experiments used the DU96-W-180 airfoil, which is commonly used in the design of the tip section of utility scale wind turbines. Furthermore, the simulations are performed at a smaller Reynolds number compared to the experiments – $Re_c^{(\text{sim})} = 5 \times 10^5$ versus $Re_c^{(\text{exp})} = 2.5 \times 10^6$. These simplifications are made to manage the computational complexity of the problem; the intent here is to focus on the physical phenomena behind noise reduction rather than perform a direct validation (one-to-one comparison) with the experimental data. Nevertheless, the simulations reveal several interesting flow physics that shed new light on the physical mechanisms behind the observed noise reduction.

This research builds upon authors' recent work in simulating fence finlets [44, 45, 41]. Bodling *et al.* [41] investigated the aeroacoustic impact of the shape of the leading edge of the finlet fences and found that it has to be highly skewed (oblique incidence) to the incoming flow to achieve noise reduction. They also noted that the fence finlets indeed increase the separation distance between the energetic turbulent eddies and the airfoil trailing (scattering) edge. In this article, we study the effect of varying the height of the finlet fences to bolster our understanding of the noise reduction mechanisms. Results from three sets of simulations are presented and compared: baseline airfoil, and baseline airfoil fitted with two fence finlets with maximum fence heights $H/\delta^* = 1$ and 2.26, where δ^* is the displacement thickness at 2.9% chord upstream of the airfoil trailing edge. Displacement thickness is chosen as the reference length scale for noise analysis as the main mechanism of noise reduction is believed to be displacement of energetic turbulent eddies away from the airfoil trailing edge. Figure 3.2 shows the two fence finlet geometries used in the simulations. Given the differences in the airfoil geometries between the simulations and the fence finlets experiment [4], the comparisons are drawn to test for *trend* prediction rather than a quantitative verification; absolute validation against aerodynamic measurements for the baseline airfoil are presented in the paper to demonstrate solver accuracy. The objective is to perform source diagnostics using the highly-

resolved flowfield to enhance our understanding of the mechanisms behind the noise reduction observed with finlets.

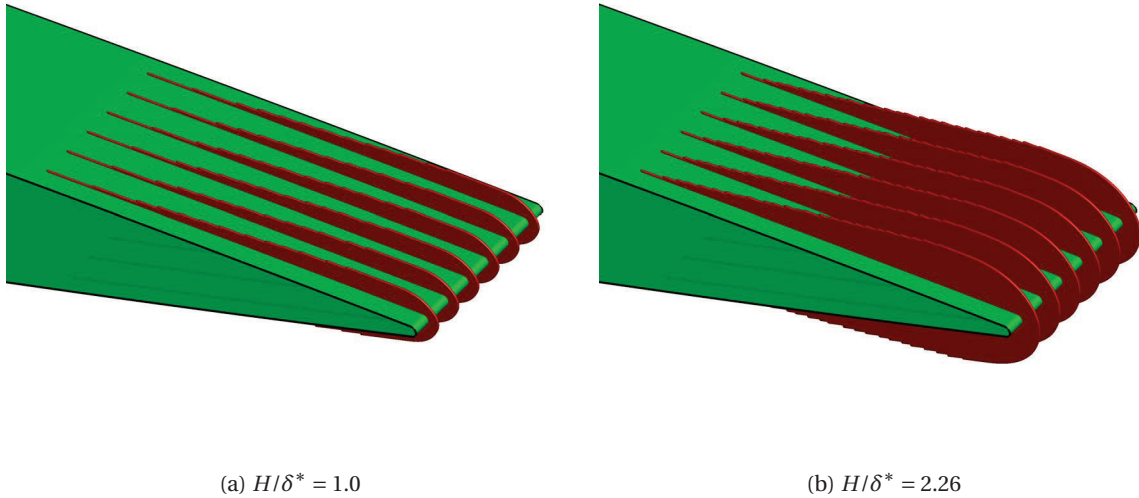


Figure 3.2: Geometry of the two fence configurations used in the simulations with maximum normalized fence heights, H/δ^* = a) 1.0 and b) 2.26. The maximum fence height occurs at $x/c = 0.971$.

3.2 Numerical Methodology

The aeroacoustic performance of the baseline and finlet fence models is evaluated using a two-step approach. First, the unsteady flow around the geometry is simulated using a computational fluid dynamics (CFD) solver; time-accurate flow data is collected during the CFD simulation on a surface enclosing the airfoil and the sound sources. In the second step, the surface data is used with an integral method (acoustic analogy) to predict the farfield noise radiation. The numerical procedure used in this work has been previously validated and used to assess the noise reduction ability of leading edge serrations [28] and finlets [44, 45, 41].

3.2.1 Compressible Flow Solver

Aeroacoustics simulations require resolution of wide ranges of spatial, temporal, and energy scales because of the requirement to simultaneously compute hydrodynamic and acoustic fields in the flow. Very high accuracy is therefore required of such solvers even when they are coupled with

integral methods for farfield noise prediction as the solver still has to accurately compute the tiny acoustic perturbations alongside the unsteady hydrodynamic field. For the present work, the compressible Navier-Stokes solver, FDL3DI [46], is used for the flow simulations. FDL3DI solves the full unfiltered compressible Navier-Stokes equations on curvilinear meshes. The governing fluid flow equations, after performing a time-invariant curvilinear coordinate transform $(x, y, z) \rightarrow (\xi, \eta, \zeta)$, are written in a strong conservation form as

$$\frac{\partial}{\partial t} \left(\frac{\mathbf{U}}{J} \right) + \frac{\partial \hat{\mathbf{F}}_I}{\partial \xi} + \frac{\partial \hat{\mathbf{G}}_I}{\partial \eta} + \frac{\partial \hat{\mathbf{H}}_I}{\partial \zeta} = \frac{1}{Re} \left[\frac{\partial \hat{\mathbf{F}}_v}{\partial \xi} + \frac{\partial \hat{\mathbf{G}}_v}{\partial \eta} + \frac{\partial \hat{\mathbf{H}}_v}{\partial \zeta} \right], \quad (3.1)$$

where J is the Jacobian of the coordinate transformation, $\mathbf{U} = \{\rho, \rho u, \rho v, \rho w, \rho E\}$; the expressions for the inviscid flux terms, $\hat{\mathbf{F}}_I, \hat{\mathbf{G}}_I, \hat{\mathbf{H}}_I$, and the viscous flux terms, $\hat{\mathbf{F}}_v, \hat{\mathbf{G}}_v, \hat{\mathbf{H}}_v$, are available in Ref. [46].

The *implicit* large eddy simulation (LES) approach is used for the simulations. Unlike traditional LES, the governing equations are not filtered. As a result, there are no additional sub-grid stress terms to model the dissipation of the unresolved, small-scale flow structures. These sub-grid flow structures are removed (filtered out) from the solution by applying discriminating, high-order (up to 10th order), low-pass spatial filters to the conserved flow variables. The filter is discriminating in the sense that it only removes wavenumbers that cannot be resolved by the grid. The filtering procedure is applied after each timestep. The implicit LES approach effectively becomes Direct Numerical Solution (DNS) in the limit of grid refinement reaching the Kolmogrov scale.

The filter used in the interior nodes has the following stencil,

$$\alpha_f \hat{\phi}_{i-1} + \hat{\phi}_i + \alpha_f \hat{\phi}_{i+1} = \sum_{n=0}^N \frac{a_n(\phi_{i-n} + \phi_{i+n})}{2}, \quad (3.2)$$

where α_f is the free parameter that provides some control on the “degree” of filtering, ϕ is the solution before filtering, $\hat{\phi}$ is the filtered solution, a_n is the set of coefficients for a given order of accuracy of the filter and $2N$ is the order of accuracy of the filter which has a stencil of $2N + 1$ points. An 8th-order filter with $\alpha_f = 0.45$ is applied on the interior nodes in the simulations presented here. One sided filters are used at the boundaries. Details of the filtering strategy used at boundaries are discussed in appendix A.

To discretize the spatial domain, up to sixth-order accurate compact finite difference schemes are used. Time integration is performed using the second-order accurate Beam-Warming implicit

scheme [60, 61]. The FDL3DI solver uses the overset (Chimera) mesh approach to handle complex geometries where the fluid domain can be discretized using multiple overlapping blocks. High-order (10th) interpolation is used for communication between the blocks to maintain the spectral-like accuracy of the solver. A 5-point overlap is used to enable 10th-order interpolation. The decomposed grid is solved in parallel using a hybrid MPI-OpenMP approach; MPI refers to message passing interface. Message passing is used with domain decomposition for data parallelism, and multithreading is used to further boost the parallel performance of the software on multi-core processors.

3.2.2 Prediction of Farfield Noise

Farfield sound propagation is performed using the Ffowcs Williams-Hawkins (FW-H) acoustic analogy [47]. By neglecting volume sources (valid for low Mach number flows), the following integral equation is obtained for far-field acoustic pressure, p' at location \mathbf{x} and time t :

$$p'(\mathbf{x}, t) = \frac{1}{4\pi|1-M_r||\mathbf{x}|} \left(\frac{\partial}{\partial t} \iint [\rho_0 u_i n_i + \rho'(u_i - U_i) n_i] d\Sigma + \frac{x_i}{c|\mathbf{x}|} \frac{\partial}{\partial t} \iint [p' n_i + \rho u_i (u_j - U_j) n_j] d\Sigma \right), \quad (3.3)$$

Solving Eq. 3.3 requires integrating over a surface Σ that encloses all sound sources. In the above, n_i is normal to the surface Σ , p' and ρ' are pressure and density fluctuations, ρ_0 is mean density, u_i is perturbation flow velocity and U_i is the velocity of the surface Σ . The source is at the origin, and \mathbf{x} denotes the observer location. We choose a “porous” surface around the airfoil defined by one of the gridlines ($\xi = \text{constant} > 1$; $\xi = 1$ is the airfoil surface) of the grid block. The FW-H solver has been validated previously against canonical problems (point monopole, dipole, and quadrupole) as well as against experimental data for aerodynamic noise from propellers [48]. The FW-H solver has also been verified against computational results for point sources in a moving medium (see appendix B).

3.2.3 Kato's Correction

The span of the airfoil in the simulations, S_s is less than the span of the airfoil used in the experiments, S_e of Ref. [4]. Therefore, the predicted farfield noise needs to be corrected before comparing to the experimental data. The correction depends on the spanwise coherence length L_c . When the coherence length is less than the simulated span, as is the case for the simulations presented here,

the following equation is used to compare the measured and predicted farfield sound spectra S_{pp} .

$$(S_{pp}(\omega))_e = (S_{pp}(\omega))_s + 10 \log(S_e/S_s), \quad L_c < S_s < S_e \quad (3.4)$$

Equation 3.4 assumes that over the span length of L_c there is perfect correlation, and outside of this length the correlation drops identically to zero. This “box-car” simplification by Kato and Ikegawa [56] is often used in such aeroacoustic predictions.

3.3 Geometry Modeling, Meshing, and Boundary Conditions

The NACA0012 airfoil is selected as the baseline airfoil. For the bioinspired airfoil, finlet fences are added near the airfoil trailing edge. The span length of all the models in the simulations is 5.85% of the airfoil chord. Two-point correlation analysis presented in Ref. [41] demonstrated that this span length is adequate to ensure that the sound sources radiate independently.

A single-block, O-grid is used to generate a 2-D mesh around the baseline airfoil, which is repeated in the span direction to obtain the 3-D grid. The near-wall mesh is obtained by normal extrusion from the airfoil surface with a high degree of refinement near the walls. The O-grid in the physical space (x, y, z) maps to an H-grid in the computational domain (ξ, η, ζ) . The following orientation is used: \hat{e}_ξ points radially out, \hat{e}_η is in the circumferential direction, and \hat{e}_ζ is along the span direction following the right hand rule, $\hat{e}_\zeta = \hat{e}_\xi \times \hat{e}_\eta$. In the baseline grid used in this study, the O-grid distribution on the z-constant planes is similar to that described in Ref. [49], which was a LES of flow over an airfoil at $Re_c = 5 \times 10^5$. Based on the mesh sensitivity study performed in Ref. [49] and the recommendations from Georgiadis *et al.* [50], the grid spacing on the suction side was found to be appropriate for LES. In the work from Ref. [49], only the suction side was resolved. Therefore, to create the grid used in this study, the suction side of the grid from Ref. [49] was mirrored in order to resolve both sides of the airfoil.

Periodic boundary condition is used in the span (\hat{e}_ζ) and azimuthal (\hat{e}_η) directions using overset grid with five-point overlaps. The airfoil surface is modeled as a no-slip, adiabatic wall with a zero-normal pressure gradient (4th-order extrapolation). The outer computational domain boundary is approximately 110 chords away from the airfoil and is prescribed as a freestream boundary. The grid is heavily stretched away from the airfoil such that the filtering procedure annihilates all fluctuations

before they reach the outer boundary and avoids spurious reflections. The computational time step, $\Delta\tau = \Delta t U_\infty / c$ is chosen to be small ($= 4 \times 10^{-5}$) to provide sufficient temporal resolution of the fine-scale features. In the above, c is airfoil chord, t is the dimensional time, and U_∞ is the freestream flow speed.

3.3.1 Baseline Airfoil Mesh

The baseline geometry is a NACA 0012 airfoil with a rounded trailing edge with $h/\delta^* \approx 0.3$, where h is the thickness of the trailing edge. According to Blake [59], this corresponds to a blunt trailing edge. The simulations are carried out at chord-based Reynolds number, $Re_c = 5 \times 10^5$, angle of attack, $\alpha = 0^\circ$, and flow Mach number, $M_\infty = 0.2$. The choice of the first cell height with these flow conditions gives an average y^+ of 0.567 for the baseline geometry. The turbulent boundary layer is well resolved. As an example, the boundary layer at $x/c = 0.85$ contains 110 grid points with approximately 15 points in the viscous sublayer. The maximum grid stretching ratio at the top of the boundary layer is 1.04. Figure 3.3 shows close-up, cross-sectional views of the baseline O-grid. For clarity, every fourth point in the radial and circumferential direction is shown in Fig. 3.3.

Table 3.1 provides the grid dimensions and first non-dimensional cell sizes in wall units averaged over the turbulent flow region. The cell sizes are also averaged along the span. Typical values of cell sizes used in previous wall-resolved LES available in the literature are $50 \leq \Delta x^+ \leq 150$, $y_{wall}^+ < 1$, $15 \leq \Delta z^+ \leq 40$, where x is the streamwise direction, y is the wall normal direction and z is in the spanwise/homogeneous direction [50]. The values used here (see Table 3.1) are on the lower range of the values reported in literature.

Table 3.1: The baseline grid dimensions and non-dimensional cell sizes in wall units. Average and max values are obtained over the turbulent flow region.

$N_\xi \times N_\eta \times N_\zeta$	Δy^+ avg, max	Δx^+ avg, max	Δz^+ avg, max
$410 \times 1937 \times 101$	0.567, 0.665	28.7, 37.1	14.9, 17.3

3.3.2 Finlet Fence Geometry and Mesh

The fence finlets used in the experiment are flushed with the airfoil and rise at a very shallow angle from the airfoil. Generating a structured mesh around such a geometry while maintaining a

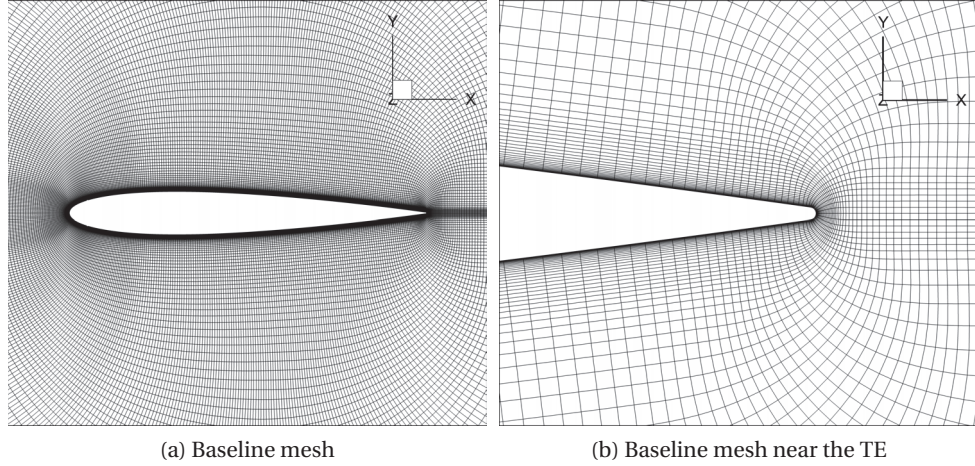


Figure 3.3: O-grid topology of the baseline mesh used in the simulation. The trailing edge is rounded and the mesh near the TE is shown in (b). Every fourth point along each axis is shown for clarity.

reasonable mesh quality and manageable cell count is nearly impossible. Therefore, alternate geometry configurations are sought for which “practical” meshes (i.e., meshes with manageable grid count and cell aspect ratios, skewness, etc. that do not render the numerical algorithm unstable) can be obtained. The fences are modeled as a “stair-step” geometry by varying the height of the fences in discrete steps (as opposed to continuous variation in the experiment model) along the chord. Such approximation of the fence geometry is justified considering that the objective is to identify the underlying flow physics behind the observed noise reduction with the fences. Note that the leading edge of each step, which is orthogonal to the oncoming turbulent flow is a scatterer of sound, it is very small ($\sim 1\text{-}2\%$ of boundary layer thickness, δ) compared to the size of the energy-containing turbulent eddies ($\sim \delta$). Therefore any impact of such a stair-case representation of the fence geometry is limited to very small eddies of the boundary layer turbulence which are not important in generating sound in the human-audible frequency range.

A large number of steps are used to approximate the fence geometry as a stair-step such that it closely approximates the continuous geometry of the experiment. For the smaller fence, the final height is reached over 13 discrete stair-steps. Figure 3.4 shows a schematic of the modeled fence geometry with a nomenclature of the key dimensions.

The meshes for the fence simulations are obtained from the baseline mesh by performing *hole-cutting* (also called point blanking). Hole-cutting involves removing mesh points that represents the

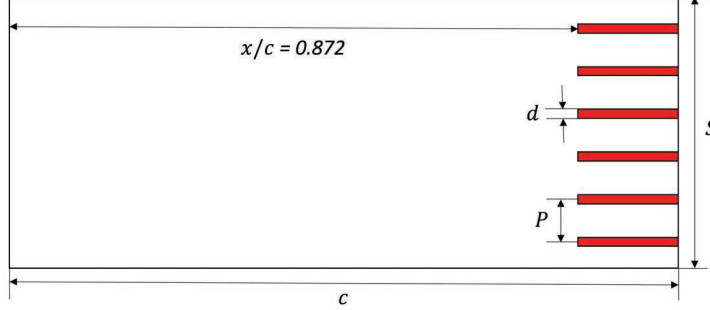


Figure 3.4: Schematic of the fence geometry as modeled: P is the fence pitch, d is fence thickness, c is airfoil chord length, and S is the airfoil span.

interior of a solid body; fences in this case. The PEGASUS software [52] is used to perform hole-cutting. The regions occupied by the fences (defined by specifying ranges $\xi_1 - \xi_2$, $\eta_1 - \eta_2$, and $\zeta_1 - \zeta_2$) are removed (cut out) from the baseline grid and the no-slip adiabatic wall with a zero-normal pressure gradient boundary condition (4th order extrapolation) is applied to the new boundaries thus created.

Figure 3.5 shows cross-sectional views of the meshes for the two different fence heights; the views are zoomed in on the fence region to clearly show the geometry differences. Every other grid point along each axis is shown for clarity. The cross-sectional views are in planes where a fence is present. The grid points in the grey regions between the airfoil surface and the red curves are blanked out (removed) from FDL3DI computation. The red curves indicate the no-slip boundaries created due to hole-cutting. The fences begin at $x/c = 0.872$ (most upstream location) and reach their maximum height (H) at $x/c = 0.971$. Based on prior experiments, Clark [1] recommend that the height of the finlets should be between 25-50% of the boundary layer thickness. In the current simulations, the heights of the two fences are 19% and 43% of the boundary layer thickness at $x/c = 0.971$. Scaled by the displacement thickness of the baseline airfoil, the maximum nondimensional height of the two fences are $H/\delta^* = 1.0$ and 2.26. The location of the most upstream point and the location of the maximum height of the fences are the same as that used in the experiment of Clark *et al.* [4].

Figure 3.6 shows top views of the baseline and the fence meshes (the two fence meshes appear identical in this view as only the fence height is different). Clark [1] stated that the fence thick-

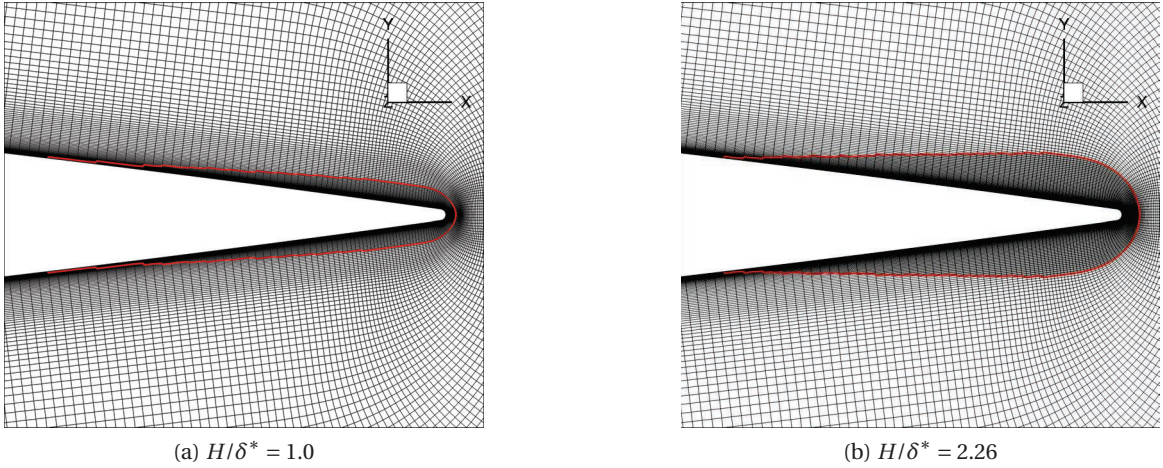


Figure 3.5: Cross-sectional (zoom) views of the computational meshes used to simulate the $H/\delta^* = 1.0$ and $H/\delta^* = 2.26$ stair-step fence geometries. Every other grid point along each axis is shown for clarity.

ness should be as small as possible. The fences are 2-cell thick in the current simulations, which corresponds to a nondimensional thickness $d/\delta^*(= 0.17)$. The effect of the fence spacing is not well understood, but according to Clark [1], an open area percentage of 75% or higher has been shown to yield the best performance. In the current simulations, an open area percentage of 88.5% is used, which similar to the configurations in Clark *et al.* [4] that resulted in farfield noise reduction. Based on this open-area percentage, the scaled pitch (distance between two adjacent fence walls) is $P/\delta^*(= 1.49)$.

The fence meshes were not further refined in the direction normal to the fence walls as the maximum z^+ is approximately 25.2 (located at the maximum fence height), which is not significantly greater than the span-averaged baseline z^+ value near the airfoil surface. Furthermore, we are not interested in accurately resolving the boundary layer on the surfaces of the fences. Our hypothesis is that the noise is reduced due to the displacement of energy-containing turbulence eddies away from the trailing edge, which can be captured even if the fence surfaces are modeled as inviscid walls. By not resolving the boundary layer on the sides of the fence walls, we may not accurately capture some of the near-wall boundary layer flow physics, however, we believe that this level of resolution is not necessary to capture the observed noise reduction.

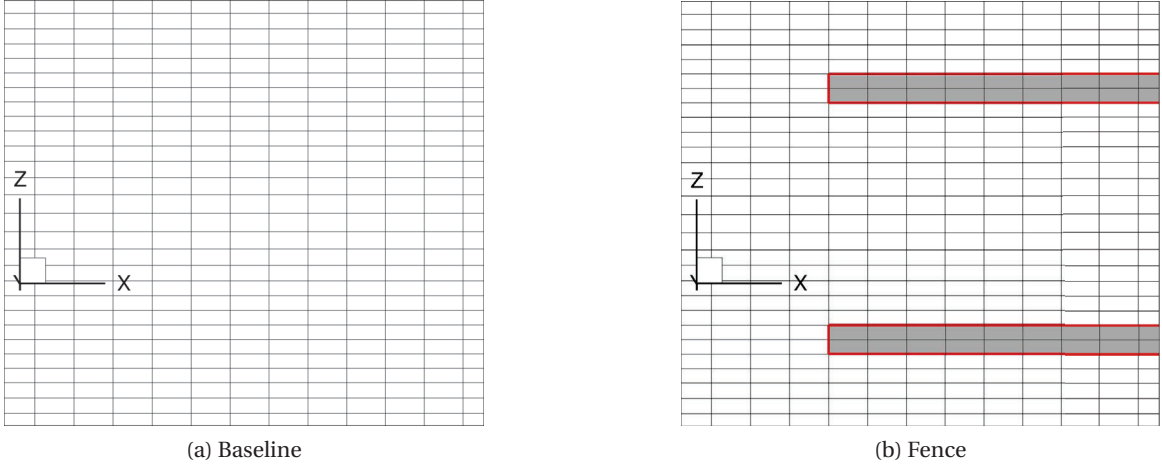


Figure 3.6: Top views of the baseline and fence meshes (the two fence meshes are identical from the top view). Each fence element is modeled to be two-cell thick in the simulations.

A mesh containing a single fence element (one fence pitch wide) is created and then repeated six times along the span to obtain a 3-D mesh with a span of 5.85% chord. It should be emphasized that other than the holes introduced in the fence meshes, the grids for all three cases (baseline and two fences) are identical. This eliminates grid-to-grid differences in the simulation results when comparing the different designs.

3.3.3 Boundary Layer Trip

Since the simulation Re_c ($= 5 \times 10^5$) is much smaller than that of the experiments ($= 2.5 \times 10^6$), the boundary layer on the airfoil surface is forcibly tripped in the simulations. It should be noted that a boundary layer trip (serrated tape) was also used in the experiments [4]. In the simulations, boundary layer tripping is achieved by placing a geometry-resolved “trip wire” at $x/c = 0.05$, measured from the leading edge of the airfoil. The height of the trip wire in wall units is $y^+ \sim 20$. The trip wire successfully forces the boundary layer to transition well upstream of where it would naturally transition at $Re_c = 5 \times 10^5$, thereby achieving a turbulent boundary layer similar to what would occur via natural transition at high Re_c . Details of the tripping methodology are available in Ref. [45] and chapter 2.3.3.

3.3.4 Removal of Transients

Several techniques are employed to reduce the computational cost of the simulations. Each simulation is initiated in 2-D, with a potential flow solution as the initial condition. The Navier-Stokes equations are then solved for the 2-D problem until statistical convergence is achieved; this typically takes about 10τ , where $\tau (= t U_\infty / c)$ is the characteristic flow time. The solution is then replicated in the span direction to obtain an initial 3-D solution for the baseline geometry. Transients in the 3-D simulation are then removed, which takes between $3 - 5\tau$. For the 3-D simulations with fences, the solution is obtained in two steps. First the 2-D solution is replicated over a single-fence span width and simulated with the fences modeled in the computation, and the solution is allowed to reach a statistical stationarity state ($\approx 10\tau$). This solution is then repeated for as many fences as required ($= 6$ here) to fit in the 5.85% span length of the full 3-D geometry simulated. Transients are then removed in the full 3-D simulation (with the array of fences) by simulating the flow for another 5τ .

3.4 Results

This section presents the baseline validation, aerodynamic and aeroacoustic results of the numerical simulations followed by a discussion on noise reduction mechanisms with the fence designs.

3.4.1 Baseline Validation

Once the transients are removed from the 3-D simulations, the simulation data is collected for approximately 2.5τ ($\approx 63,000$ samples) and averaged in time and along the span to compute aerodynamic performance. Figure 3.7 (a) compares the predicted time- and span-averaged aerodynamic pressure coefficient (C_p) distributions of the baseline airfoil with experimental data and with XFOIL [53] predictions. The experimental measurements are from Sagrado *et al.* [8] and Gregory *et al.* [54] for NACA 0012 airfoils at $AOA = 0^\circ$ for $Re_c = 4 \times 10^5$ and $= 2.9 \times 10^6$, respectively. The boundary layer is tripped on both surfaces of the airfoil at $x/c = 0.127$ in Sagrado *et al.* [8] and at $x/c = 0.05$ in Gregory *et al.* [54]. XFOIL results are also obtained with the boundary layer tripped at $x/c = 0.05$ and $Re_c = 5 \times 10^5$, which is the same as in the FDL3DI simulation. The FDL3DI prediction of C_p agrees very well with the measured data over the entire airfoil except for the notch in the FDL3DI result at

the trip wire location. The agreement with the higher Re_c data is better. XFOIL does remarkably well in predicting the C_p distribution.

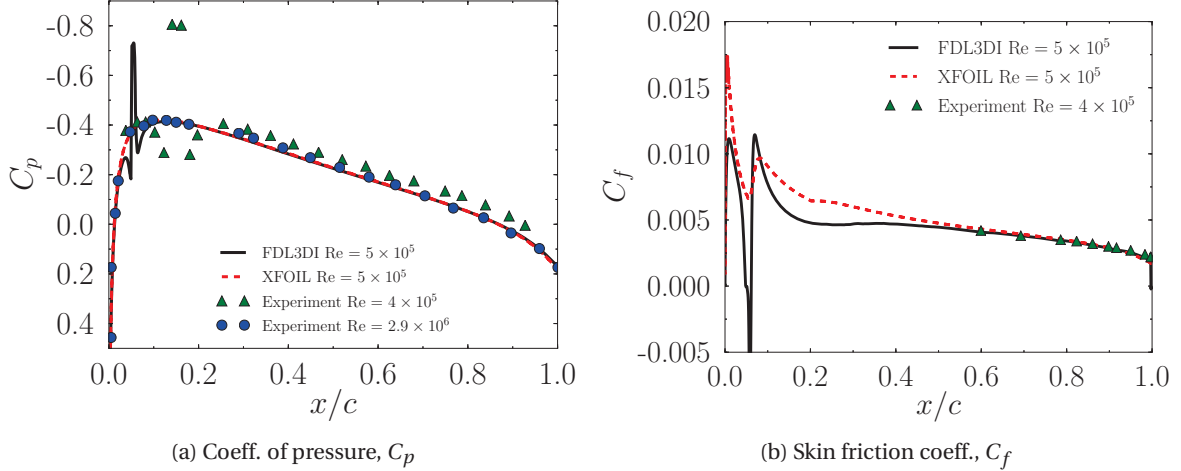


Figure 3.7: Time- and span-averaged C_p and C_f distributions from FDL3DI predictions ($Re_c = 5 \times 10^5$) compared with experiments ($Re_c = 4 \times 10^5$ & $Re_c = 2.9 \times 10^6$) and XFOIL simulations ($Re_c = 5 \times 10^5$).

Figure 3.7 (b) compares the skin friction coefficient (C_f) distribution over the airfoil surface between FDL3DI prediction, XFOIL prediction, and measured data from Sagrado *et al.* [8]. Excellent agreement is seen between the FDL3DI predictions and the measured data. Large differences between XFOIL and FDL3DI are observed near the trip wire location ($x/c = 0.05$) as expected. In FDL3DI, the trip wire triggers an instability wave that induces transition over a finite distance, while in XFOIL the transition appears to occur immediately. Despite this difference, the two predictions agree reasonably well in the aft portion of the airfoil where the boundary layer is turbulent in both the simulations.

Figure 3.8 shows the span-averaged surface pressure spectrum (Φ) for the baseline airfoil at $x/c = 0.98$. The spectrum is normalized by the inner variables as $\Phi(\omega)/(\tau_w^2 \nu / u_\tau^2)$, where τ_w is the wall shear stress, ν is the kinematic viscosity, u_τ is the friction velocity and ω is the angular frequency. The predicted spectra were computed using 1400 samples spanning over 2.5τ of simulation data. The wall pressure spectrum is expected to follow a power-law behavior, $\Phi(\omega) \sim \omega^n$, where the exponent n is dependent on the frequency range of the turbulent spectrum. The ω^{-5} behavior is associated with sources in the boundary layer below y^+ of 20 [62]. Figure 3.8 shows that the predicted turbulent

spectrum follows the expected power-law behavior. Measurements of surface pressure spectra at multiple chordwise locations are available in Figure 13 (b) of Ref. [8] (not reproduced here); the measurements are for a NACA 0012 airfoil at $AOA = 0^\circ$ and $Re = 2 \times 10^5$ and 4×10^5 . There is good agreement between the current LES results and the measurements in terms of the frequency range over which the wall pressure spectra follow the ω^{-5} behavior.

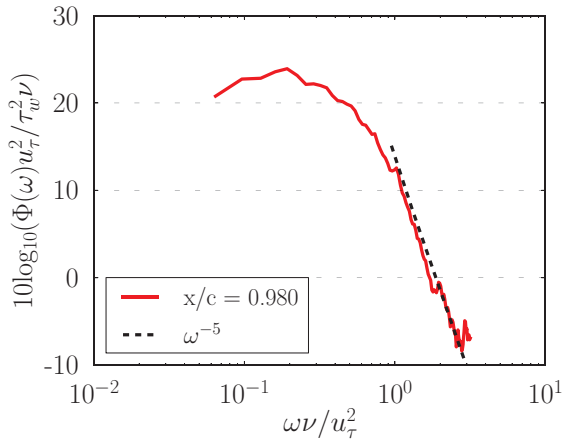


Figure 3.8: Predicted span-averaged surface pressure spectrum for the baseline airfoil at $x/c = 0.980$; the spectrum is normalized by the inner variables.

Figure 4.14 (a) compares the baseline time- and span-averaged normalized velocity (U^+) profiles at different chordwise locations on the aft portion of the airfoil. The profiles follow the expected $U^+ = y^+$ trend in the viscous sublayer. The slope in the log-law region is found to be 1/0.34 in the simulations and in the measurements reported in Ref. [5]. This slope is slightly different than the value of 1/0.41 obtained with the von Kármán constant. Nagib *et al.* [63] found that the von Kármán constant is not universal and is dependent on the flow geometry and pressure gradient. Experiments by Lee and Kang [5] for turbulent flow over a NACA 0012 airfoil at $Re_c = 600,000$ found the slope to be closer to 1/0.34 (see Fig. 4.14 a).

Figure 4.14 (b) compares the current LES predictions of the time- and span-averaged velocity profiles, U/U_∞ for the baseline airfoil with the measurements from Sagrado *et al.*[8]. The agreement is good except very near the airfoil surface where the velocity is slightly lower in the measurements. Similar differences have been observed in other LES predictions (see e.g., Wolf and Lele [64]).

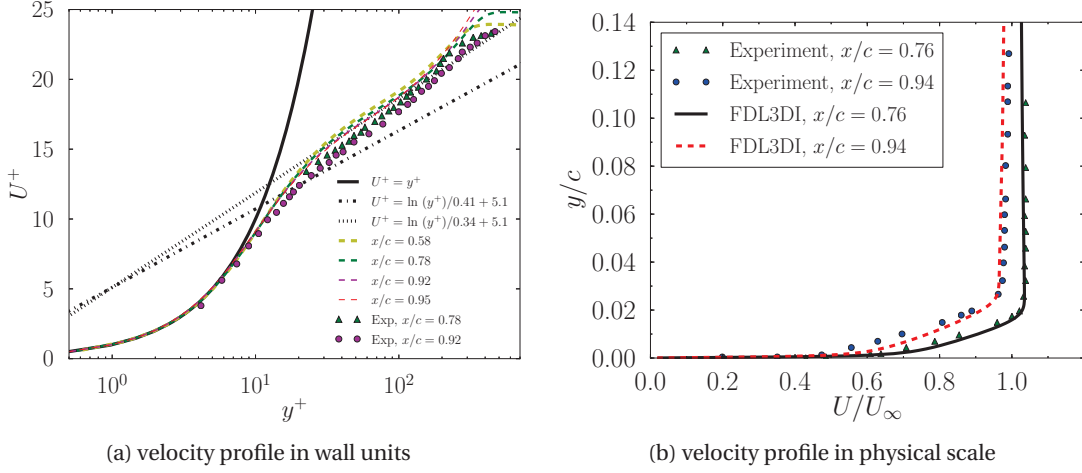


Figure 3.9: Baseline time- and span-averaged velocity profile comparisons of the current LES predictions and experiment from a) Lee and Kang [5] and b) Sagrado *et al.* [8].

Figures 3.10 and 3.11 compare the predicted time- and span-averaged velocity and turbulence intensity profiles at two locations in the airfoil wake with measurements from Sagrado *et al.* [8]. The agreement is generally good except the peak wake deficit at $y/c = 0.0$ is slightly underpredicted. Correspondingly, the turbulence intensity at that location is slightly over predicted in the LES results. As with the velocity profiles, similar differences were observed in the LES predictions by Wolf and Lele [64].

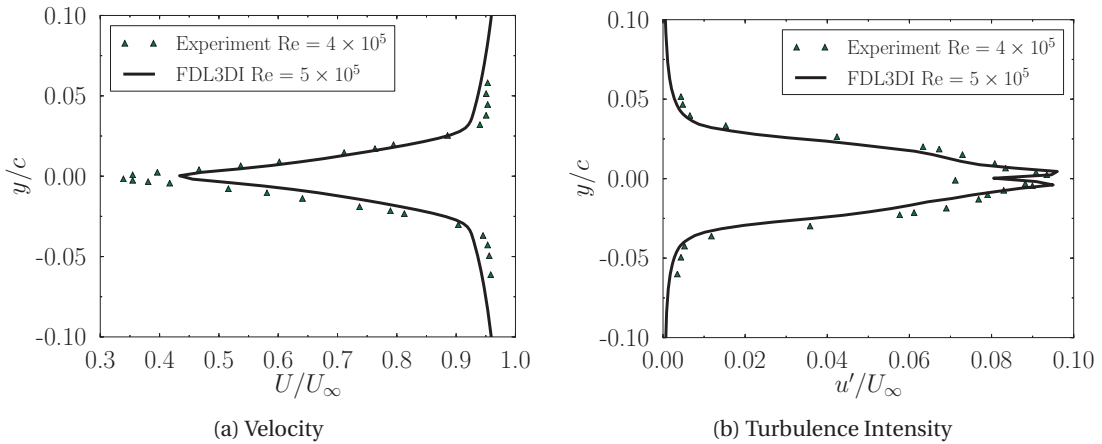


Figure 3.10: Baseline time- and span-averaged velocity and turbulence intensity comparisons of the simulation and experiment from Sagrado *et al.* [8] at $x/c = 1.02$.

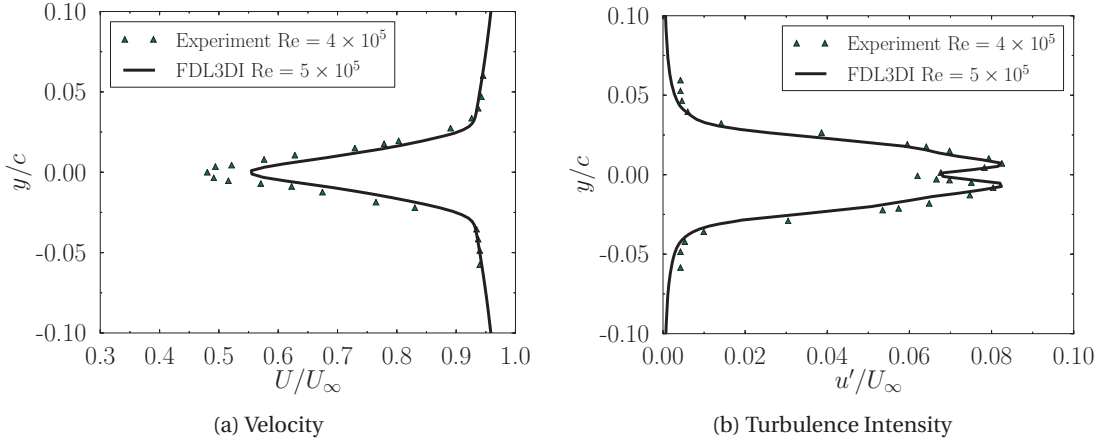


Figure 3.11: Baseline time- and span-averaged velocity and turbulence intensity comparisons of the simulation and experiment from Sagrado *et al.* [8] at $x/c = 1.05$.

3.4.2 Aerodynamic Performance

Figure 3.12 compares the time- and span-averaged C_p and C_f distributions over the airfoil surface between the baseline and the two fence geometries. In this and other plots that show span-averaged results, unless specified otherwise, the points that lie on and within the fence walls are removed in the averaging procedure for the fence simulations. Outside of the fence region, the C_p and C_f distributions are nearly identical for the three simulations. For the fences, both C_p and C_f drop below the corresponding baseline values in the fence region.

Figure 3.13 shows the time- and span-averaged wall-normal velocity in the fence region at $x/c = 0.975$. From the airfoil surface to the top of the fences (shown by horizontal dashed lines), there is a lower velocity gradient with the fences than with the baseline. Above the fence height, the velocity abruptly changes for both fences while the velocity gradient of the baseline remains smooth. This sudden inflection in velocity profile is typical of canopy flows [36]. The reduced gradient near the wall is responsible for the reduced wall skin friction seen earlier in Fig. 3.12 (b).

Since the fences maintain the flow symmetry for the $\text{AOA}=0^\circ$ case investigated, the mean lift ($= 0$) is unaffected by the fences. The drag coefficient ($C_D = D/(q_\infty S.c)$) of the baseline and fence geometries is compared in Table 3.2. Here $q_\infty = \frac{1}{2}\rho_\infty u_\infty^2$, S is airfoil span, and c is airfoil chord. Note that the surface area ($= S \times c$) used to compute C_D is unchanged between baseline and fences.

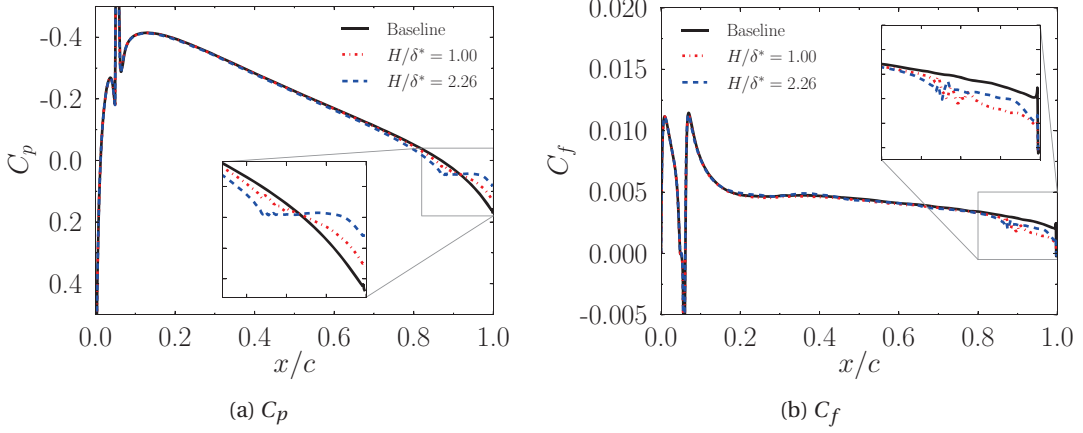


Figure 3.12: Time- and span-averaged C_p and C_f distributions compared between the baseline and the two fence simulations.

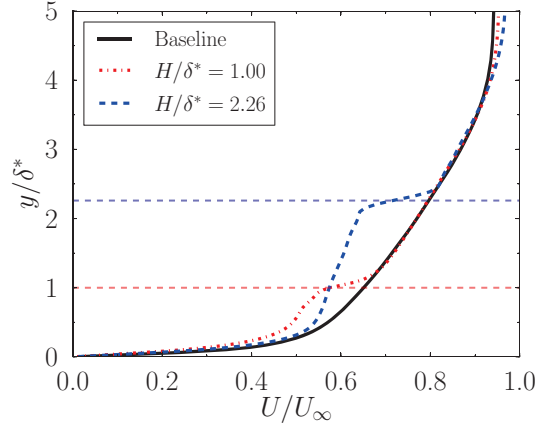


Figure 3.13: Predicted wall-normal velocity profiles at $x/c = 0.975$. The profiles are averaged over the span. The horizontal dashed lines represent the top of the fences.

In the first three rows of Table 3.2, C_D is computed by integrating the x component of the forces acting on the airfoil surface and the side-, front-, and top walls of the fences. The drag for both fences is larger than the baseline although the percentage increase is small, particularly with the smaller fence. Note that the increase in C_D is substantially smaller than the increase in the wetted surface area (additional surface area due to the fence side and front walls). To further analyze this, C_D is also computed by *ignoring* the contribution from the side and front walls of the fences; the contribution from the top wall is still included. These values are listed in the last two rows of Table 3.2. When computed this way, the C_D is slightly lower for the fences compared to the baseline due to the reduc-

tion in C_f within the fence channels (see Fig. 3.12 (b)). Furthermore, there is virtually no difference in C_D between the two fence heights.

The net aerodynamic effect of the fences is an increase in drag with the percentage increase equal to 3.36 and 13.2 respectively for the short and tall fences

Table 3.2: Drag coefficient (C_D) comparisons between the baseline and fence simulations

Geometry	C_D	C_D %increase	Wetted area %increase
Baseline	0.01212	–	–
$H/\delta^* = 1.0$	0.01253	3.36	9.47
$H/\delta^* = 2.26$	0.01372	13.2	22.1
$H/\delta^* = 1.0$ (neglecting lateral/front fence sides)	0.01202	-0.81	0.0
$H/\delta^* = 2.26$ (neglecting lateral/front fence sides)	0.01201	-0.90	0.0

3.4.3 Aeroacoustic Performance

The in-house Ffowcs Williams-Hawkins (FW-H) solver described in Sec. 3.2.2 is used to calculate the far field noise. A porous integration (Kirchoff) surface is used that is approximately half chord away from the airfoil surface. Data is sampled for approximately four characteristic times (4τ) for a total of 1200 samples. The data is segmented into 13 intervals for spectral averaging using Welch's method [55].

Figure 3.15 plots the predicted far field noise spectra for the baseline and the two fences at the azimuth angle, $\theta = 90^\circ$. The azimuth angle is measured from downstream, and is positive in the counter-clockwise direction (see Fig. 3.14). The origin of the coordinate system is at the airfoil trailing edge ($x = c$, $y = 0$). The observer location is at $x = c$, $y = 12c$ and mid-span. The dimensional frequencies in Fig. 3.15, and in the remainder of the text are obtained by scaling the nondimensional simulation results to the experimental conditions. The reference length and velocity scales in the experiment [4] are: airfoil chord length of 0.8 m and free stream velocity of 50 m/s.

As seen in Fig. 3.15, a large reduction in the farfield SPL is observed with both fences for frequencies (f) greater than 1.5 kHz. Between 600 Hz – 1.5 kHz, noise reduction is observed only with the shorter fence. In contrast, for $f > 2$ kHz, the taller fence is quieter than the shorter fence. Figure 3.16 plots the measured [4] farfield spectra for a different baseline airfoil (DU96-W-180) and two fence geometries, and is shown here for a qualitative comparison with the prediction results plotted

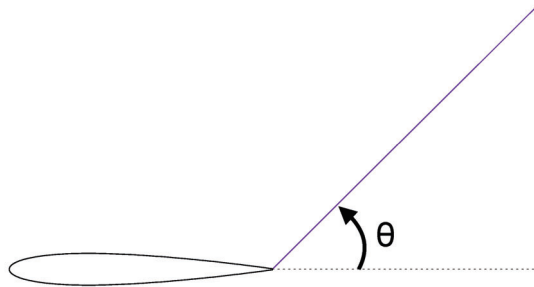


Figure 3.14: Azimuthal angle, θ measured from downstream. The origin of the coordinate system is at the airfoil trailing edge.

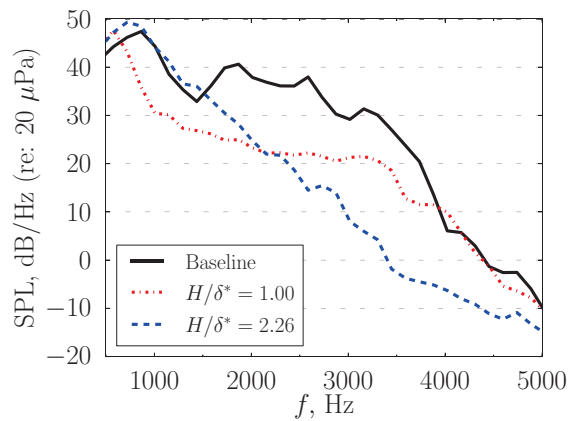


Figure 3.15: Predicted farfield noise spectra at an observer located at $\theta = 90^\circ$.

in Fig. 3.15. The measured farfield noise was obtained using acoustic beamforming over a two-dimensional area near the trailing edge. The data in Fig. 3.16 is for the -0.5° angle-of-attack case for the DU96-W-180 airfoil. In the experiment [4], the maximum heights of the two fences were 4 and 8 mm. An estimate of δ^* for the DU96-W-180 for this case is obtained using XFOIL, and the scaled maximum heights of the two fences, H/δ^* are found to be 0.62 and 1.38 on the suction side and 0.98 and 1.96 on the pressure side. The estimates from XFOIL were obtained by forcing the flow to transition at the same location that the trip wire was placed in the experiment, which was at $x/c = 0.05$ and $x/c = 0.10$ on the suction and pressure surface, respectively. Note that the value of the displacement thickness slightly varies depending on the location of the trip.

Kato's correction [56] is used to account for the difference in the simulated span and the span over which the measured data is integrated during Beamforming in the measurement of farfield

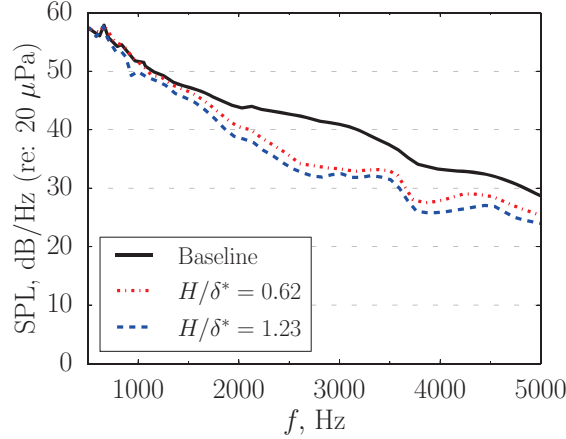


Figure 3.16: Measured farfield sound spectra from Clark *et al.* [4]. The nondimensional fence pitch, $P/\delta^* = 0.69$ in the experiment.

sound. The general trend of larger noise reduction (for $f > 2$ kHz) with taller fences is the same as the experimental observation even though the reduction is much greater in the simulations. For $f < 2$ kHz, the simulations predict the taller fence to be louder than the shorter fence but the experiments found the taller fence to be quieter over the entire spectrum. The experiment data shows no measurable difference between the baseline and the two fence geometries at these low frequencies. Clark *et al.* [4] noted that the measurements may be limited by the facility noise for $f < 1$ kHz; hence any potential noise reduction at those frequencies is not captured by the measurements.

The following differences between the experiment and the simulations can explain the differences in the predicted and measured trends: (1) The baseline airfoils are different; the simulations are for a symmetric (NACA 0012) airfoil while the measurements use the asymmetric DU96-W-180 airfoil, (2) the scaled fence heights, H/δ^* are substantially different; while the taller fence in the simulations has $H/\delta^* = 2.26$, the taller fence in the experiment has $H/\delta^* = 1.23$, and (3) the scaled pitch of the fences, P/δ^* in the simulations is 1.49, which is approximately double of that in the experiment ($= 0.69$).

Figure 3.17 shows the predicted farfield noise spectra at two observer locations at azimuth angles of $\theta = 45^\circ$ and 135° . The trends for the noise reduction are the same as with $\theta = 90^\circ$, i.e., noise reduction is observed with only the shorter fence for $f < 1.5$ kHz but with both fences for $f > 1.5$ kHz, where a greater noise reduction is observed with the taller fence for $f > 2$ kHz. Although the

trend of noise reduction is similar to $\theta = 90^\circ$, the *SPL* difference between the fences and the noise reduction compared to the baseline are smaller, especially at $f > 2$ kHz.

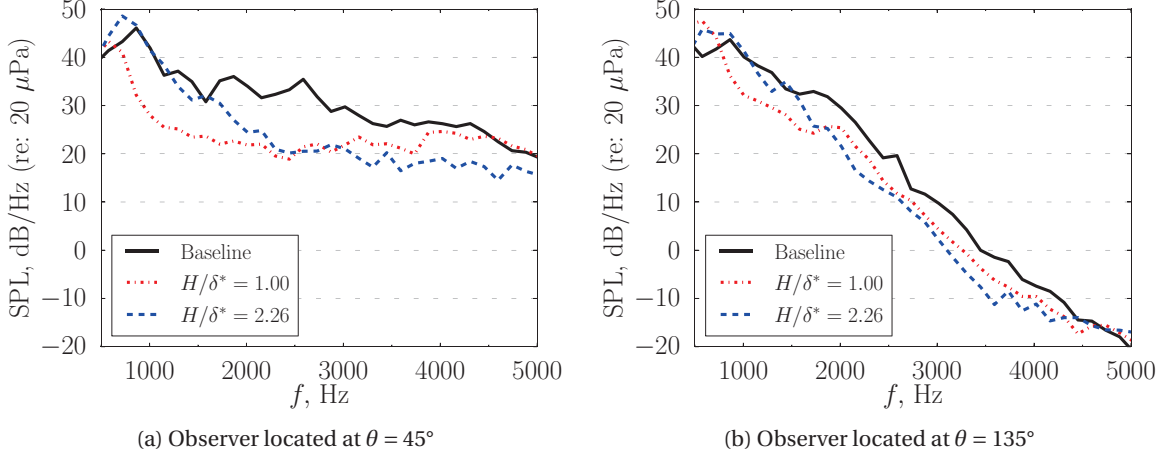


Figure 3.17: Predicted farfield noise spectra at observer locations: a) $\theta = 45^\circ$ and b) $\theta = 135^\circ$.

To quantify the overall noise reductions, band sound pressure level (L_{pb}), defined as

$$L_{pb} = 10 \log_{10} \sum_{f_{\min}}^{f_{\max}} \left(|\hat{p}(f_i)| / p_{\text{ref}} \right)^2, \quad (3.5)$$

is computed, where $p_{\text{ref}} = 20 \mu\text{Pa}$, and f_{\min} and f_{\max} correspond to the minimum and maximum frequencies of the band level over which the spectra is integrated. We integrate over different frequency ranges to quantify the variation of noise reduction with frequency.

The difference in computed band pressure level, ΔL_{pb} between the baseline and the two fence geometries for azimuth angle $\theta = 90^\circ$ are listed in Table 3.3. As seen in the first column, integrating over the entire frequency range results in a L_{pb} reduction of 5.43 dB with the short fence ($H/\delta^* = 1.0$). However, with the taller fence ($H/\delta^* = 2.26$), the L_{pb} increases slightly (≈ 0.54 dB). The second column, which is obtained by integrating over the low frequencies (500 Hz–2 kHz), shows a L_{pb} reduction of 4.86 dB with the shorter fence and an increase of 1.2 dB with the taller fence. Integrating over only the high frequencies (2–5 kHz), as shown in the third column, a significant reduction in L_{pb} is seen with both fences, where a larger reduction is observed with the taller fence. The results of the integrated band pressure level for azimuth angles $\theta = 45^\circ$ and 135° are shown in Tables 3.4 and 3.5. The trends for noise reduction are the same as with $\theta = 90^\circ$, except with smaller noise reductions in the 2–5 kHz frequency range.

Table 3.3: Difference in L_{pb} between baseline and fences at $\theta = 90^\circ$

Geometry, H/δ^*	ΔL_{pb} , dB 500 Hz – 5 kHz	ΔL_{pb} , dB 500 Hz – 2 kHz	ΔL_{pb} , dB 2 kHz – 5 kHz
1.0	-5.43	-4.86	-12.89
2.26	0.54	1.20	-16.74

Table 3.4: Difference in L_{pb} between baseline and fences at $\theta = 45^\circ$

Geometry, H/δ^*	ΔL_{pb} , dB 500 Hz – 5 kHz	ΔL_{pb} , dB 500 Hz – 2 kHz	ΔL_{pb} , dB 2 kHz – 5 kHz
1.0	-6.08	-5.93	-7.09
2.26	1.14	1.77	-9.54

To estimate the reduction in radiated sound power, the L_{pb} is integrated over all azimuth angles and the results are listed in Table 3.6. The trends for the noise reduction are the same as seen in Tables 3.3–3.5, which shows that the total sound power generated is reduced at the source.

3.4.4 Noise Reduction Mechanisms

Two hypotheses are put forth to explain the observed farfield noise reduction with the finlet fences:

1. The fences lift the turbulence eddies away from the scattering (airfoil trailing) edge, and
2. the fences reduce the spanwise correlation length.

These hypotheses are investigated using the simulation results in this section.

Turbulence Kinetic Energy

To assess the first hypothesis, the normalized turbulence kinetic energy (TKE) is obtained by averaging the time-accurate flow data over 2.6τ ; the TKE field did not change significantly with dou-

Table 3.5: Difference in L_{pb} between baseline and fences at $\theta = 135^\circ$

Geometry, H/δ^*	ΔL_{pb} , dB 500 Hz – 5 kHz	ΔL_{pb} , dB 500 Hz – 2 kHz	ΔL_{pb} , dB 2 kHz – 5 kHz
1.0	-0.59	-0.54	-4.57
2.26	1.54	1.61	-8.42

Table 3.6: Difference in L_{pb} between baseline and fences after integrating over all azimuth angles.

Geometry, H/δ^*	ΔL_{pb} , dB	ΔL_{pb} , dB	ΔL_{pb} , dB
	500 Hz – 5 kHz	500 Hz – 2 kHz	2 kHz – 5 kHz
1.0	-3.62	-3.21	-8.77
2.26	1.09	1.63	-11.14

bling the sampling duration. Contour plots of normalized TKE at $x/c = 0.975$ are compared between the baseline and fence simulations in Fig 3.18. This is the chordwise location where the fences reach the maximum height. It is clear from the figure that for both fences, the TKE reduces near the airfoil surface and increases above the fences.

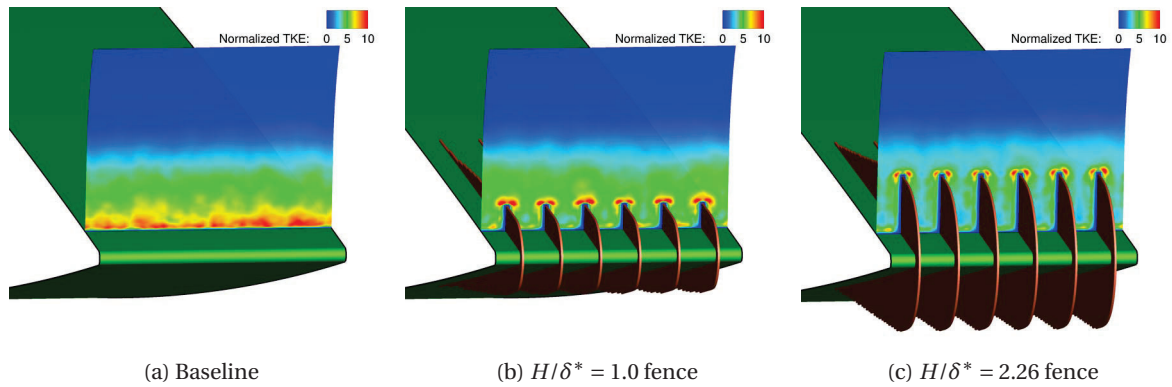


Figure 3.18: Normalized turbulent kinetic energy, TKE/u_t^2 at $x/c = 0.975$ for a) baseline, b) $H/\delta^* = 1.0$ fence, and c) $H/\delta^* = 2.26$ fence

The time-averaged data is further averaged along the span and the span-averaged profiles are compared in Fig. 3.19. In the figure, the vertical axis is the wall-normal distance normalized by δ^* , and the horizontal dashed lines represent the location of the top of the fences. The profiles show a significant reduction in TKE near the airfoil surface due to the fences; furthermore, the reduction is greater with the taller fence. The location of peak TKE is symptomatic of the location of the noise source (the fluctuations in the turbulence). Note that direct radiation from this source is not as efficient as indirect radiation due to scattering of the hydrodynamic field of this source by the airfoil trailing edge. Figure 3.19 therefore verifies the first hypothesis: fence finlets indeed increase the separation distance between the source and the airfoil trailing (scattering) edge.

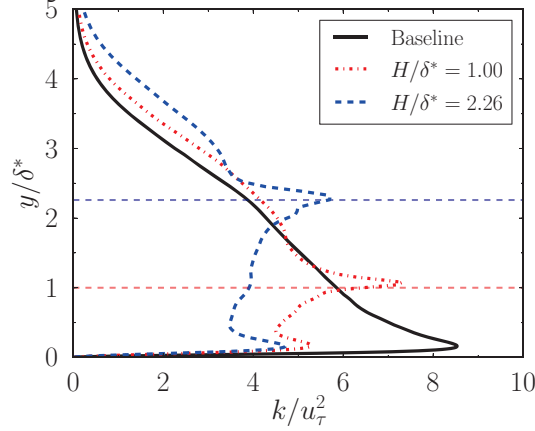


Figure 3.19: Predicted normalized turbulent kinetic energy, TKE/u_τ^2 profiles at $x/c = 0.975$. The profiles are averaged over the span. The horizontal dashed lines represent the location of the top of the fences.

The increased source separation from the airfoil trailing edge leads to inefficient scattering (noise radiation), which is explained below. Ffowcs Williams and Hall [65] studied how turbulent eddies scatter from the edge of a half plane. Edge scattering is most intense when an eddy is well within an acoustic wavelength of the edge, i.e., $2kr_o \ll 1$, where k is the acoustic wave number, and r_o is the distance from the center of the eddy to the edge. When this condition is met, the intensity of the scattered sound, $I \propto \alpha^2/r_o^3$, where α is the normalized turbulence intensity. [65] When the eddies are far enough from the edge ($\sqrt{kr_o} \gg 1$), then the eddies radiate as if in free space and the edge does not produce any significant sound amplification. Therefore, as the turbulence intensity reduces or the peak turbulence shifts away from the edge, the intensity of the sound emitted from the edge should decrease.

The predicted TKE profiles are examined against measured turbulence intensity (TI) profiles reported in Afshari *et al.* [9]. A different experiment is selected for this comparison as Clark *et al.* [4] did not report velocity measurements. Afshari *et al.* [9] investigated the effect of finlets installed in the turbulent boundary layer over a flat plate. Figure 3.20 plots profiles of rms of the fluctuating streamwise flow velocity, u_{rms} normalized by the freestream velocity, U_∞ . In terms of the baseline δ^* at $x/c = 0.975$, the fences in the experiment had maximum heights $H/\delta^* = 0.98$ and 1.46 , and pitch $P/\delta^* = 0.30$. It should be noted that these velocity measurements were taken downstream of the fences instead of between the fences as is done in the current predictions; the fences in the

experiment were placed at $x/c = 0.64$ to $x/c = 0.82$ and velocity measurements taken at $x/c = 0.975$.

Despite these differences, the trend in the current predictions (see Fig. 3.19) is consistent with the measurements, i.e., the turbulent fluctuations (represented by u_{rms} and TKE) decrease near the flat plate/airfoil surface and increase above the fences. Also, in both the experiment and simulation, increasing the fence height results in lesser turbulent fluctuations near the surface.

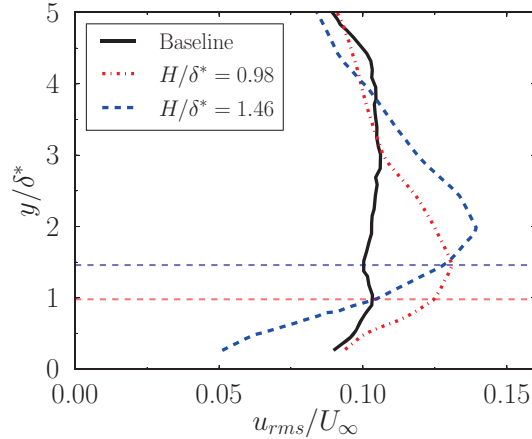


Figure 3.20: Measured profiles of u_{rms}/U_∞ from the flat plate experiment by Afshari *et al.* [9]. The profiles are measured downstream of the fences. The horizontal dashed lines represent the maximum height of the fences.

Surface Pressure Spectra

The primary noise generation mechanism for low Mach number flow over an airfoil is trailing edge noise. The hydrodynamic energy in the boundary layer turbulence results in unsteady surface pressure, primarily near the edge, which radiates as an unsteady lift (dipole) source. Unsteady surface pressure near the trailing edge is therefore a measure of the strength of the noise source. Surface pressure spectra are computed at $x/c = 0.975$. Numerical data is collected for approximately 6τ . Welch's method [55] is used with 1655 samples divided into 20 segments to reduce the scatter in the spectra by spectral averaging. The spectra are further averaged along the span to obtain an overall measure of reduction in spectral magnitude with the fences. The grid planes ($\zeta = \text{constant}$) that have grid points inside the fence region, which are not solved by FDL3DI, are removed in the averaging procedure.

Figure 3.21 (a) compares the predicted surface pressure spectra from the baseline and the two fence simulations. Compared to the baseline, a measurable reduction at high frequencies ($f > 2$ kHz) and a small increase at low frequencies is observed in the predicted spectra for the $H/\delta^* = 1.0$ fence geometry. The taller fence exhibits a similar trend except a greater reduction in the surface pressure spectra is observed at all frequencies. The crossover frequency, at which the surface pressure spectra switches from being higher than baseline to lower than the baseline, is smaller with the larger fence.

These observations are compared with the measured surface pressure spectra from Clark [1] in Fig. 3.21. In the experiment [1], unsteady surface pressure data was only measured with the baseline airfoil and the $H/\delta^* = 1.38$ fence. The predictions agree qualitatively with the measurements with reduction in spectral magnitude observed at high frequencies and an increase at low frequencies. However, the crossover frequency is lower in the measurements.

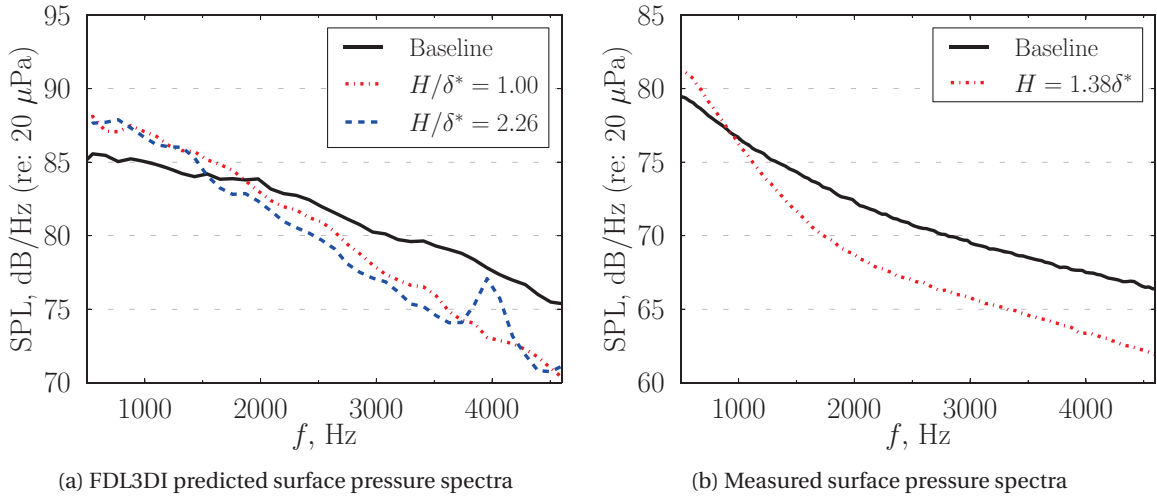


Figure 3.21: Qualitative comparison between the predicted and measured surface pressure spectra near the airfoil trailing edge ($x/c = 0.975$). Measured data is from Clark [1] with a scaled fence pitch $P/\delta^* = 0.77$.

A broad peak is observed around 4 kHz in the predicted spectrum for the taller fence. Spectra were obtained at various chordwise locations and it was found that the peak is maximum at x/c where the maximum fence height occurs. Resonance in the channels between adjacent fences (cascade resonance) could explain the presence of this peak.

Afshari *et al.* [9] assessed the effect of fence height on unsteady surface pressure for two fence spacings ($P/\delta^* = 0.30$ and 1.03) in their flat-plate experiment. The measured spectra are plotted in Fig. 3.22. The measurements show the same trends as in the predictions (compare with Fig. 3.21): 1) increasing the fence height results in further reductions in the unsteady surface pressure at the trailing edge; reductions are limited to high frequencies, and 2) the crossover frequency reduces with increasing fence height.

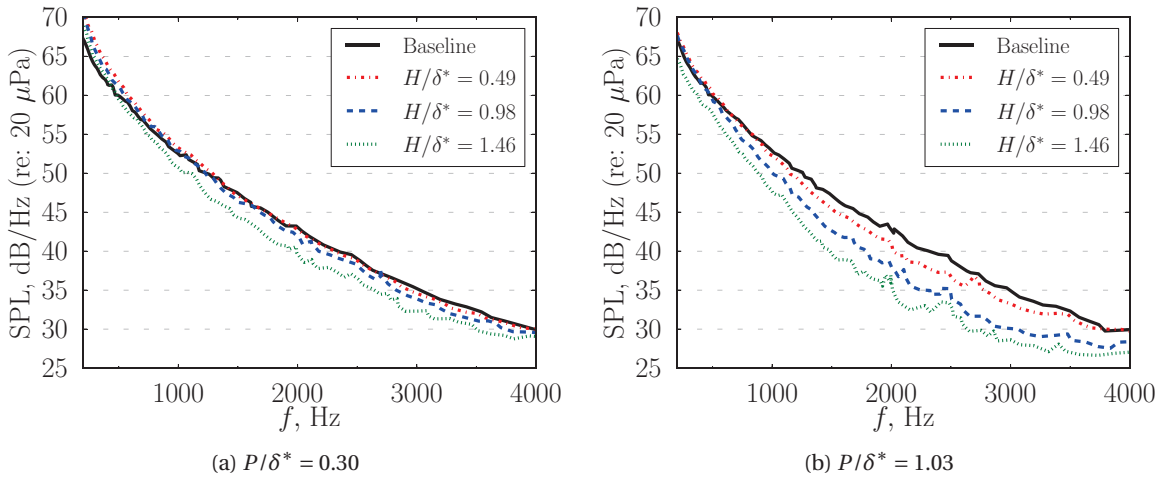


Figure 3.22: Measured surface pressure spectra from Afshari *et al.* [9]. The profiles are measured downstream of the fences. Measurements are for a nondimensional fence pitch, P/δ^* = a) 0.30 and b) 1.03 .

Velocity Spectra

The span-averaged velocity power spectral density (PSD) of the vertical and horizontal velocity fluctuations in the viscous sublayer ($y/\delta^* = 0.045$) at $x/c = 0.975$ are shown in Fig. 3.23. There is a reduction observed in the vertical velocity fluctuations with both fences compared to the baseline particularly at high frequencies. Greater reduction is observed with the taller fence. The same trend is observed in the horizontal velocity fluctuations. Afshari *et al.* [9] reported the velocity PSD measured at $x/c = 0.975$ for fence heights, $H/\delta^* = 0.49, 0.98$, and 1.46 with a fixed pitch, $P/\delta^* = 0.30$. The contour plots near the flat plate surface (see Ref. [9]) showed the same behavior as is seen in the current predictions, i.e., greater reductions are observed with the taller fences and at high frequencies.

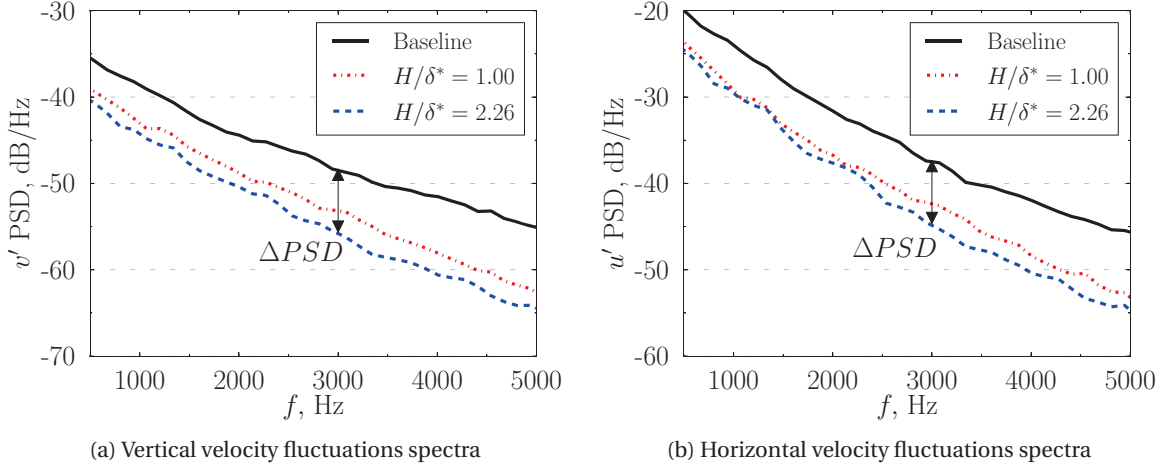


Figure 3.23: FDL3DI predicted velocity fluctuation spectra in the a) vertical and b) horizontal directions within the viscous sublayer ($y/\delta^* = 0.045$) at the trailing edge $x/c = 0.975$. Predictions are averaged along the span with the points within the fences removed from the averaging procedure.

Review of the First Hypothesis

The observations are summarized here. For $f > 2$ kHz, the farfield noise reduces with both fences, with higher reductions observed for the taller fence. Commensurate with the farfield noise reductions, the near-surface velocity fluctuations and the unsteady surface pressure reduce with the fences for $f > 2$ kHz, and larger reductions are seen with the taller fence. In addition, it is shown that with the fences, the TKE reduces near the surface and increases above the fences; higher TKE reduction is observed with the taller fence. These results substantiate the first hypothesis to explain the measured farfield noise reductions: the fences lift the turbulence eddies away from the scattering (trailing) edge thereby increasing the distance between the noise source (turbulence) and the airfoil trailing edge. Because of the increased source-scattering edge separation distance, the high frequency ($f > 2$ kHz) surface pressure fluctuations reduce, which reduces the scattering efficiency of the trailing edge, leading to farfield noise reduction. Increasing the fence height increases the source-scattering edge separation distance which further reduces the unsteady surface pressure and the farfield sound.

Spanwise Coherence

Next we study spanwise coherence to investigate the second hypothesis. Dependence of farfield noise on spanwise coherence can be assessed using Amiet's theory [40] which gives an analytical expression of the farfield pressure PSD, $S_{pp}(\omega)$ of sound radiated from a turbulent flow past the trailing edge of a half-plane. Per Amiet [40], $S_{pp}(\omega) \propto l_y(\omega) S_{qq}(\omega)$, where ω is the angular frequency, $l_y(\omega)$ is the spanwise correlation length of the pressure fluctuations, and $S_{qq}(\omega)$ is the surface pressure PSD. A reduction in spanwise coherence (a measure of $l_y(\omega)$) can cause farfield noise reduction even if the surface pressure PSD remains unchanged.

Coherence squared (γ^2) between two points \mathbf{x} and \mathbf{y} is defined as

$$\gamma_{xy}^2(\omega) = \frac{|S_{xy}(\omega)|^2}{S_{xx}(\omega)S_{yy}(\omega)}, \quad (3.6)$$

where $S_{xx}(\omega)$ is the power spectral density (PSD) evaluated at \mathbf{x} and $S_{yy}(\omega)$ is the PSD at \mathbf{y} . For spanwise coherence, points \mathbf{x} and \mathbf{y} are at a given chordwise location (x/c) but separated in the span direction such that $\mathbf{y} = \mathbf{x} + \Delta z \hat{e}_k$, where \hat{e}_k is a unit vector along the span direction. The reference location to compute spanwise coherence is varied along the span. Each grid point is selected as a reference to compute one instance of coherence. All the instances of coherence so computed (101 in total) are then averaged to obtain the γ^2 reported here.

Equation 4.6 is used with the aforementioned span averaging to compute $\gamma_{xy}^2(\omega)$ for the baseline and fence simulations. A total of 6τ of data, consisting of 1655 samples divided into 20 segments for spectral averaging is used for the calculations. Figure 3.24 compares γ^2 of the unsteady surface pressure near the trailing edge ($x/c = 0.975$) as a function of the spanwise separation distance ($\Delta z/c$) for the baseline and fence simulations. Coherence plots are drawn for two example frequencies to highlight the characteristics in the low- and high-frequency regions. The vertical dashed lines in the plots represent the spanwise location of the fences. The fences are equidistant and the pitch is P .

Focusing on γ^2 for separation distances greater than the fence pitch, i.e., $\Delta z/c > P/c$, we note that the fences reduce γ^2 at low frequencies; a larger reduction in γ^2 is obtained with the taller fence. At high frequencies, the coherence is already small for $\Delta z/c > P/c$ and the fences do not reduce it any further. The simulation results show a farfield noise reduction at low frequencies (see Fig. 3.15) with the $H/\delta^* = 1.0$ fence despite an increase in the unsteady surface pressure PSD (see Fig. 3.21 (a)).

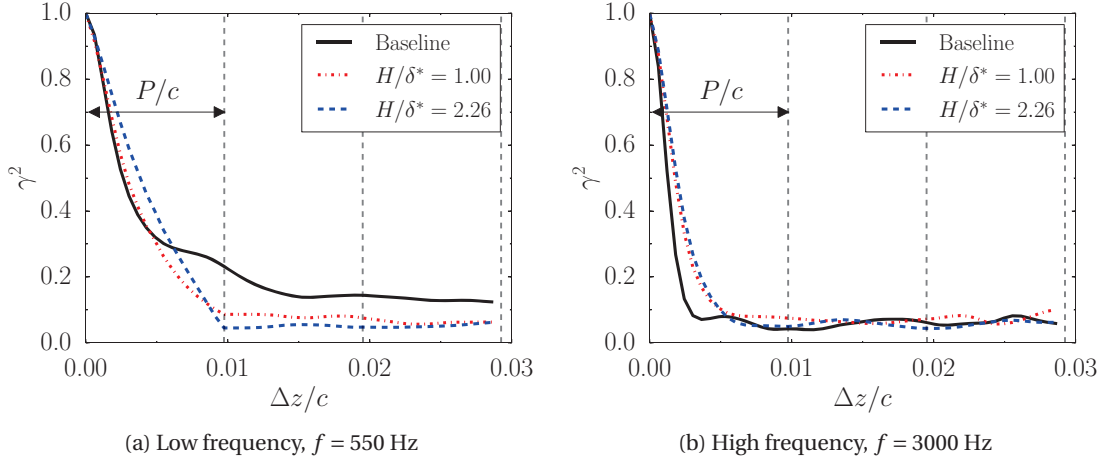


Figure 3.24: Spanwise coherence, $\gamma^2(\omega)$ of unsteady surface pressure at the trailing edge $x/c = 0.975$ for a) low, and b) high frequencies.

This analysis suggests that the reduction in spanwise coherence at low frequencies is responsible for the reduction in farfield noise.

This argument is supported by the following observation of the results from Clark [4]. Low-frequency noise reduction is observed when the fence pitch is reduced (see Fig. 3.25). Since fences successfully reduce γ^2 for spanwise distances greater than a fence pitch, a tighter pitch implies a reduction in span correlation length, and hence farfield noise.

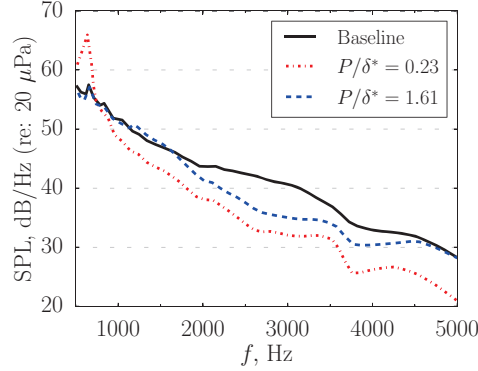


Figure 3.25: Measured farfield noise spectra from Clark *et al.* [4] showing the effect of fence spacing. For all cases, the normalized maximum height of the fences, $H/\delta^* = 0.62$ on the suction side.

For a separation distance smaller than the fence pitch, i.e., $\Delta z/c < P/c$, γ^2 increases due to the fences. This is observed for both fences at high frequencies, but only for the taller fence at low fre-

quencies. Adjacent fences act as channel walls bounding the flow, thereby increasing the coherence within each channel/passage. The taller fences create a stronger “channeling” effect and it correspondingly has a greater increase in γ^2 . At high frequencies (small wavelength), the increase in source-trailing edge separation dominates over the increase in γ^2 and farfield noise reduction is observed with fences. At low frequencies the increase in source separation distance is small (corresponding to the acoustic wavelength) with the fences and hence the spanwise coherence becomes a dominant factor. This increase in γ^2 within fence passages would therefore imply an increase in the radiated farfield sound with the taller fence in comparison to the smaller fence, which is indeed observed in the numerical predictions (see Fig. 3.15).

Another potential reason for the taller fence to be louder than the shorter fence at low frequencies, even though the taller fence has lower pressure PSD on the airfoil surface (see Fig. 3.21), is the additional noise due to scattering from the leading edge of the fence. As the maximum fence height increases, the leading edge of the fence becomes less aligned with the flow (see Fig. 3.26), increasing the energy in the wavenumber component (of the boundary layer turbulence) normal to the fence edge. This results in an unsteady force on the fence leading edge which radiates noise as a dipole source. The noise generation mechanism is the same as for the leading edge noise problem investigated in Amiet [66].

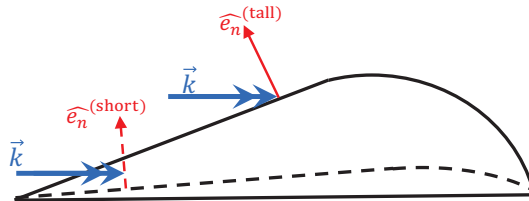


Figure 3.26: A schematic illustrating the effect of increasing the maximum fence height on the angle between the oncoming boundary layer turbulence wavenumber vector (\vec{k}) and the fence normal (\hat{e}_n). Highest sound radiation from the fence edge would occur when \vec{k} and \hat{e}_n are parallel.

3.5 Conclusions

This paper presents numerical investigations of airfoil geometries inspired by the down coat of the owl. The down coat is modeled using finlet fences proposed by Clark *et al.* [3]. Large eddy simu-

lations are performed for the zero-lift case ($\text{AOA}=0$ degree) for the baseline (NACA 0012) airfoil and two airfoils with fences attached to the aft portion of the airfoil. Two fences with different maximum nondimensional heights, $H/\delta^* = 1.0$ and 2.26 , are investigated.

The aerodynamic analysis shows that the drag increase due to the fences is small and is due to the increased wetted surface area. The skin friction coefficient on the airfoil surface reduces because of fences and hence the drag increase is smaller than the increase in the wetted surface area.

An in-house FW-H solver is used with the LES data to predict the farfield noise and evaluate the aeroacoustic performance of the fences. Compared to the baseline, the $H/\delta^* = 1.0$ fence reduces the farfield SPL by up to 10 dB for frequencies between 500 Hz and 5 kHz. Noise reduction with the taller fence ($H/\delta^* = 2.26$) is limited to frequencies above 1.5 kHz. Larger noise reduction is observed with the taller fence for frequencies greater than 2 kHz.

Two noise reduction mechanisms are identified: 1) the fences increase the source-scattering edge separation distance rendering the scattering process inefficient, particularly for high-frequency noise, and 2) the fences reduce the spanwise coherence (γ^2) in the boundary layer for separation distances greater than the fence pitch, which is more effective at reducing low-frequency farfield noise.

The first mechanism of noise reduction is verified by examining the TKE near the airfoil trailing edge and the unsteady surface pressure spectra. The fences reduce the TKE near the airfoil (scattering) surface; peak TKE shifts to just above the fence height. The reduced TKE near the surface leads to reduced unsteady surface pressure, which is observed in the simulations and previous measurements. The taller fence gives greater reductions in near-surface TKE, surface pressure PSD, and farfield noise for frequencies greater than 2 kHz.

Spanwise coherence of the unsteady surface pressure near the trailing edge is computed and compared between the baseline and the two fence simulations. Both fences reduce γ^2 at low frequencies for normalized separation distances $\Delta z/c > P/c$. For these frequencies, both fences increase γ^2 in fence passages (i.e., for $\Delta z/c < P/c$) due to a “channeling” effect from adjacent fence sidewalls. This increase is larger for the taller fence. The taller fence is louder than the shorter fence (but not the baseline) for low frequencies. This is hypothesized to be due to (a) increased γ^2 within

fence passages, and (b) additional noise radiated by the leading edge of the taller fence as it is less aligned with the oncoming turbulence in the flow.

CHAPTER 4. NUMERICAL INVESTIGATION OF BIO-INSPIRED FINLETS FOR THE REDUCTION OF AIRCRAFT AND WIND TURBINE NOISE

A version of this chapter will be submitted in June 2019 to the Journal of Fluid Mechanics.

Abstract

Numerical analysis of an airfoil geometry inspired by the down coat of the night owl is presented. The bioinspired geometry consists of an array of “finlet fences”, which is placed near the trailing edge of the baseline (DU96-W-180) airfoil. Two fences with nondimensional thicknesses, $d/\delta^* = 0.107$ and 0.214 are investigated, where δ^* is the displacement thickness at 2.9% chord upstream of the airfoil trailing edge. Wall-resolved large eddy simulations are performed at chord-based Reynolds number, $Re_c = 6 \times 10^5$, flow Mach number, $M = 0.146$, and angle of attack, $\alpha = -0.2^\circ$. The simulation results suggest that the fences should be as thin as possible to minimize the adverse impact on drag and lift. On the suction side near the maximum fence height, there are reductions in the high-frequency surface pressure spectra. However, close to the trailing edge the simulations show no reductions in the high-frequency surface pressure spectra and therefore, no high-frequency farfield noise reduction is predicted. This shows that the reductions in the surface pressure fluctuations *closest* to the trailing edge are ultimately what leads to farfield noise reductions. Larger velocity deficit below the fence height is shown to lead to more reductions in the surface pressure fluctuations. The velocity deficit and source-trailing edge separation distance is shown to work in tandem to reduce the pressure fluctuations near the trailing edge. Although both the pressure and suction side has an increase in velocity near the airfoil surface, since the source-trailing edge separation distance on the pressure side is larger (or large enough), there are still reductions in the surface pressure fluctuations on the pressure side. Higher farfield noise of thicker fence is attributed to scattering of sound from

the top surfaces of the fences. Thinner fences are therefore both aerodynamically and aeroacoustically better than thicker fences.

4.1 Introduction

One biological feature that has yet to be used in engineering innovations is the silent flight of nocturnal owls. One species of nocturnal owls - the barn owl (*Tyto alba*) - is particularly adept at silent flight. In this paper, we refer to the barn owl as ‘the owl’. The owl has unique feather features – leading edge (LE) comb, downy coat on flight feathers, and trailing edge (TE) fringes, are collectively referred to as the “hush kit”. There has been considerable research on using LE and TE features, modeled as serrations, to reduce airfoil noise [29, 30, 31]. The downy coat has been investigated analytically [34, 42] and experimentally [3, 4]. Bodling *et al.* [10, 41] performed numerical studies to investigate the acoustic impact of the owl down coat. In the studies by Bodling *et al.* [10, 41], the downy coat was modeled using “finlet” designs that were first discussed by Clark *et al.* [3]. The “finlets” designed by Clark *et al.* [4] were constructed in two different ways - (a) using an array of sharp-edge fences, and (b) using thin cylindrical rails. Clark *et al.* [3, 4] presented aeroacoustics measurements of trailing edge noise from airfoils with these finlets (fences and rails) installed using a substrate near the trailing edge of the baseline airfoil. The DU96-W-180 airfoil, commonly used in wind turbine applications, was selected as the baseline in the experiments [3, 4].

Figure 4.1 shows schematics of the two finlet designs used in the experiments. Plots (a) and (b) in the figure are the fence and rail configurations, respectively. Farfield sound measurements showed that the finlet designs were significantly quieter than the baseline airfoil [4].

This paper presents results of highly-resolved large eddy simulations of a baseline airfoil as well as the baseline airfoil fitted with a finlet fence design. This research builds upon the authors’ previous studies in simulating finlet fences [10, 41]. Bodling *et al.* [41] investigated the aeroacoustic impact of the shape of the leading edge of the finlet fences and found that it has to be highly skewed (oblique incidence) to the incoming flow to achieve noise reduction. They also noted that the fence finlets increase the separation distance between the energetic turbulent eddies and the airfoil trailing (scattering) edge. Bodling *et al.* [10] studied the effect of varying the height of the finlet fences.

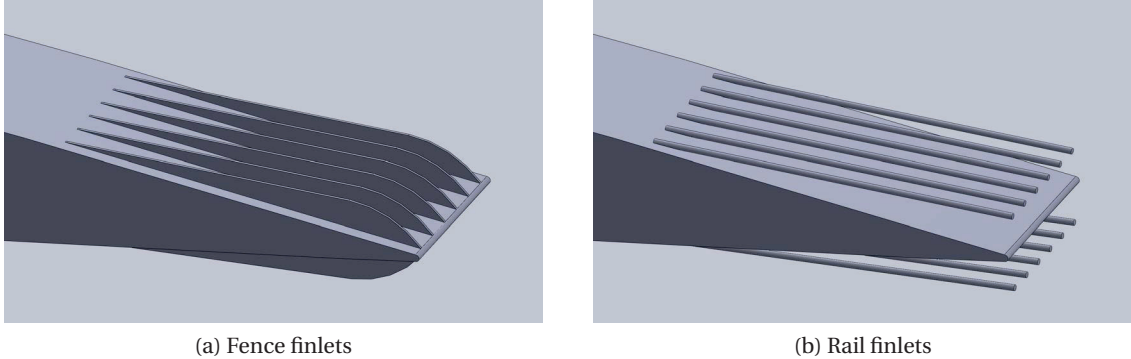


Figure 4.1: Idealized schematics of the two finlet designs used by Clark *et al.* [4].

They found that increasing the height increased the source-trailing edge separation distance, which further reduced the high-frequency noise, but with a higher aerodynamic drag penalty. They also found that the finlet fences decrease the spanwise coherence of the eddies for separation distances greater than a fence pitch. However, they found that the taller fence is louder than the shorter fence (but not the baseline) for low frequencies. This is hypothesized to be due to (a) increased γ^2 within fence passages, and (b) additional noise radiated by the leading edge of the taller fence as it is less aligned with the oncoming turbulence in the flow. In these studies, the NACA0012 airfoil was used instead of the DU96-W-180. To allow one-to-one comparisons with the experimental data from Ref. [4], the same airfoil as in the experiments is used in the current work. Also, the previous work by the authors' [10, 41] was performed at a zero-lift condition. The simulations presented here are at a non-zero lift condition. This will allow a better understanding of the noise reduction physics at realistic operating conditions.

Results from three sets of simulations are presented and compared: baseline airfoil, and baseline airfoil fitted with two fence finlets with thicknesses $d/\delta^* = 0.107$ and 0.214 , where δ^* is the displacement thickness at 2.9% chord upstream of the airfoil trailing edge. Displacement thickness is chosen as the reference length scale for noise analysis as the main mechanism of noise reduction is believed to be displacement of energetic turbulent eddies away from the airfoil trailing edge. Scattering of hydrodynamic waves (turbulence) into sound waves at the trailing edge is the main noise generation mechanism here. The objective is to perform noise source diagnostics using the highly-resolved

flowfield to enhance our understanding of the mechanisms behind the noise reduction observed with finlets.

4.2 Numerical Methodology

The aeroacoustic performance of the baseline and finlet fence models is evaluated using a two-step approach. First, the unsteady flow around the geometry is simulated using a computational fluid dynamics (CFD) solver; time-accurate flow data is collected during the CFD simulation on a surface enclosing the airfoil and the sound sources. In the second step, the surface data is used with an integral method (acoustic analogy) to predict farfield noise. The numerical procedure used in this work has been previously validated and used to assess the noise reduction ability of leading edge serrations [28] and finlets [10, 41, 67]. Details of the compressible flow/acoustics solver, Kato's correction and the transient removal process are given in chapter 3.

4.3 Geometry Modeling, Meshing, and Boundary Conditions

The simulations are carried out at chord-based Reynolds number, $Re_c = 6 \times 10^5$, angle of attack, $\alpha = -0.2^\circ$, and flow Mach number, $M_\infty = 0.146$. The DU96-W-180 airfoil is selected as the baseline airfoil. The baseline airfoil, α and M_∞ selected are the same as that used in the experiment of Clark [1]. For the bioinspired airfoil, finlet fences are added near the airfoil trailing edge. The span length of the airfoil model in the simulations is 6.5% of the airfoil chord. A nested, O-grid is used to generate a 2-D mesh around the baseline airfoil, which is repeated in the span direction to obtain the 3-D grid. The O-grid in the physical space (x, y, z) maps to an H-grid in the computational domain (ξ, η, ζ). The following orientation is used: \hat{e}_ξ points radially out, \hat{e}_η is in the circumferential direction. \hat{e}_ζ is along the span direction such that the right hand rule, $\hat{e}_\zeta = \hat{e}_\xi \times \hat{e}_\eta$ is obeyed.

Periodic boundary condition is used in the span (\hat{e}_ζ) and azimuthal (\hat{e}_η) directions using overset grids with five-point overlaps. The airfoil surface is modeled as a no-slip, adiabatic wall with a zero-normal pressure gradient (4th-order extrapolation). The outer computational domain boundary is approximately 180 chords away from the airfoil and is prescribed as a freestream boundary. The grid is heavily stretched away from the airfoil such that the filtering procedure annihilates all fluctuations

before they reach the outer boundary and avoids spurious reflections. The computational time step, $\Delta\tau$ is chosen to be very small ($= 4 \times 10^{-5}$). Based on the study by Choi and Moin [51], in the turbulent flow region the computational time step in terms of wall units, $\Delta t^+ = \Delta t u_\tau^2 / \nu \leq 0.08$, should be sufficiently accurate to resolve the near-wall turbulence. In the above, $\tau = t U_\infty / c$ is non-dimensional time ($\tau = 1$ is nominally the time it takes for the flow to go past the airfoil), where c is the airfoil chord, t is the dimensional time, and U_∞ is the freestream flow speed.

4.3.1 Baseline Airfoil Mesh and Spatial Resolution Study

Figure 4.2 shows close-up, cross-sectional views of the O-grid around the baseline airfoil. For clarity, every third point in the radial and circumferential directions is shown in Fig. 4.2. The nested O-grid topology is shown in Fig. 4.3. The nested O-grid dimensions and spatial extents are summarized in Table 4.1.

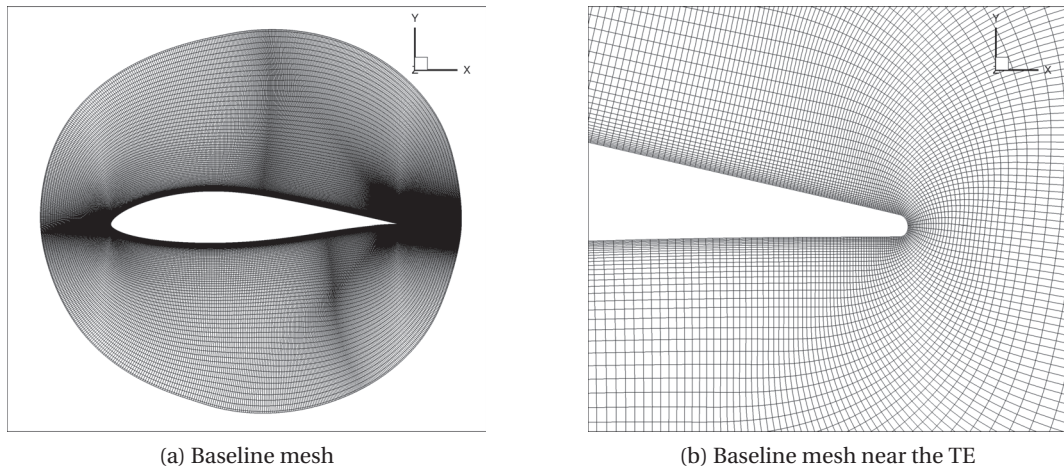


Figure 4.2: The O-grid topology used in the simulations; shown here for the baseline airfoil. The trailing edge is rounded and the mesh near the TE ($0.90 \leq x/c \leq 1.04$) is shown in (b). Every third point along each axis is shown for clarity.

Table 4.1: The baseline nested O-grid dimensions and spatial extent.

Mesh	$N_\xi \times N_\eta \times N_\zeta$	Xmin, Xmax Extent	Ymin, Ymax Extent
1	$263 \times 3080 \times 148$	-0.25, 1.2	-0.53, 0.53
2	$87 \times 2202 \times 108$	-1.38, 2.6	-2.1, 2.1
3	$83 \times 1329 \times 68$	-180, 180	-180, 180

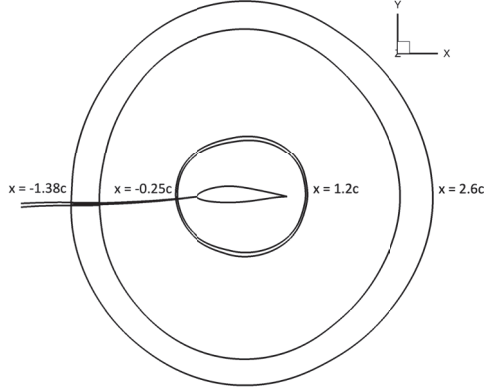


Figure 4.3: The nested O-grid topology used in the simulations.

A grid resolution study is performed to ensure adequate spatial resolution is achieved for the quantities of interest. Table 4.2 shows the grid dimensions and first non-dimensional cell sizes of the inner-most grid block for the coarse, medium and fine meshes; the corresponding x^+ and y^+ distributions are shown in Fig. 4.4. The cell sizes in Table 4.2 are span-averaged over the turbulent flow region ($x/c > 0.5$). Typical values of cell sizes used in previous wall-resolved LES available in the literature are $50 \leq \Delta x^+ \leq 150$, $y_{wall}^+ < 1$, $15 \leq \Delta z^+ \leq 40$, where x is the streamwise direction, y is the wall normal direction and z is in the spanwise/homogeneous direction [50]. The cell sizes for the medium and fine meshes (see Table 4.2) are on the lower range of the values reported in the literature. The effect of spatial resolution is shown in Figs. 4.5 and 4.6 in terms of the time- and span-averaged surface pressure coefficient (C_p) and skin friction coefficient (C_f) distributions over the airfoil. The C_p distribution is nearly unaffected by the spatial resolution, with only small differences between the three grids at the transition location. For the medium and fine grids, there is little difference in the C_f distribution over the airfoil suggesting grid convergence. The comparisons in Figs. 4.5 and 4.6 demonstrate that the turbulent boundary layer is being captured with sufficient spatial resolution by the fine mesh. All results that follow correspond to the fine mesh.

For the fine mesh, the boundary layer on the suction side at $x/c = 0.85$ contains 121 grid points with approximately 14 points in the viscous sublayer. The max grid stretching ratio at the top of the boundary layer is 1.05.

Table 4.2: The baseline grid dimensions and non-dimensional cell sizes in wall units for the coarse, medium and fine inner-most grid block. Average and max values are obtained over the turbulent flow region.

Mesh	$N_\xi \times N_\eta \times N_\zeta$	Δy^+ avg, max	Δx^+ avg, max	Δz^+ avg, max
Coarse	$135 \times 1543 \times 78$	0.86, 1.33	26.2, 103	19.8, 30.4
Medium	$199 \times 2311 \times 114$	0.59, 0.94	18.3, 75.2	13.5, 21.5
Fine	$263 \times 3080 \times 148$	0.44, 0.70	13.8, 57.1	10.2, 16.42

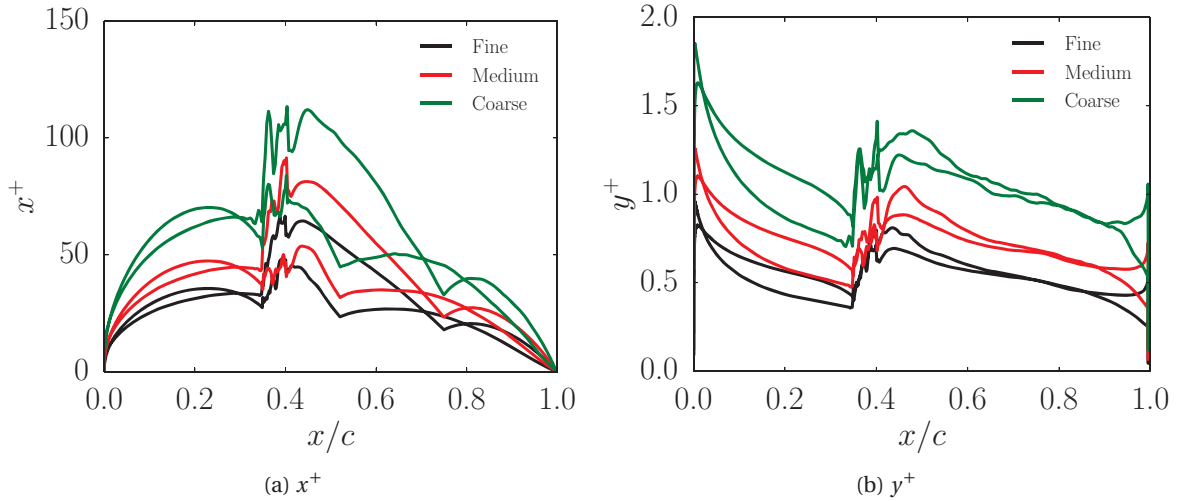


Figure 4.4: Time- and span-averaged (a) x^+ and (b) y^+ distributions using three different spatial resolutions.

4.3.2 Finlet Fence Geometry and Mesh

Figure 4.7 contrasts the geometries of the fences used in the experiments with those used in the simulations. The fence finlets used in the experiment are flushed with the airfoil and rise at a very shallow angle from the airfoil. The fences are modeled as a “stair-step” geometry by varying the height of the fences in discrete steps (as opposed to continuous variation in the experiment model) along the chord. A large number of steps are used to approximate the fence geometry as a stair-step such that it closely approximates the continuous geometry of the experiment. The final height is reached over 24 discrete steps. Figure 4.8 shows a schematic of the modeled fence geometry with a nomenclature of the key dimensions.

The meshes for the fence simulations are obtained from the baseline mesh by performing *hole-cutting* (also called point blanking). Hole-cutting involves removing mesh points that represents the interior of a solid body; fences in this case. The PEGASUS software [52] is used to perform hole-

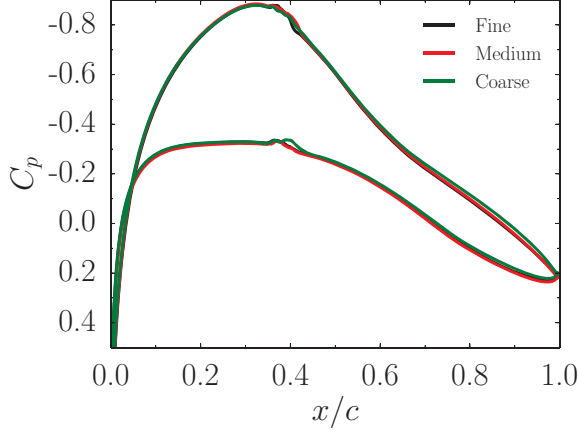


Figure 4.5: Time- and span-averaged C_p distributions on baseline airfoil using three different spatial resolutions.

cutting. The regions occupied by the fences (defined by specifying ranges $\xi_1 - \xi_2$, $\eta_1 - \eta_2$, and $\zeta_1 - \zeta_2$) are removed (cut out) from the baseline grid and the no-slip adiabatic wall with a zero-normal pressure gradient boundary condition (4th order extrapolation) is applied to the new boundaries thus created. Care has to be taken when filtering the solution around these new boundaries; these details are provided in Appendix C.

Figure 4.9 shows cross-sectional views of the mesh for the fence (side view is identical for the two different fence thicknesses); the views are zoomed in on the fence region to clearly show the fence geometry. Every other grid point along the radial axis and every 3rd point along the circumferential axis is shown for clarity. The cross-sectional view is in a plane where a fence is present. The grid points in the grey regions between the airfoil surface and the red curves are blanked out (removed) from FDL3DI computation. The red curves indicate the no-slip boundaries created due to hole-cutting. The fences begin at $x/c = 0.872$ (most upstream location) and reach their maximum height (H) at $x/c = 0.971$. Scaled by the displacement thickness of the baseline airfoil, the maximum nondimensional height of the fences on the suction and pressure sides are $H/\delta^* = 1.71$ and 2.8, respectively.

Figure 4.10 shows top views of the baseline and the thin and thick fence meshes. The thin and thick fences are 2 and 4-cells thick, respectively, in the current simulations. For the thin fence, this corresponds to a nondimensional thickness of $d/\delta^* (= 0.107)$ and $d/\delta^* (= 0.175)$ on the suction and

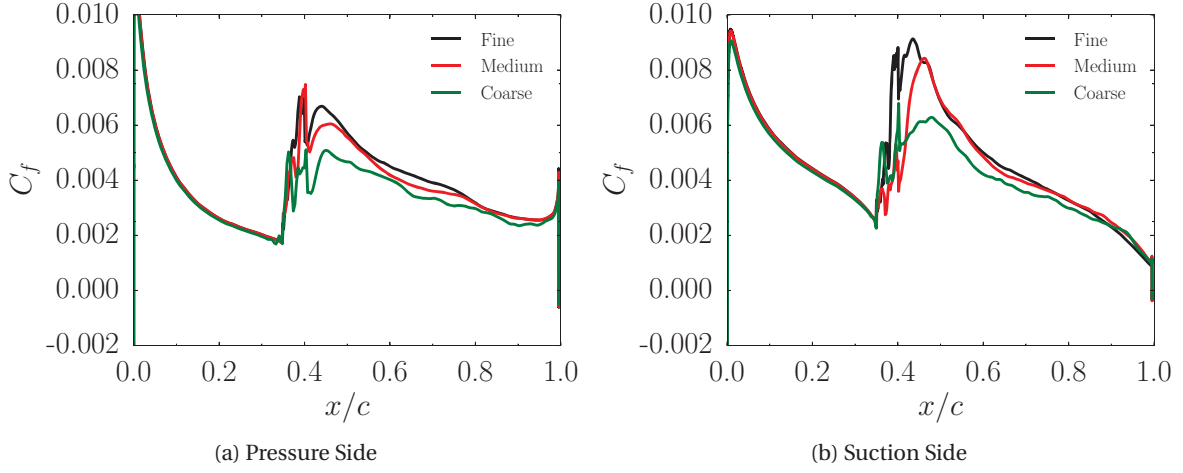


Figure 4.6: Time- and span-averaged C_f distributions on (a) pressure side and (b) suction side of baseline airfoil using three different spatial resolutions.

pressure sides, respectively. The thick fence was made to be double the thickness of the thin fence. An open area percentage of 80.0% and 90.0% is used for the thin and thick fences, respectively. The scaled pitch (distance between two adjacent fence walls) for the thin and thick fence is P/δ^* ($= 1.07$) and P/δ^* ($= 1.75$) on the suction and pressure sides, respectively. The nondimensional height/pitch, location of the most upstream point, and the location of the maximum height of the two fence designs are the same as that used in the experiment of Clark [1]. The thickness and open-area percentage of the thick fence is also the same as used in the experiment. Note that the displacement thicknesses near the trailing edge of the pressure and suction sides of the airfoil are different (with suction side being greater). Therefore, although the nondimensional fence parameters are different on the pressure and suction sides of the airfoil, the *dimensional* lengths are the same.

A mesh containing a single fence element (one fence pitch wide) is created and then repeated seven times along the span to obtain a 3-D mesh with a span of 6.5% chord. It should be emphasized that other than the holes introduced in the fence meshes, the grids for the baseline and fence are identical. This eliminates grid-to-grid differences in the simulation results when comparing the different designs.

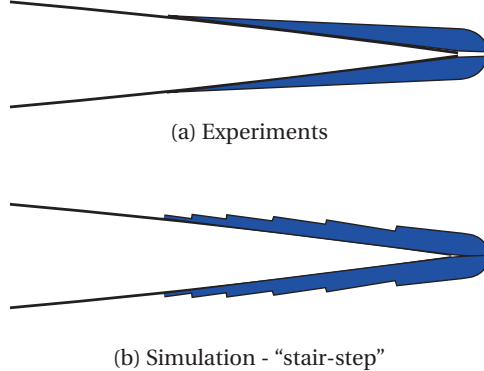


Figure 4.7: Schematics highlighting the differences in the fence geometries between the experiments and the current simulations.

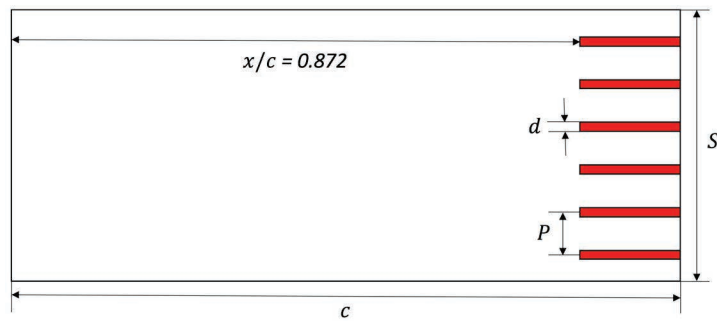


Figure 4.8: Schematic of the fence geometry as modeled: P is the fence pitch, d is fence thickness, c is airfoil chord length, and S is the airfoil span.

4.3.3 Boundary Layer Trip

Since the simulation Re_c ($= 6 \times 10^5$) is smaller than that of the experiments ($= 2.5 \times 10^6$), the boundary layer on the airfoil surface is forcibly tripped in the simulations. It should be noted that a boundary layer trip (serrated tape) was also used in the experiments [4]. In the simulations, boundary layer tripping is achieved by using high frequency unsteady tangential reverse blowing. This is implemented on the pressure and suction sides from $0.35 < x/c < 0.40$ by updating the velocity at the wall to be tangent to the wall and point upstream and then scale the u , v and w components using the expressions below,

$$|V| = \sqrt{u^2 + v^2 + w^2} \quad (4.1)$$

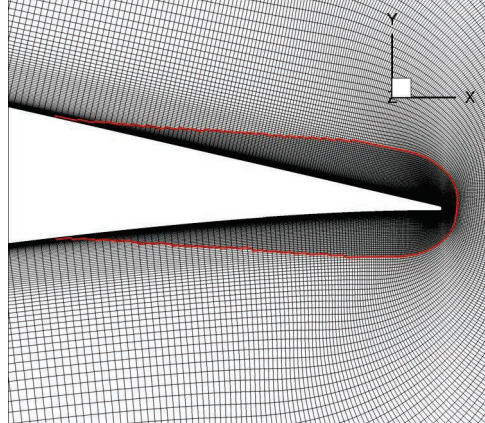


Figure 4.9: Cross-sectional (zoom) views of the computational meshes used to simulate the fence geometry. Every other grid point along the radial axis and every 3rd point along the circumferential axis is shown for clarity. Fence meshes for thin and thick fence are identical from the side.

$$u = [\sin(2\pi \tilde{f}\tau) + 1.0] * SF * u/|V| \quad (4.2)$$

$$v = [\sin(2\pi \tilde{f}\tau) + 1.0] * SF * v/|V| \quad (4.3)$$

$$w = [\sin(2\pi \tilde{f}\tau) + 1.0] * SF * w/|V| \quad (4.4)$$

where τ is the computational non-dimensional time, SF is an empirical scaling factor, \tilde{f} is the non-dimensional blowing frequency and $|V|$ is the velocity magnitude. From experimentation, \tilde{f} and the empirical scaling factor (SF) is specified as 25,000 and $0.185U_\infty$, respectively, which minimizes the amount of undesirable noise emanating from the transition region.

Q contours are a three dimensional vortex criterion that is used to detect and visualize vortices. The scalar is defined by the equation below,

$$Q = \frac{1}{2} [|\boldsymbol{\Omega}|^2 - |\boldsymbol{S}|^2], \quad (4.5)$$

where $\boldsymbol{\Omega}$ is the vorticity tensor and \boldsymbol{S} is the rate of strain tensor. Figure 4.11 shows iso-surfaces of Q -criterion ($Q = 10$) for the baseline airfoil with the unsteady reverse blowing boundary

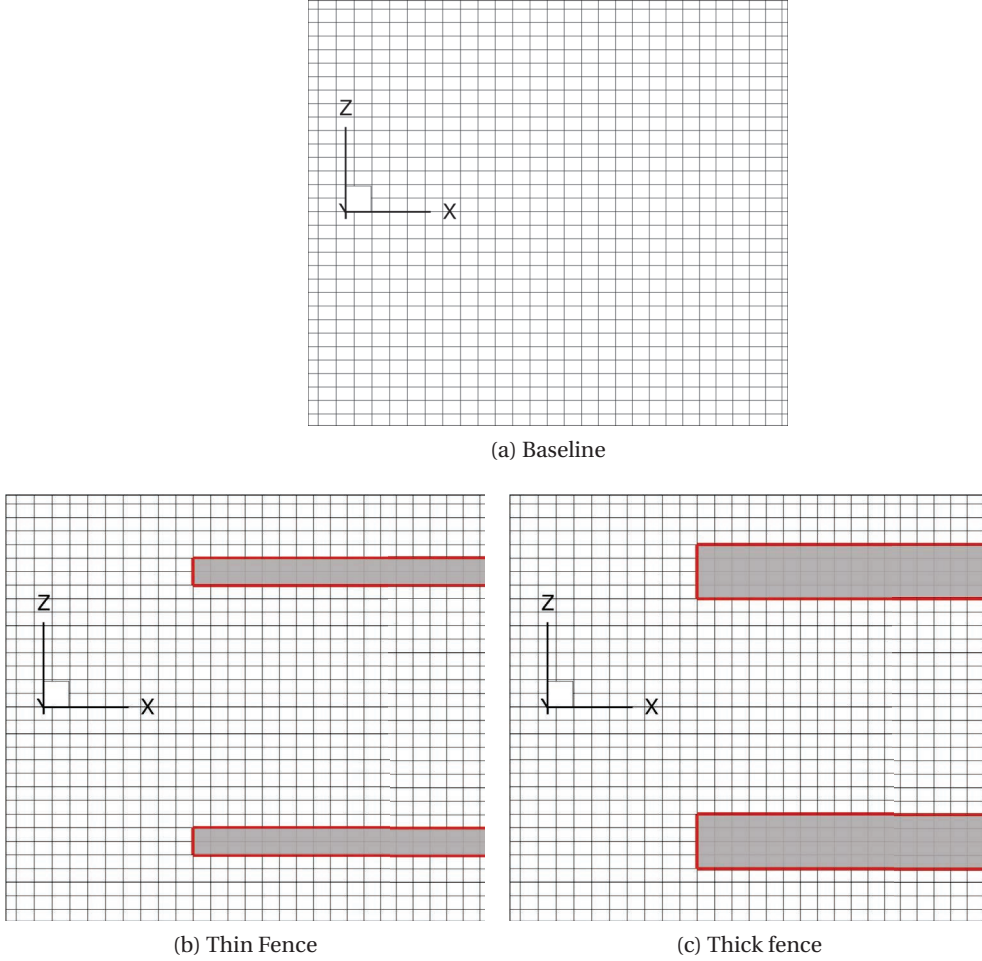


Figure 4.10: Top views of the (a) baseline (b) thin and (c) thick fence meshes. The thin and thick fences are 2 and 4-cells thick, respectively, in the simulations.

tripping mechanism implemented. The tripping mechanism achieves a turbulent boundary layer similar to what would occur via natural transition at high Re_c .

4.4 Results

The baseline validation results are presented first, followed by comparisons of the baseline and fence aerodynamic performance. Finally, the acoustic performance is analyzed and the noise reduction mechanisms are explained.

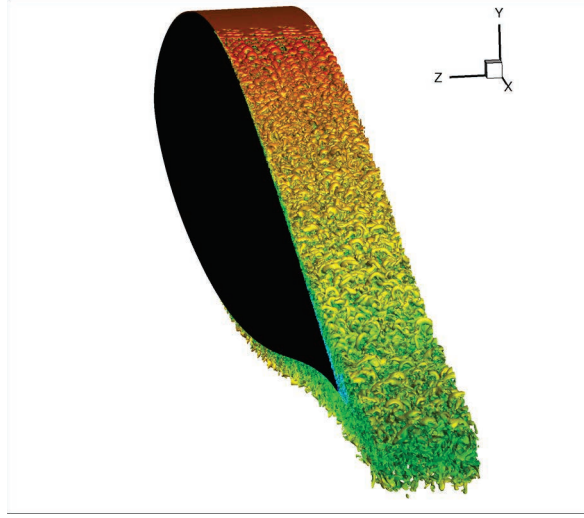


Figure 4.11: Iso-surfaces of the Q-criterion ($Q = 10$) for the unsteady tangential reverse blowing boundary layer tripping mechanism.

4.4.1 Baseline Validation

Figure 4.12 (a) compares the predicted time- and span-averaged aerodynamic pressure coefficient (C_p) distributions of the baseline airfoil with the experimental data from Clark [1] and with XFOIL [53] predictions. Along the entire airfoil, there is good agreement between FDL3DI and XFOIL. Before the airfoil is tripped in FDL3DI, there are differences in the C_p values between FDL3DI and the experiment, primarily on the suction side (curves with more negative value of C_p). To test whether this is due to differences in the Reynolds number between the experiment and FDL3DI, predictions with XFOIL are performed at the same Reynolds number as the experiment. As shown in Fig. 4.13, there are still differences in the C_p value between XFOIL and the experiment, primarily on the suction side. Furthermore, in a RANS CFD result by Clark [1], where the Reynolds number was matched with the experiment, similar differences as FDL3DI were seen between the experiment and predictions. Therefore, the differences observed do not appear to be due to the differences in the Reynolds number between FDL3DI and the experiment. Additional calculations (not shown here) showed that the differences between XFOIL and the experiment remained even as the angle of attack was varied in XFOIL from -0.2° to 0.1° . Thus, the uncertainty in the tunnel-corrected angle of attack does not appear to be a factor as well. The above conclusions leads us to believe that the differences before transition are due to blockage effects in the experiment. These blockage effects

can be mitigated by correcting the angle of attack to match the integrated lift, but the exact pressure distribution cannot be perfectly matched. Although this difference in C_p distribution at the suction peak exists, note that in the aft portion of the airfoil where we are most interested in the physics, there is excellent agreement in the C_p distribution between FDL3DI and the experimental data.

Figure 4.12 (b) compares the skin friction coefficient (C_f) distribution over the airfoil surface between FDL3DI and XFOIL predictions. Excellent agreement is seen on the suction side (red curves with higher value of C_f). XFOIL predicts a lower value of C_f on the pressure side in the aft portion of the airfoil. Since the pressure side has a smaller adverse pressure gradient than the suction side (where XFOIL agrees better with FDL3DI), the differences seen are likely due to how FDL3DI and XFOIL initiate transition; on a greater adverse pressure gradient, the effects of how the boundary layer is tripped would be less significant since the flow is more susceptible to transition. It should be noted that the baseline grid C_f values do not change in the aft portion of the pressure side of the airfoil with further refinements of the grid. The disagreement between XFOIL and FDL3DI is due to the modeling differences and FDL3DI is a much higher fidelity method.

Figure 4.14 compares the baseline time- and span-averaged normalized velocity (U^+) profiles at different chordwise locations on the aft portion of the suction side of the airfoil. The profiles follow the expected $U^+ = y^+$ trend in the viscous sublayer, showing that the viscous sublayer is well resolved throughout the turbulent region. The slope in the log-law region is found to be close to 1/0.41 once the flow has fully developed, which is in agreement with the value of 1/0.41 obtained with the von Kármán constant. Bodling *et al.* [10] performed an LES of a NACA 0012 at $Re_c = 5 \times 10^5$ and found that the slope in the log-law region was close to 1/0.34. Nagib *et al.* [63] found that the von Kármán constant is dependent on the flow geometry and pressure gradient. The DU96-W-180 airfoil used in the current predictions has a much larger pressure gradient on the suction side than the NACA 0012 airfoil. Therefore, the closer agreement with the von Kármán constant in the current predictions further supports the conclusions made by Nagib *et al.* [63].

Figure 4.15 compares the normalized Reynolds stresses for the baseline airfoil as computed using the current FDL3DI simulations and the DNS of a turbulent boundary layer with an adverse pressure gradient by Spalart and Watmuff [6]. In the DNS, the pressure gradient parameter ($\beta = (\delta^*/\tau_w)dp/dx$), varies from 0 to 2 in the x direction, where the Reynolds stresses are at an x/c

location ($x/c = 0.8$) corresponding to $\beta = 1$. The Reynolds number based on this x -coordinate is $Re_x = 3.4 \times 10^5$. The data from the FDL3DI predictions has a $\beta \approx 1$ at $x/c = 0.72$, and the data corresponds to this location. Excellent agreement is seen with the DNS results near the wall. Away from the wall, satisfactory agreement is seen, where the differences are likely due to the different flow geometries/Reynolds numbers that are used.

Figure 4.16 shows the effect of the time-step on the normalized surface pressure spectrum for the baseline airfoil at $x/c = 0.99$. The spectrum is normalized by the inner variables as $\Phi(\omega)/(\tau_w^2 \nu / u_\tau^2)$, where τ_w is the wall shear stress, ν is the kinematic viscosity, u_τ is the friction velocity and ω is the angular frequency. Shown on the graph are the spectra for two different time-steps as well as the ω^{-5} power law behavior that is associated with sources in the boundary layer below y^+ of 20 [62]. The effect of the time-step on the surface pressure spectrum appears to be minimal. For the two different time-steps used, there is also minimal change to the drag and lift. Therefore, a time-step of $\Delta\tau = 4 \times 10^{-5}$ was deemed sufficient for resolving the temporal scales of the flow.

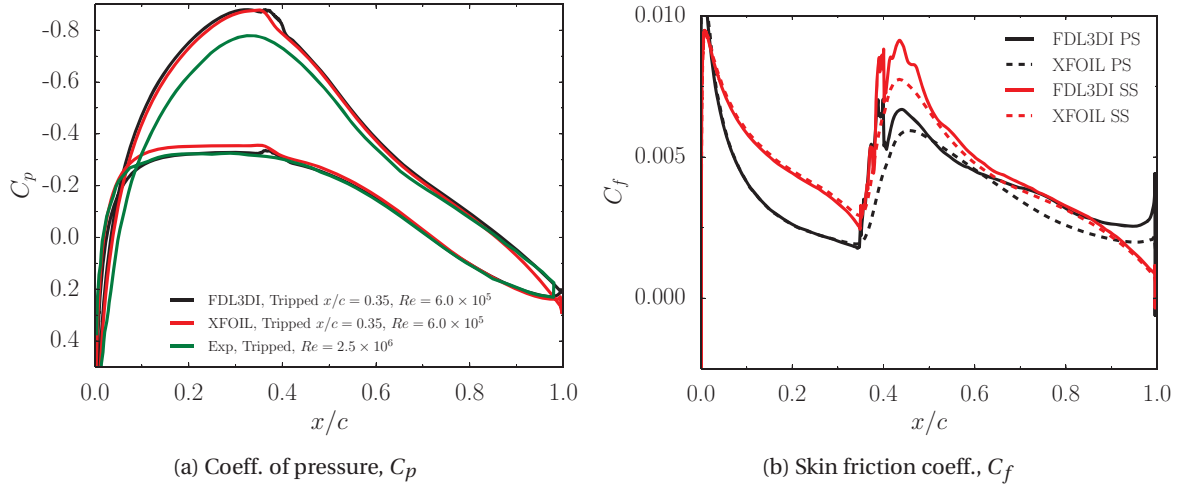


Figure 4.12: Time- and span-averaged C_p and C_f distributions from FDL3DI predictions ($Re_c = 6 \times 10^5$) compared with experiments ($Re_c = 2.5 \times 10^6$) and XFOIL simulations ($Re_c = 6 \times 10^5$).

Coherence squared, γ^2 , between two points \mathbf{x} and \mathbf{y} is defined as

$$\gamma_{xy}^2(\omega) = \frac{|S_{xy}(\omega)|^2}{S_{xx}(\omega)S_{yy}(\omega)}, \quad (4.6)$$

where $S_{xx}(\omega)$ is pressure spectral density, $S_{pp}(\omega)$ evaluated at point \mathbf{x} and $S_{yy}(\omega)$ is $S_{pp}(\omega)$ evaluated at point \mathbf{y} . For spanwise coherence, points \mathbf{x} and \mathbf{y} are at a given chordwise location (x/c) but sepa-

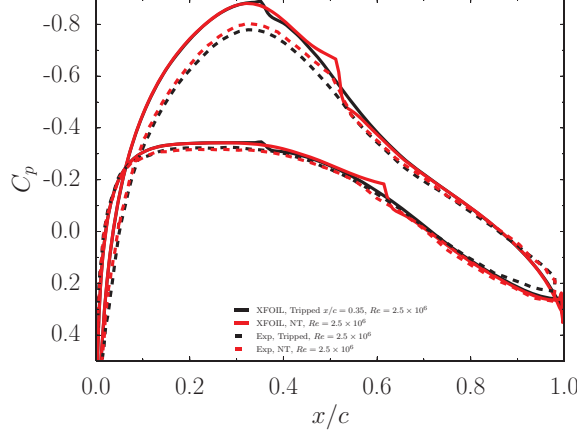


Figure 4.13: XFOIL predictions ($Re_c = 2.5 \times 10^5$) compared with experiments ($Re_c = 2.5 \times 10^6$) for both natural and forced transition.

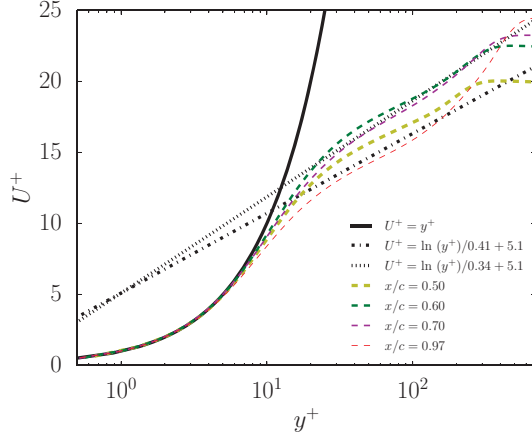


Figure 4.14: Baseline time- and span-averaged velocity profiles compared with the expected trends in the near-wall and log-law regions.

rated in the span direction such that $\mathbf{y} = \mathbf{x} + \Delta z \hat{e}_k$, where \hat{e}_k is a unit vector along the span direction. The reference location to compute spanwise coherence is varied along the span. Each grid point is selected as a reference to compute one instance of coherence. All the instances of coherence so computed (148 in total) are then averaged to obtain the γ^2 reported here.

Spanwise coherence is typically used to assess if the simulated span in a CFD simulation is sufficient for all sources of sound to radiate independently. For the baseline simulation, $\gamma_{xy}^2(\omega)$ is computed using Eq. 4.6 and the Welch spectrogram method [55] with 3125 samples of data ($\approx 5\tau$) divided into 30 segments with a 50% overlap. The Hanning window is applied over each segment.

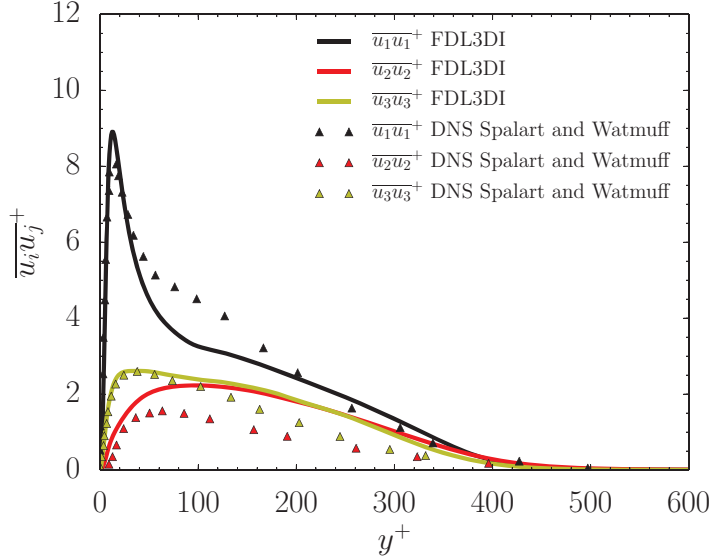


Figure 4.15: Comparison of FDL3DI predictions of normalized Reynolds stresses for the baseline airfoil with DNS results of a turbulent boundary layer in an adverse pressure gradient from Spalart and Watmuff [6]. The Reynolds stresses are at an x location corresponding to $\beta = 1$.

Zero padding is not used in computing the Fourier transforms. Figure 4.17 plots the $\gamma^2(\omega)$ evaluated at various locations along the suction side at frequency, $f = 543$ Hz. Figure 4.18 shows the $\gamma^2(\omega)$ distributions on the pressure (a) and suction (b) sides of the airfoil for three frequencies and at three x/c locations along the airfoil. The figures show that the spanwise coherence decays to near zero suggesting that the span length in the simulations is sufficient.

4.4.2 Baseline and Fence Aerodynamic Comparison

Comparisons of the drag C_D and lift C_L coefficients for the baseline and the two fence simulations are shown in Table 4.3. Compared to the baseline, both fences increase the C_D and decrease the C_L value, with the thinner fence performing better of the two. The fences have a larger impact on drag than lift. However, for both fence cases, the C_D increase is less than the increase in the wetted area due to the additional surface area on the front and sides of the fences. Table 4.4 shows the C_D and C_L values from the experiment of Clark [1]. The impact on the aerodynamic performance with the fences in the experiment is similar to what is observed in the current predictions; the fences increase the C_D and decrease the C_L value, and the increase in C_D is less than the increase in the wetted surface area. In a different experiment from Clark *et al.* [68], they found that the lift decreased

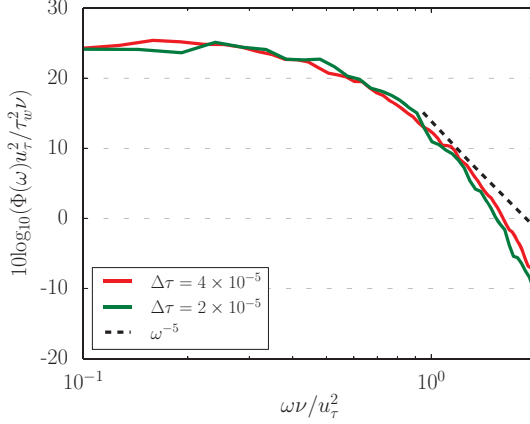


Figure 4.16: Predicted span-averaged surface pressure spectrum for the baseline airfoil at $x/c = 0.99$ on the suction side for two different time-steps; the spectrum is normalized by the inner variables.

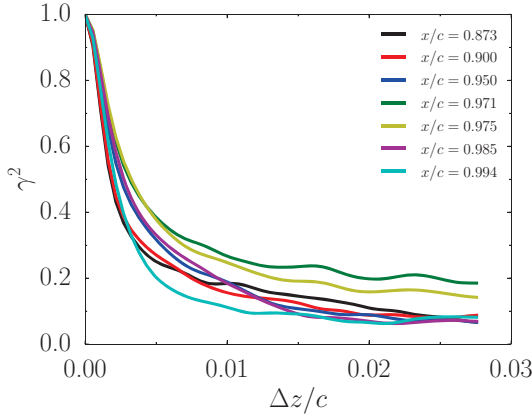


Figure 4.17: Low frequency ($f = 543$ Hz) γ^2 along chordwise direction on suction side.

more with thicker fences as well. The adverse impact of the fences in terms of drag increase is less in the experiment than in the predictions; this is due to the difference in the additional wetted surface area due to the fences; the increase in wetted surface area is higher in the simulations to maintain the same H/δ^* ratio.

To better understand how the fences impact the drag and lift of the airfoil, comparisons of the C_p distributions for the baseline and two fence simulations are shown in Fig. 4.19 (a). The effects of the fences are limited to the fence region. Away from the fence region, the C_p distributions are nearly identical. However, in the fence region, in front of both fences there is an increase in C_p and between the fences the C_p drops; the thicker fence has a larger C_p drop and therefore the C_L decreases

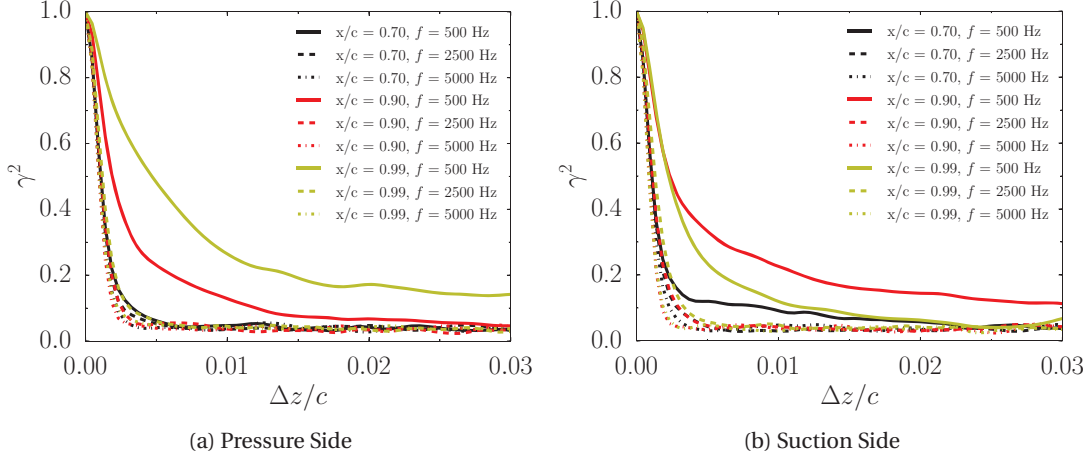


Figure 4.18: Spanwise coherence squared (γ^2) on the a) pressure and b) suction surface of the baseline airfoil at $x/c = 0.70, 90$, and 0.99 for $f = 500, 2500$ and 5000 Hz.

more with the thicker fence. It is worth noting that in previous NACA 0012 zero-lift predictions from Bodling *et al.* [10, 41], the fences impacted the C_p distribution similar to the current predictions; namely, the C_p increased in front of the fences and dropped within the fence region.

Figure 4.19 (b) shows the experimental data from Clark [1]. Although the experiment is at a much higher Reynolds number, there is excellent qualitative agreement between the predictions and experimental data. The effects of the fences appear to be well captured, where the pressure increases and drops are seen in both the predictions and experiment. Also, in both the experimental data and predictions the pressure side C_p distribution is more affected by the fences than the suction side.

Figure 4.20 shows the C_f distribution for the baseline and both fence simulations on the pressure and suction sides. Once again, the effect of the fences is limited to the fence regions. As observed with the C_p distribution, the thinner fence has lesser impact on the C_f distribution. On the suction side, for the thicker fence, C_f drops right before the fences but then is the same as the baseline throughout the fences. With the thinner fence, C_f decreases slightly within the fence region. On the pressure side, for the thicker fence, C_f drops before the fences as well, but then compared to the baseline, increases throughout the fence region. For the thinner fence, the C_f distribution is nearly unchanged within the fence region. The reason for the differences in the pressure and suction side with the thicker fence could be due to the differences in the H/δ^* ratios. The pressure side has

a much higher value of H/δ^* . Therefore, on the pressure side the fences protrude more into the boundary layer than on the suction side. The fence perhaps acts as vortex generators that transfer higher-momentum outer boundary layer flow to near the surface and hence, the C_f increases within the fence region. With the thinner fence, since the fence interacts less with the boundary layer, the smaller differences between the suction and pressure sides are expected. It is worth noting that in previous simulations from Bodling *et al.* [10, 41], the C_f was found to *reduce* within the fence region. In the current simulations this only occurs on the suction side for the thinner fence. This may have interesting consequences on farfield noise radiation, which is explored next.

Table 4.3: Drag (C_D) and lift (C_L) coefficient comparisons between the baseline and fence simulations.

Geometry	C_D	C_D %increase	Wetted area %increase	C_L	C_L %decrease
Baseline	0.00999	–	–	0.275	–
$d/\delta^* = 0.107$	0.0114	14.1	22.8	0.265	3.7
$d/\delta^* = 0.214$	0.0118	18.6	22.9	0.258	6.0

Table 4.4: Drag (C_D) and lift (C_L) coefficient comparisons between the baseline and fence experiment from Clark [1].

Geometry	C_D	C_D %increase	Wetted area %increase	C_L	C_L %decrease
Baseline	0.0097	–	–	0.225	–
$d/\delta^* = 0.214$	0.0104	7.2	8.0	0.203	9.7

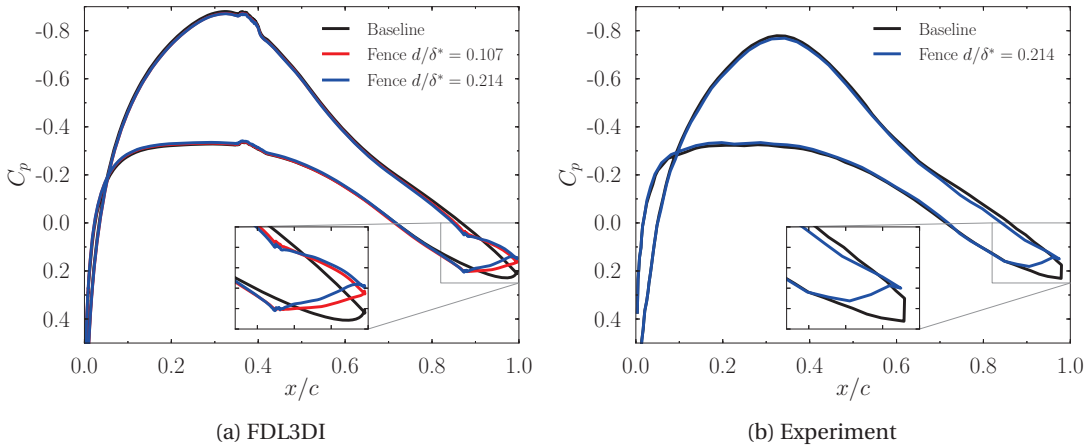


Figure 4.19: Time- and span-averaged C_p distributions for the baseline and fence geometry from a) FDL3DI predictions ($Re_c = 6 \times 10^5$) compared with b) experiment ($Re_c = 2.5 \times 10^6$). Measured data is from Clark [1].

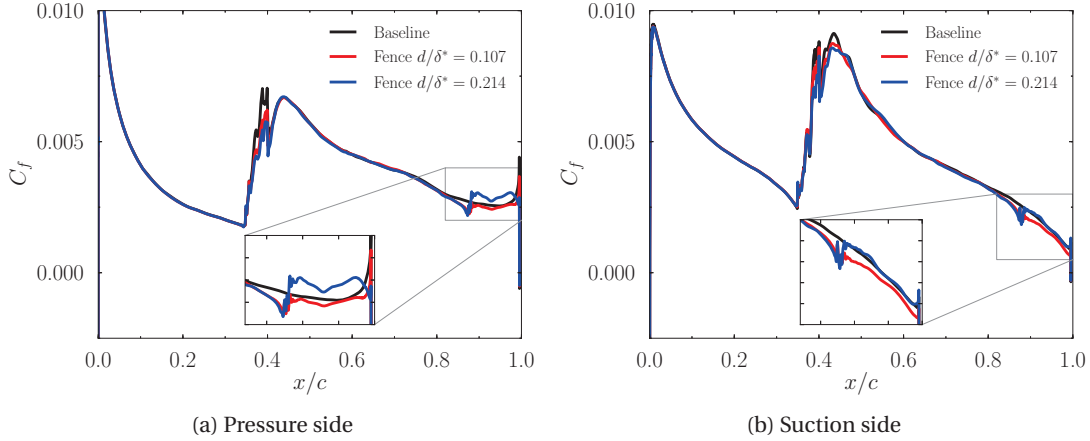


Figure 4.20: Comparison of the baseline and fence time- and span-averaged C_f distribution on the (a) pressure side and (b) suction side.

4.4.3 Baseline and Fence Aeroacoustic Comparison

The in-house Ffowcs Williams-Hawkins (FW-H) solver described in Sec. 3.2.2 is used to calculate the far field noise. The sound sources are located around the trailing edge of the airfoil. Therefore, a porous C-grid integration (Kirchoff) surface is used that is approximately $0.15c$ away from the airfoil surface and extends downstream to $x/c = 1.5$. Data is sampled for two and a half characteristic times ($\tau = 2.5$) for a total of 1561 samples. The data is segmented into 16 intervals for spectral averaging using Welch's method [55]. The predictions do not change for sample durations more than $\tau = 2.5$.

Figure 4.21 plots the predicted far field noise spectra for the baseline and the two fences at various azimuth angles on the suction side of the airfoil. The azimuth angle is measured from downstream, and is positive in the counter-clockwise direction. The origin of the coordinate system is at the airfoil trailing edge. The observers are 12 chords away from the trailing edge and in the mid-span plane. The dimensional frequencies in Fig. 4.21, and in the remainder of the text are obtained by scaling the nondimensional simulation results to the experimental conditions. The reference length and velocity scales in the experiment [1] are: airfoil chord length of 0.8 m and free stream velocity of 50 m/s.

As shown in Fig. 4.21, across all azimuth angles and frequencies, the farfield SPL of both fences is equal to or larger than the baseline, especially at high frequencies. Comparing the two fence de-

signs, the thinner fence has a slightly lower SPL value throughout all frequencies. Also, the biggest difference between the baseline and the fences is at lower azimuth angles.

Figure 4.22 plots the predicted far field noise spectra for the baseline and the two fences at various azimuth angles on the pressure side of the airfoil. Once again the thinner fence has slightly lower SPL than the thicker fence for nearly all frequencies. However, in contrast with the suction side, at all azimuth angles shown, there is some low-frequency ($f < \approx 1\text{kHz}$) noise reduction for the thinner fence.

Figure 4.23 shows farfield directivity comparisons at low, mid and high frequencies. Looking at the low frequencies in Fig. 4.23 (a) and (b), there is some noise reductions observed with the thinner fence on the pressure side. The thicker fence has higher SPL than the baseline nearly everywhere. For the higher frequencies (e.g., 1521 Hz and 2606 Hz) both fences are louder than the baseline for all azimuth angles.

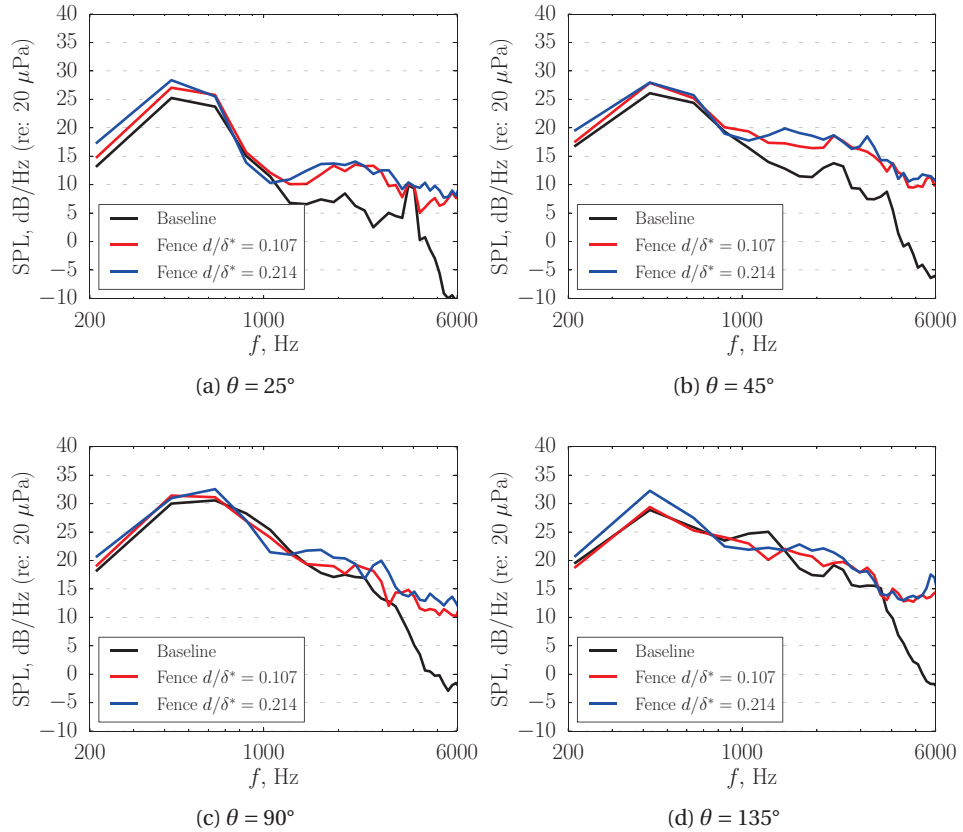


Figure 4.21: Farfield noise spectra at $\theta =$ a) 25° , b) 45° , c) 90° , and d) 135° .

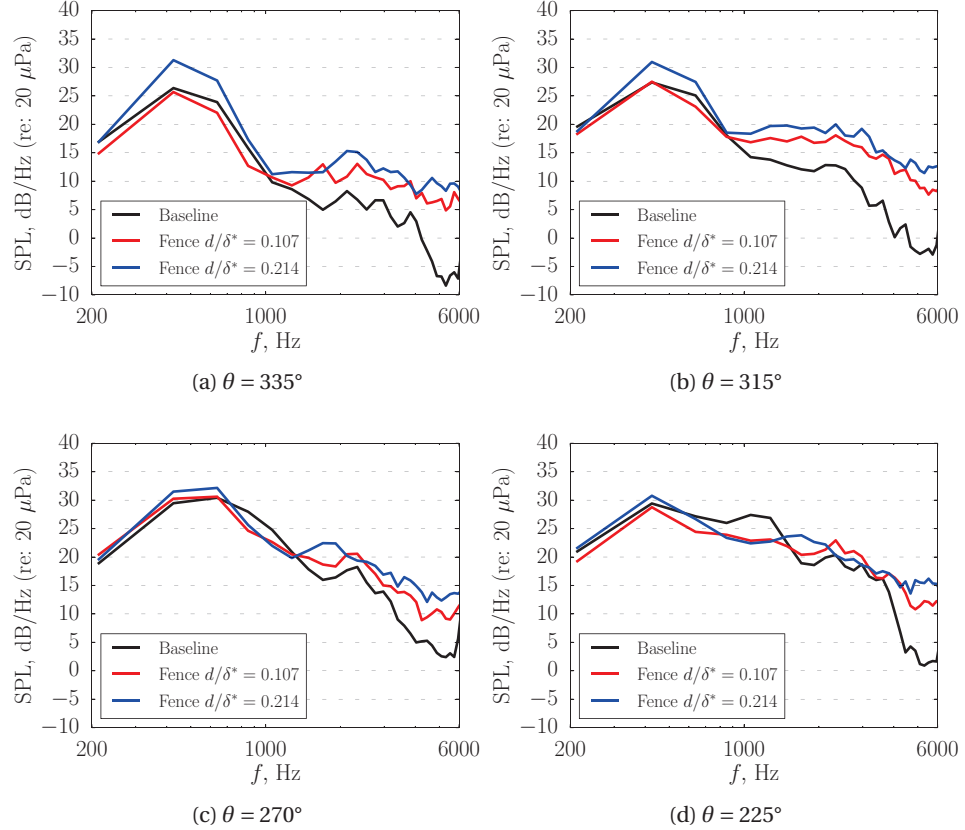


Figure 4.22: Farfield noise spectra at a) $\theta = 335^\circ$, b) 315° , c) 270° , and d) 225° .

4.4.4 Noise Reduction Mechanisms

This section explains the lack of high frequency noise reduction in the simulation results by comparing to previous simulations that demonstrated noise reductions with fences at all frequencies. The reasons for the farfield noise differences between the thin and thick fences are also explained.

Lack of High Frequency Noise Reduction

The unsteady surface pressure fluctuations at the trailing edge are the source of trailing-edge noise [40]. Comparisons of the surface pressure spectra near the trailing edge at $x/c = 0.971$ for the pressure and suction sides is shown in Fig. 4.24. Compared to the baseline, there is a reduction in the surface pressure SPL observed with the fences for frequencies approximately above 1 kHz; the SPL is reduced slightly more for the thicker fence. Below 1 kHz there is a slight increase in the surface pressure SPL for both fences.

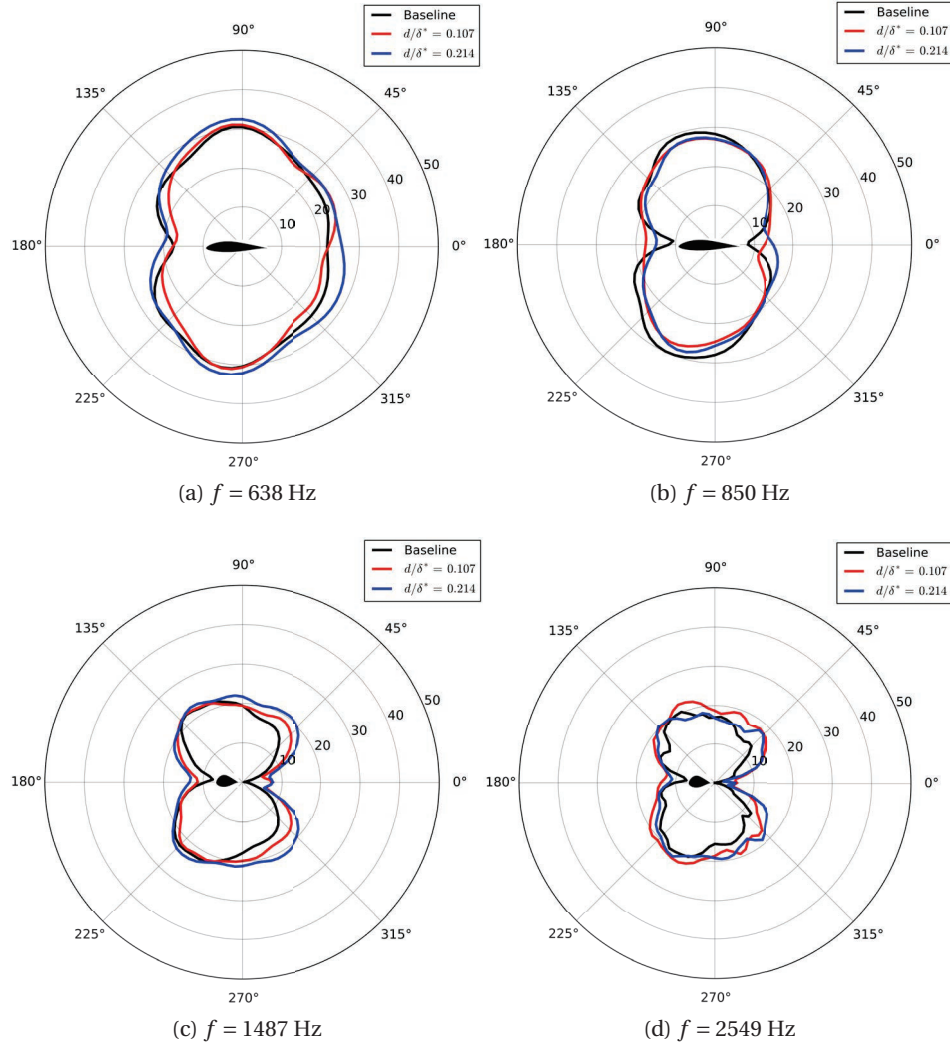


Figure 4.23: Farfield noise directivity at a) 638 Hz, b) 850 Hz, c) 1487 Hz, and d) 2549 Hz. Baseline is in black, $d/\delta^* = 0.107$ fence is in red and $d/\delta^* = 0.214$ fence is in blue.

The surface pressure spectra from Clark [1] are shown in Fig. 4.25. The current predictions agree with the measured data on the suction side. In the experiment, reductions on the suction side are observed for $f > 1 \text{ kHz}$, and a small increase of the SPL is observed for $f < 1 \text{ kHz}$; this trend and magnitude of SPL reduction is the same as in our predictions. However, no reductions in the surface pressure spectra are observed on the pressure side in the experiment, while our predictions show some reduction at high frequencies.

We have seen here that in both the experiment from Clark *et al.* [1] and the current simulations, reductions in the high frequency surface pressure spectra was observed on the suction side at the

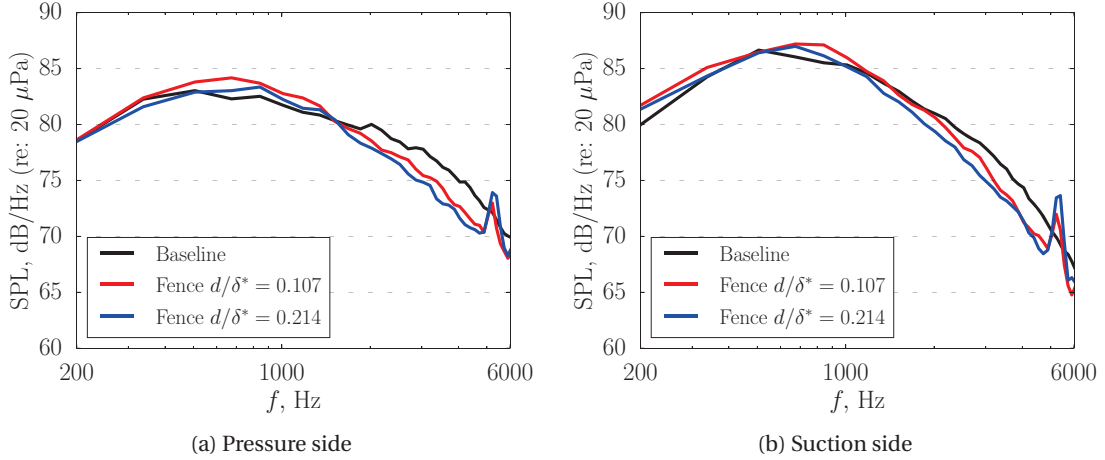


Figure 4.24: Comparison of the baseline and fence surface pressure spectra at $x/c = 0.971$ on the (a) pressure side and (b) suction side.

maximum fence height. What is more, the current predictions saw reductions in the surface pressure spectra on the pressure side as well, which did not occur in the experiment. However, the experiment resulted in farfield noise reductions, which is not the case in the current predictions. The reason for the lack of high frequency farfield noise reductions is explained by comparing the current results to the predictions from Bodling *et al.* [10]. Bodling *et al.* [10] performed an LES of a NACA 0012 airfoil at $\alpha = 0^\circ$ and $Re_c = 5 \times 10^5$ with finlet fences placed at the trailing edge; reductions in the high frequency farfield noise was observed with the two fence cases tested. Also for the two fence cases, as shown in Fig. 4.26 reductions in the high-frequency surface pressure spectra was observed at both the maximum fence height ($x/c = 0.971$) *and* close to the trailing edge ($x/c = 0.994$); in trailing edge noise theories, the trailing edge is the mathematical singularity that scatters the hydrodynamic turbulence energy into acoustic energy. Therefore, pressure fluctuations close to the trailing edge are key. Figure 4.27 plots the surface pressure spectra on the pressure and suction side at $x/c = 0.994$ from the current predictions. In contrast, the current predictions show no reductions with the fences on the suction side close to the trailing edge ($x/c = 0.994$). Therefore, this is the reason for the lack of farfield noise reductions in the current predictions.

This leaves the question of why is there not reductions in the surface pressure spectra close to the trailing edge in the current predictions, but there were reductions in the previous predictions from Bodling *et al.* [10]. We can better understand this by observing trends in previous experiments

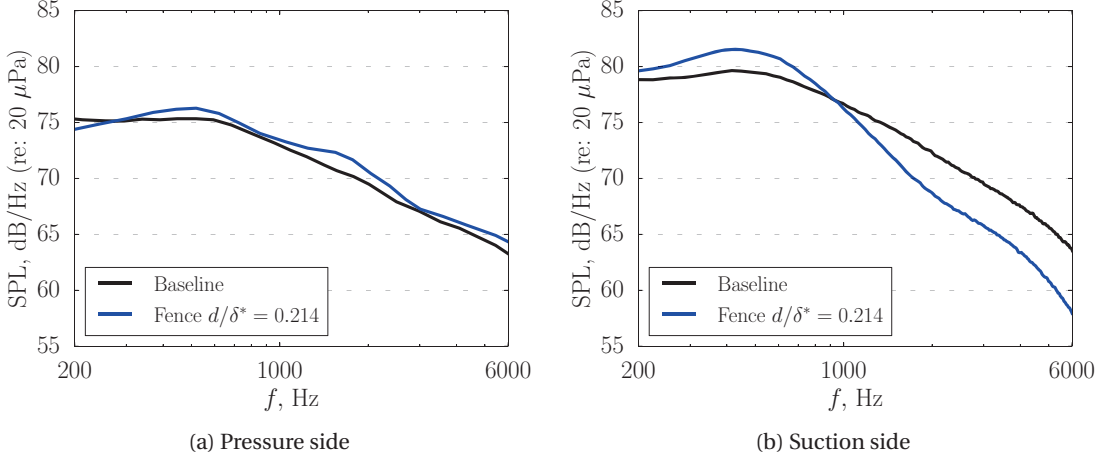


Figure 4.25: Comparison of the baseline and fence surface pressure spectra at $x/c = 0.971$ on the (a) pressure side and (b) suction side. Measurements are from Clark [1].

and simulations. Millican [11] placed finlet fences on a flat plate and measured the velocity profile near the trailing edge and the far field noise. These measurements are shown in Fig. 4.28, where the fence height is shown with the horizontal dashed line. Two common characteristics were observed in the measured data. For all fence cases, there was a velocity deficit below the fence height (see Fig. 4.28 (a)), and a shear layer near the top of the fences, characterized by a sharp gradient in the velocity (see Fig. 4.28 (b)). As shown in Fig. 4.28 (c), Millican [11] found that the largest farfield noise reductions came from the case that had the largest velocity deficit and shear layer (velocity gradient) near the top of the fences. Afshari *et al.* [9] performed a similar experiment as Millican [11] and also observed a velocity deficit and shear layer near the top of the fences (although not discussed in detail) with corresponding high-frequency surface pressure spectra reductions downstream of the finlets. Therefore, these experiments suggest that the velocity deficit and shear layer at the top of the fences plays an important role in noise reduction. Bodling *et al.* [10] showed that the turbulence kinetic energy (TKE) reductions near the airfoil surface, due to the separation distance between the energetic turbulent eddies and the airfoil trailing (scattering) edge, also plays an important role in noise reduction.

To better understand how the velocity profile, shear layer and TKE distribution affects the unsteady surface pressure (the source of TE noise), an additional LES is performed with the taller fence case from Bodling *et al.* [10] using double the original fence spacing. Fig. 4.29 compares the baseline

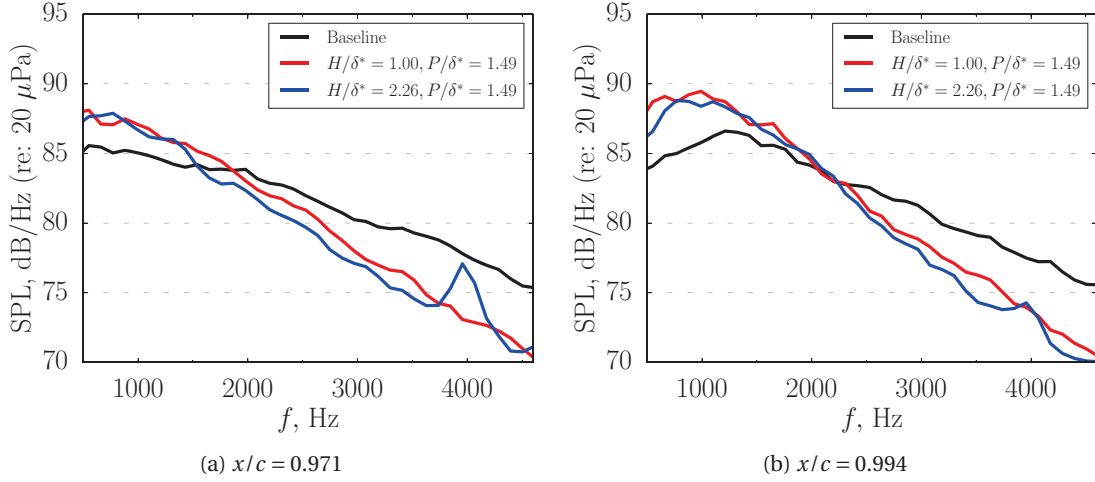


Figure 4.26: Comparison of the NACA 0012 baseline and fence surface pressure spectra at a) $x/c = 0.971$ and b) $x/c = 0.994$. Predictions are from Bodling *et al.* [10].

and fence surface pressure spectra, velocity, z-vorticity, and TKE profiles close to the trailing edge. The ordinate in Fig. 4.29 (b-d) is the wall normal distance, normalized by $v/u_{\tau, \text{baseline}}$, where v is the kinematic viscosity of the fluid and $u_{\tau, \text{baseline}}$ is the wall friction velocity of the baseline simulation. As shown in Fig. 4.29 (b), velocity deficit below the maximum height is observed with all fences. Comparing the trends in Figs. 4.29 (a) and (b), larger velocity deficit corresponds with more reductions in the surface pressure spectra. With all fence cases, there is also a sharp velocity gradient near the top of the fences, similar to what was observed by Milican [11]. To quantify the strength of the shear layer, we can calculate the span-averaged z-vorticity. Comparison of the baseline and fence z-vorticity is shown in Fig. 4.29 (c). The shear layer is weakest with the larger fence spacing, which comparing to Fig. 4.29 (a), has the least amount of surface pressure spectra reductions. The shear layer above the tall fence is farther away from the airfoil than the short fence, which has more reductions in the surface pressure spectra. The span-averaged TKE k/U_∞^2 profiles are shown in Fig. 4.29 (d). Comparing the trends in Fig 4.29 (a) and (d), more reductions in TKE near the airfoil surface correspond with more reductions in the high frequency surface pressure spectra. Also, similar to the shear layer analysis, larger distance between the peak TKE and airfoil leads to more reductions in the surface pressure spectra.

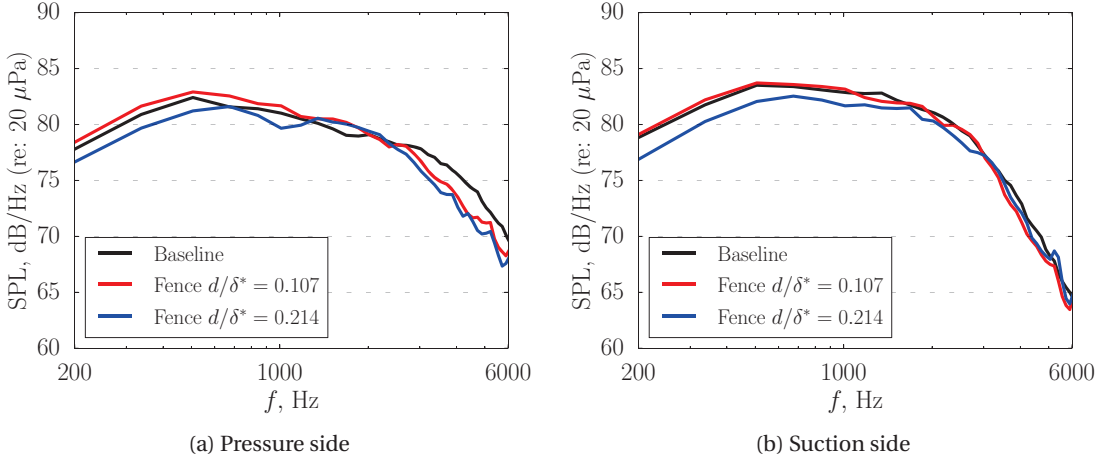


Figure 4.27: Comparison of the baseline and fence surface pressure spectra at $x/c = 0.994$ on the (a) pressure side and (b) suction side.

In light of these conclusions, we will now compare the suction side of the DU96-W-180 airfoil with the NACA 0012 results. Figure 4.30 contrasts the velocity profiles of the NACA 0012 and suction side of the DU96-W-180 close to the trailing edge at $x/c = 0.994$. For the suction side of the DU96-W-180, there is an increase in velocity near the airfoil surface, which does not occur with the NACA 0012. This may be one of the reasons that there are no reductions in the surface pressure spectra close to the trailing edge. Figure 4.31 contrasts the z-vorticity profiles of the NACA 0012 and suction side of the DU96-W-180 close to the trailing edge at $x/c = 0.994$. The NACA 0012 shows two different fence spacings. For the fence applied to the NACA 0012 that has smaller fence spacing, the peak z-vorticity (strength of the shear layer) is larger than with the DU96-W-180. The fence that has a larger fence spacing (which still had reductions in the surface pressure spectra) has a peak z-vorticity and wall normal distance that is about the same as the DU96-W-180. Since the fence with the larger fence spacing still had reductions in the surface pressure spectra, the effect of the location and magnitude of the peak z-vorticity is not conclusive.

We previously showed that in the current predictions the pressure side had reductions in the surface pressure spectra close to the trailing edge, while the suction side did not. Therefore, we will now compare the two sides of the DU96-W-180 airfoil to see how the velocity and TKE profiles differ. Figure 4.32 compares the baseline and fence velocity profile on the pressure and suction of the DU96-W-180 airfoil close to the trailing edge at $x/c = 0.994$. On *both* sides, there is an increase in

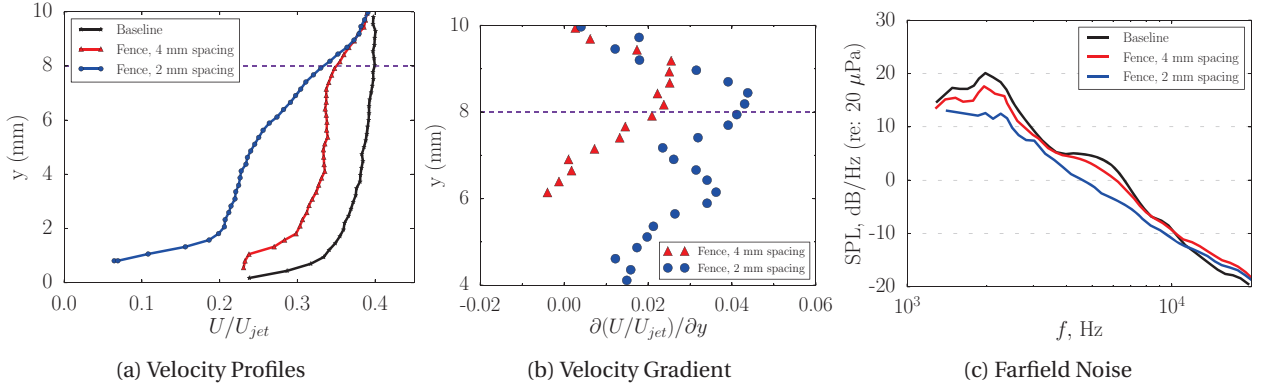


Figure 4.28: Measured profiles of (a) velocity, (b) velocity gradient and (c) farfield noise from the flat plate experiment by Millican [11]. The profiles are measured at the trailing edge of the flat plate. The horizontal dashed lines represent the maximum height of the fences.

velocity near the airfoil surface, which we have shown previously should lead to less reductions in the surface pressure spectra. However, we know that the pressure side still had reductions in the surface pressure spectra. Therefore, this tells us that the velocity deficit within the fence channels is not the sole determinate for noise reductions. Figure 4.33 compares the baseline and fence TKE profiles for the NACA 0012 and both sides of the DU96-W-180. As was shown previously, (repeated in Fig. 4.33 (a)), with the NACA 0012, larger separation distance between the peak TKE (source) and the airfoil surface (scattering body) results in larger TKE reductions near the airfoil surface. Comparing the pressure and suction side of the DU96-W-180 (Fig. 4.33 (b) and (c)), the peak TKE of the fences is displaced farther from the airfoil on the pressure side than the suction side. Since the baseline profiles of the pressure and suction side of the DU96-W-180 are different, the differences in the TKE reductions are not clear from viewing the entire boundary layer profile. However, if we zoom in to the near wall region we can better compare the TKE reductions. Figure 4.34 shows the TKE profile zoomed in to the near wall region. More TKE reductions are observed with the fences on the pressure side than the suction side. Figure 4.35 shows the corresponding vertical velocity fluctuation spectra near the wall. Commensurate with the TKE reductions, there is more reductions in the velocity fluctuations with the fences on the pressure side of the DU96-W-180 airfoil than the suction side. In addition, the suction side has much less TKE and velocity spectra reductions than what was observed with the small spacing fences applied to the NACA 0012 (see Fig. 4.34 (a) and Fig. 4.35 (a)).

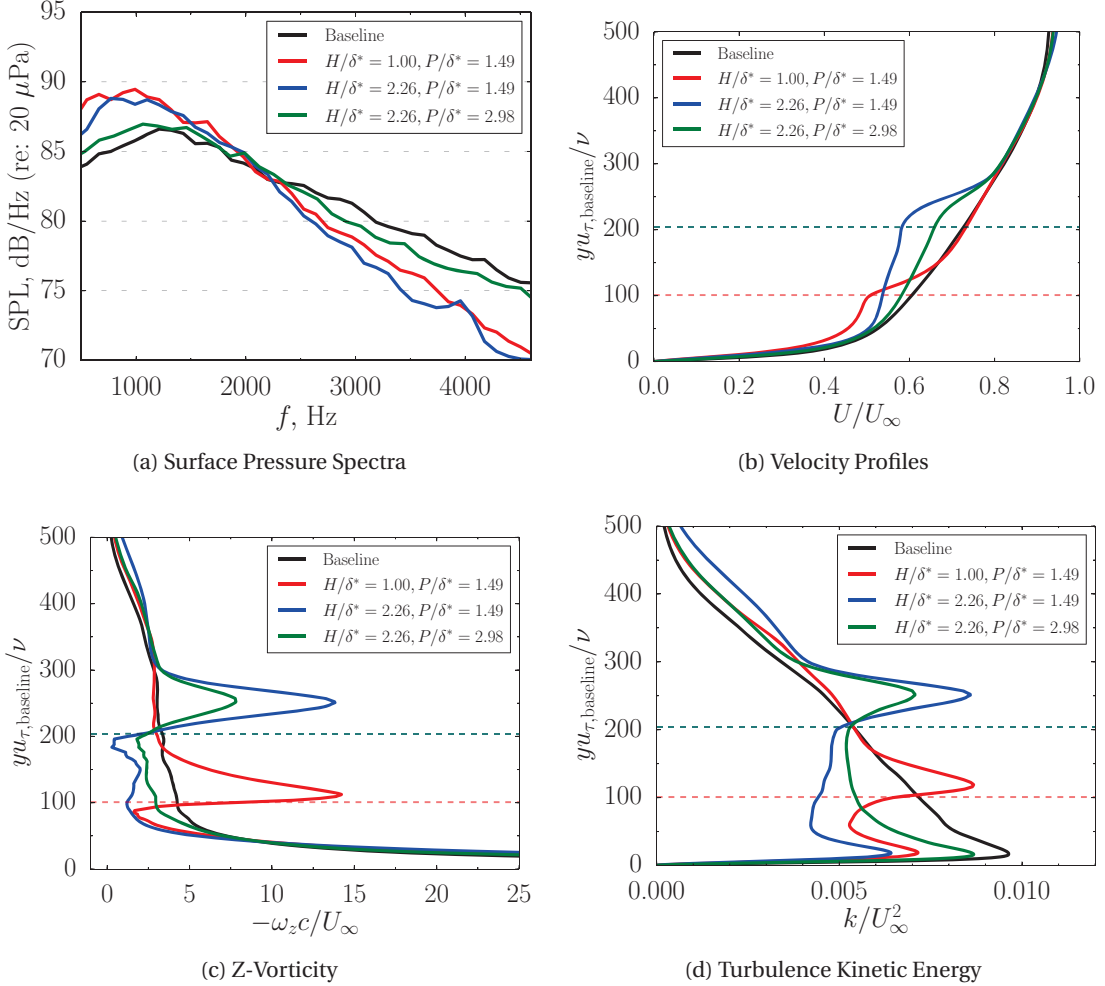


Figure 4.29: Comparison of the NACA 0012 baseline and fence span-averaged (a) surface pressure spectra, (b) wall normal velocity profiles and (c) z-vorticity and (d) k / U_{∞}^2 at $x/c = 0.994$. Predictions with $P/\delta^* = 1.49$ are from Bodling *et al.* [10].

Some important conclusions can be drawn from this analysis. This analysis has shown that the reductions in the surface pressure fluctuations *closest* to the trailing edge are ultimately what leads to farfield noise reductions. If the entire trailing edge does not have reductions in surface pressure fluctuations, as was the case with the suction side of the DU96-W-180, the fences may not be effective in reducing farfield noise. This analysis has also shown that as suggested by the measurements from Millican [11] and Afshari *et al.* [9], the velocity deficit indeed plays a role in reducing the surface pressure fluctuations. This analysis has also further supported the conclusions made by Bodling *et al.* [10] that an increase in the source-trailing edge separation distance leads to more TKE and pres-

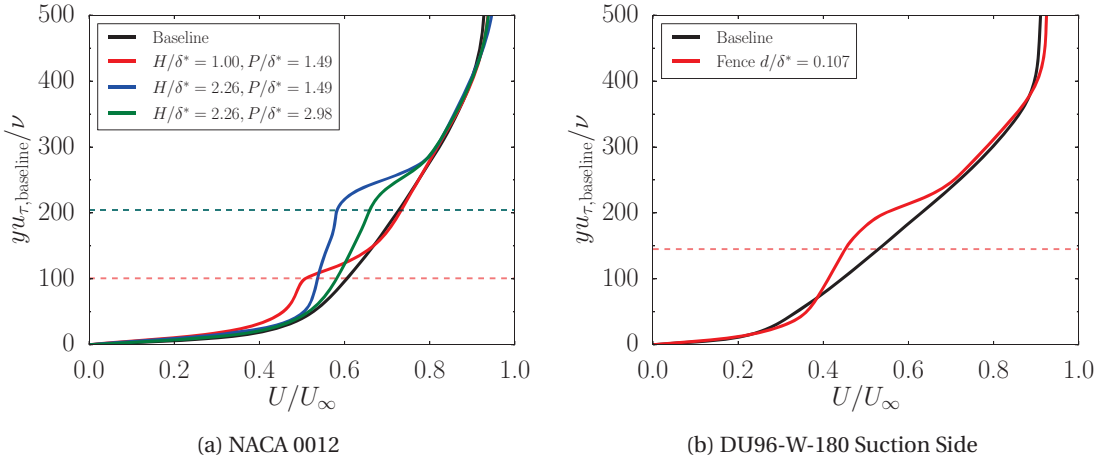


Figure 4.30: Comparison of the baseline and fence time- and span-averaged velocity distribution on the suction side of the (a) NACA 0012 and (b) DU96-W-180 close to the trailing edge at $x/c = 0.994$.

sure fluctuation reductions near the airfoil surface. Since the pressure side of the DU96-W-180 has a larger source-trailing edge separation distance than the suction side, there is more TKE and pressure fluctuation reductions near the airfoil surface. The analysis has also shown that the velocity deficit and source-trailing edge separation distance work in tandem to reduce the pressure fluctuations near the trailing edge. Although both the pressure and suction side has an increase in velocity near the airfoil surface, since the source-trailing edge separation distance on the pressure side is larger (or large enough), there are still reductions in the surface pressure fluctuations on the pressure side.

Differences in Farfield Noise of Thin/Thick Fences

This section seeks to explain why the thinner fence has less farfield noise than the thicker fence. One reason for the lower farfield noise levels of the thinner fence could be due to scattering at the top of the fences themselves. Figure 4.36 shows the surface pressure spectra at the top of the center fence surface (4th fence along span) at $x/c = 0.98$ for the pressure and suction sides. The SPL levels are much greater for the two fences compared to the baseline, regardless of which airfoil surface. Since the thinner fence would have less area to scatter noise from, the thinner fence should have less farfield noise than the thicker fence.

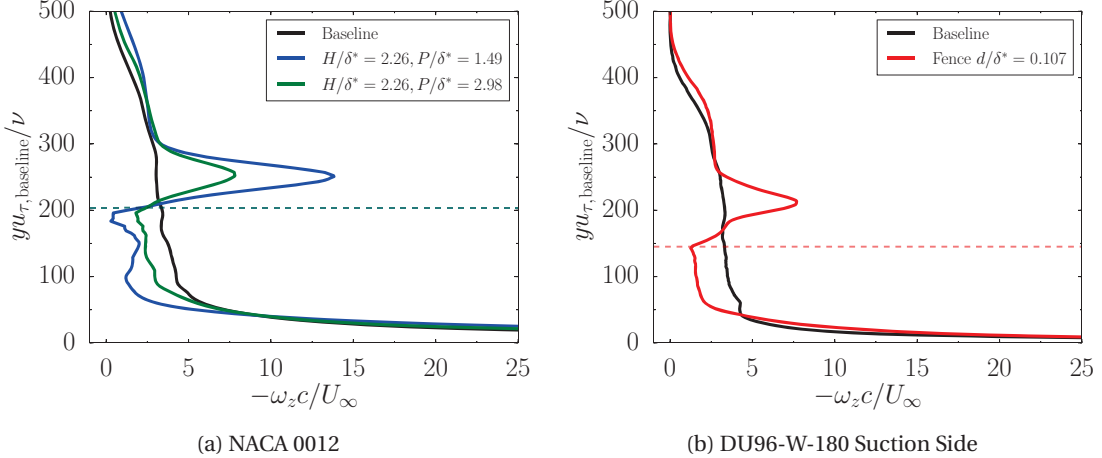


Figure 4.31: Comparison of the baseline and fence time- and span-averaged z-vorticity distribution on the suction side of the (a) NACA 0012 and (b) DU96-W-180.

4.5 Conclusions

This paper presents numerical investigations of airfoil geometries inspired by the down coat of the owl. The down coat is modeled using finlet fences proposed by Clark *et al.* [3]. Large eddy simulations are performed for the -0.2°AOA case for the baseline (DU96-W-180) airfoil and two airfoils with fences attached to the aft portion of the airfoil. To examine the effect of the fence thickness, two fences with nondimensional thicknesses, $d/\delta^* = 0.107$ and 0.214 , are investigated.

The aerodynamic analysis shows that the drag increase is due to the increased wetted surface area, which is in agreement with the measurements. The thicker fence has a greater drag increase than the thinner fence due to the higher skin friction in the fence region. The airfoil lift decreases slightly due to the fences, with a larger decrease observed with the thicker fence, which is also in agreement with the measurements. This analysis suggests that for optimal aerodynamic performance, the fences should be as thin as possible.

An in-house FW-H solver is used with the LES data to predict the farfield noise and evaluate the aeroacoustic performance of the fences. Except for some low frequency noise reduction with the thinner fence, both fences show increase of farfield noise.

The reason for the lack of noise reduction with the fences is investigated. On the suction side near the maximum fence height, there are reductions in the high-frequency surface pressure spec-

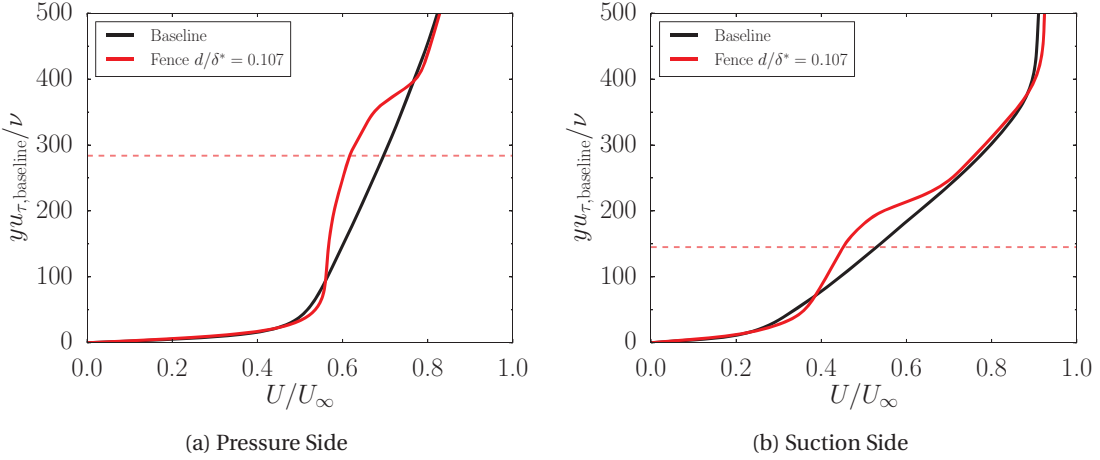


Figure 4.32: Comparison of the baseline and fence time- and span-averaged velocity distribution on the (a) pressure side and (b) suction side of the DU96-W-180 at $x/c = 0.994$.

tra. However, close to the trailing edge the simulations show no reductions in the high-frequency surface pressure spectra and therefore, no high-frequency farfield noise reduction is predicted. This shows that the reductions in the surface pressure fluctuations *closest* to the trailing edge are ultimately what leads to farfield noise reductions. If the entire trailing edge does not have reductions in surface pressure fluctuations, as was the case with the suction side of the DU96-W-180, the fences may not be effective in reducing farfield noise. A larger velocity deficit below the fence height is shown to correspond with more reductions in the surface pressure fluctuations at the trailing edge. This analysis has shown that as suggested by the measurements from Millican [11] and Afshari *et al.* [9], the velocity deficit indeed plays a role in reducing the surface pressure fluctuations. Analysis of the results also further supports the conclusions made by Bodling *et al.* [10] that an increase in the source-trailing edge separation distance leads to more TKE and pressure fluctuation reductions near the airfoil surface. Since the pressure side of the DU96-W-180 has a larger source-trailing edge separation distance than the suction side, there is more TKE and pressure fluctuation reductions near the airfoil surface. We have also shown that the velocity deficit and source-trailing edge separation distance work in tandem to reduce the pressure fluctuations near the trailing edge. Although both the pressure and suction side has an increase in velocity near the airfoil surface, since the source-trailing edge separation distance on the pressure side is larger (or large enough), there are still reductions in the surface pressure fluctuations on the pressure side.

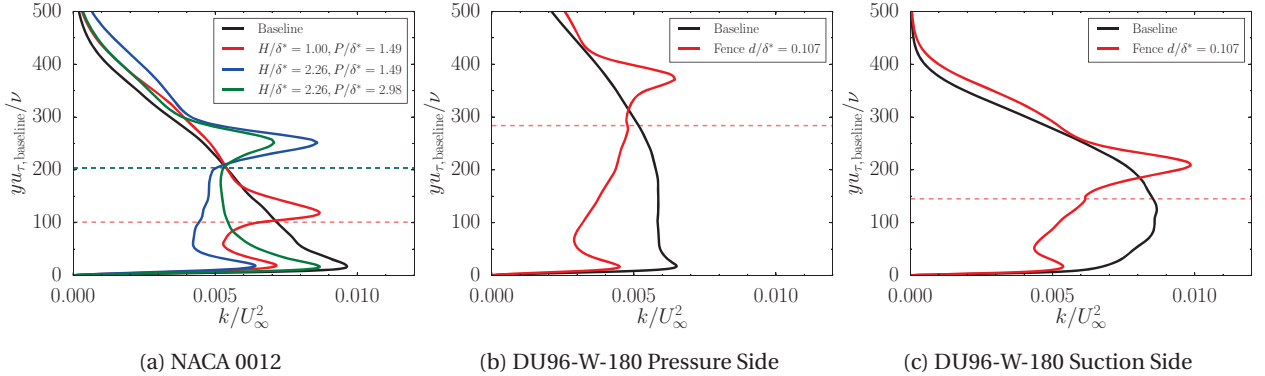


Figure 4.33: Comparison of the baseline and fence time- and span-averaged k/U_{∞}^2 distribution on the (a) NACA 0012, (b) DU96-W-180 pressure side and (c) DU96-W-180 suction side at $x/c = 0.994$.

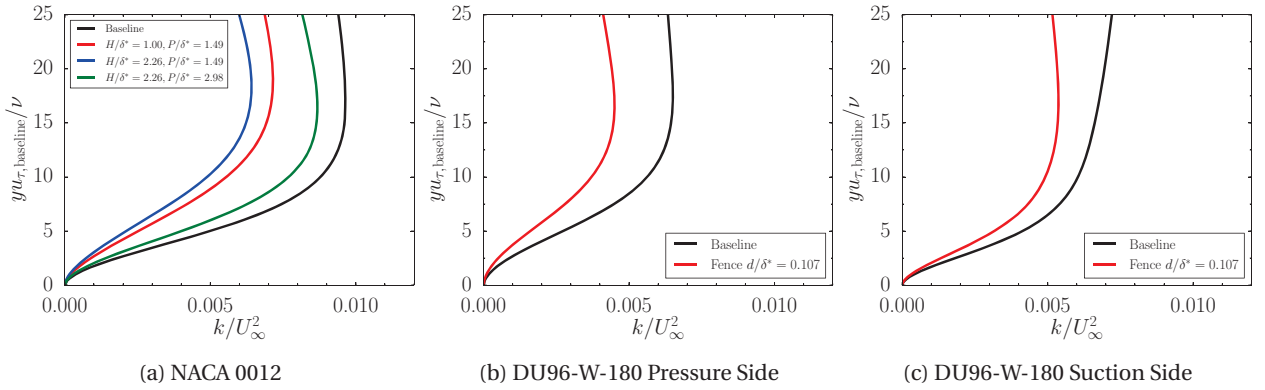


Figure 4.34: Comparison of the baseline and fence time- and span-averaged k/U_{∞}^2 distribution near the wall on the (a) NACA 0012, (b) DU96-W-180 pressure side and (c) DU96-W-180 suction side at $x/c = 0.994$.

The lower farfield noise levels of the thinner fence compared to the thicker fence is believed to be due to less scattering at the top of the fences themselves (less surface area at the top of the fences). Therefore, the thinner fence is found to be better than the thicker fence from both aerodynamic and aeroacoustic perspectives.

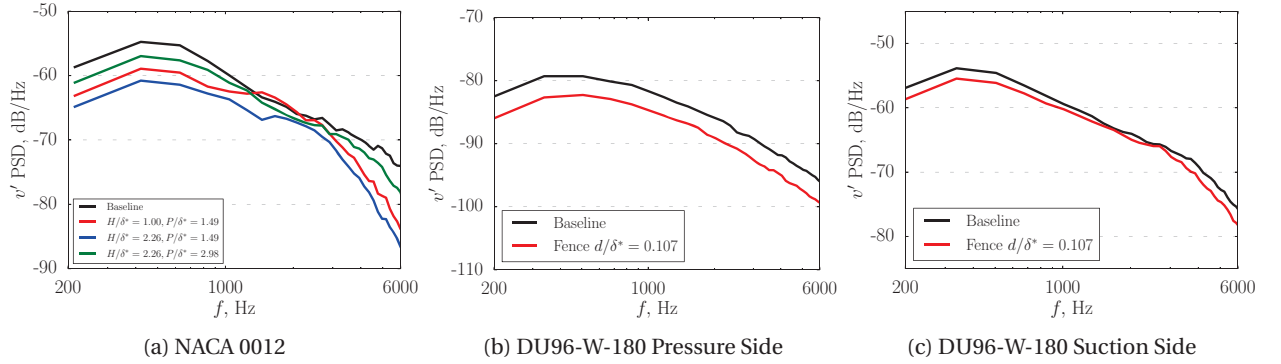


Figure 4.35: FDL3DI predicted vertical velocity fluctuation spectra for the (a) NACA 0012, (b) DU96-W-180 pressure side and (c) DU96-W-180 suction side at $x/c = 0.994$. Spectra is taken within the viscous sublayer ($y^+ = 0.5$). Predictions are averaged along the span with the points within the fences removed from the averaging procedure.

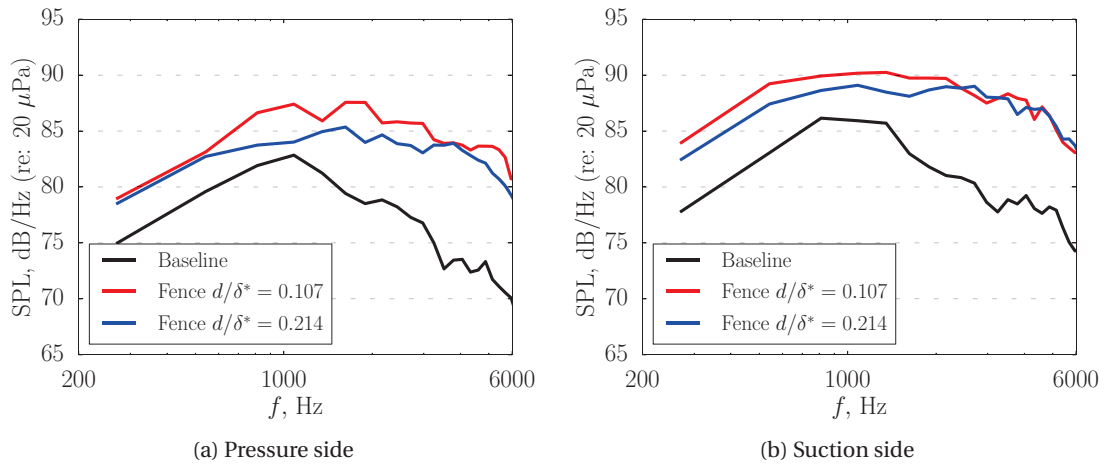


Figure 4.36: Comparison of the baseline and fence surface pressure spectra at the top of the middle fence (4th fence) at $x/c = 0.98$ on the (a) pressure side and (b) suction side.

CHAPTER 5. CONCLUSIONS AND FUTURE WORK

5.1 Conclusions

Chapter one introduces the motivation and theoretical background for bioinspired trailing edge noise reduction designs. The bioinspired finlet designs that are the focus of this dissertation are inspired by the down coat of the owl and were proposed by Clark *et al.* [3]. The two main noise reduction mechanism hypotheses for the finlet design are discussed, which is investigated in the rest of the dissertation using high-fidelity simulations. Although there have been many high-fidelity simulations done to model the leading edge combs and trailing edge fringes of owl wings, the high fidelity simulations performed in this dissertation to model the downy coat are the first of its kind.

In chapter two and three, wall-resolved large eddy simulations are performed for the baseline (NACA 0012) airfoil and two airfoils with fences attached to the aft portion of the airfoil. The NACA 0012 airfoil is first selected, instead of the DU96-W-180 that is used in the experiment, to reduce the computational complexity of the simulations. Two fences with different maximum nondimensional heights, $H/\delta^* = 1.0$ and 2.26, are investigated. All three models are simulated at chord-based Reynolds number, $Re_c = 5 \times 10^5$, flow Mach number, $M = 0.2$, and angle of attack, $\alpha = 0^\circ$ (zero-lift case). The boundary layer in the simulations is tripped with a geometry-resolved trip wire in order to compare with experiments that are at much higher Re_c (of the order of 2 M).

Comparisons with experimental data show good agreement for aerodynamic pressure coefficient (C_p) and skin friction coefficient distributions (C_f) for the baseline airfoil. The time-averaged wall-normal velocity and Reynolds stresses for the baseline airfoil also agree well with experimental and direct numerical simulations (DNS) data.

The aerodynamic analysis shows that the drag increase due to the fences is small and is due to the increased wetted surface area. The skin friction coefficient on the airfoil surface reduces because of the fences and hence the drag increase is smaller than the increase in the wetted surface area.

An in-house FW-H solver is used with the LES data to predict the farfield noise and evaluate the aeroacoustic performance of the fences. Compared to the baseline, the $H/\delta^* = 1.0$ fence reduces the farfield SPL by up to 10 dB for frequencies between 500 Hz and 5 kHz. Noise reduction with the taller fence ($H/\delta^* = 2.26$) is limited to frequencies above 1.5 kHz. Larger noise reduction is observed with the taller fence for frequencies greater than 2 kHz.

Two noise reduction mechanisms are identified: 1) the fences increase the source-scattering edge separation distance rendering the scattering process inefficient, particularly for high-frequency noise, and 2) the fences reduce the spanwise coherence (γ^2) in the boundary layer for separation distances greater than the fence pitch, which is more effective at reducing low-frequency farfield noise.

The first mechanism of noise reduction is verified by examining the TKE near the airfoil trailing edge and the unsteady surface pressure spectra. The fences reduce the TKE near the airfoil (scattering) surface; peak TKE shifts to just above the fence height. The reduced TKE near the surface leads to reduced unsteady surface pressure, which is observed in the simulations and previous measurements. The taller fence gives greater reductions in near-surface TKE, surface pressure PSD, and farfield noise for frequencies greater than 2 kHz.

Spanwise coherence of the unsteady surface pressure near the trailing edge is computed and compared between the baseline and the two fence simulations. Both fences reduce γ^2 at low frequencies for normalized separation distances $\Delta z/c > P/c$. For these frequencies, both fences increase γ^2 in fence passages (i.e., for $\Delta z/c < P/c$) due to a “channeling” effect from adjacent fence sidewalls. This increase is larger for the taller fence. The taller fence is louder than the shorter fence (but not the baseline) for low frequencies. This is hypothesized to be due to (a) increased γ^2 within fence passages, and (b) additional noise radiated by the leading edge of the taller fence as it is less aligned with the oncoming turbulence in the flow.

An additional fence configuration, which was designed to reach the final height in one single “step”, was tested. The lack of farfield noise reduction from this design demonstrates the importance of having a fence leading edge that is highly skewed to the incoming flow.

In chapter four, the finlets are then applied to a DU96-W-180 baseline airfoil at a lift condition to allow better comparisons with the experimental data and to better understand the noise reduction mechanisms at conditions more applicable to aerospace and wind turbine applications. To examine the effect of the fence thickness, two fences with nondimensional thicknesses, $d/\delta^* = 0.107$ and 0.214 are investigated. Wall-resolved large eddy simulations are performed at chord-based Reynolds number, $Re_c = 6 \times 10^5$, flow Mach number, $M = 0.146$, and angle of attack, $\alpha = -0.2^\circ$. The aerodynamic analysis shows that the drag increase is due to the increased wetted surface area, which is in agreement with the measurements. The thicker fence has a greater drag increase than the thinner fence due to the higher skin friction in the fence region. The airfoil lift decreases slightly due to the fences, with a larger decrease observed with the thicker fence, which is also in agreement with the measurements. This analysis suggests that for optimal aerodynamic performance, the fences should be as thin as possible.

An in-house FW-H solver is used with the LES data to predict the farfield noise and evaluate the aeroacoustic performance of the fences. Except for some low frequency noise reduction with the thinner fence, both fences show increase of farfield noise.

The reason for the lack of noise reduction with the fences is investigated. On the suction side near the maximum fence height, there are reductions in the high-frequency surface pressure spectra. However, close to the trailing edge the simulations show no reductions in the high-frequency surface pressure spectra and therefore, no high-frequency farfield noise reduction is predicted. This shows that the reductions in the surface pressure fluctuations *closest* to the trailing edge are ultimately what leads to farfield noise reductions. If the entire trailing edge does not have reductions in surface pressure fluctuations, as was the case with the suction side of the DU96-W-180, the fences may not be effective in reducing farfield noise. A larger velocity deficit below the fence height is shown to correspond with more reductions in the surface pressure fluctuations at the trailing edge. This analysis has shown that as suggested by the measurements from Millican [11] and Afshari *et al.* [9], the velocity deficit indeed plays a role in reducing the surface pressure fluctuations. Analysis

of the results also further supports the conclusions made by Bodling *et al.* [10] that an increase in the source-trailing edge separation distance leads to more TKE and pressure fluctuation reductions near the airfoil surface. Since the pressure side of the DU96-W-180 has a larger source-trailing edge separation distance than the suction side, there is more TKE and pressure fluctuation reductions near the airfoil surface. We have also shown that the velocity deficit and source-trailing edge separation distance work in tandem to reduce the pressure fluctuations near the trailing edge. Although both the pressure and suction side has an increase in velocity near the airfoil surface, since the source-trailing edge separation distance on the pressure side is larger (or large enough), there are still reductions in the surface pressure fluctuations on the pressure side. Furthermore, the lower farfield noise levels of the thinner fence compared to the thicker fence is believed to be due to less scattering at the top of the fences themselves (less surface area at the top of the fences). Therefore, the thinner fence is found to be better than the thicker fence from both aerodynamic and aeroacoustic perspectives.

5.2 Future Work

The work presented in this dissertation lays the path forward for future computational studies on finlets. The simulations performed on the DU96-W-180 airfoil has opened up many interesting questions to be answered. It will be interesting to see if increasing the fence height, perhaps even on only the suction side, would result in reductions in the surface pressure fluctuations on the suction side, and therefore, farfield noise reductions. Alternately, it would be interesting to see if the spacing of the fences is decreased enough, would there no longer be a velocity increase near the airfoil surface, and therefore, there would be farfield noise reductions.

It was not conclusive what role the shear layer at the top of the finlet fences had, if any, on noise reduction. Millican [11] hypothesized that the fences are reducing the farfield noise by a mechanism called shear sheltering [69]. Millican [11] hypothesized that the shear layer at the fence height reduces the influence of the disturbances (turbulence above the fence height) from penetrating through to the aft surface and causing unsteady surface pressure. Much more analysis is needed to verify this hypothesis.

One numerical experiment that could be performed is placing a single-harmonic source term above the fences and seeing how/if the fences shield the trailing edge from the perturbations emanating from the point source. Based off of the shear sheltering hypothesis, compared to the baseline, one would expect a smaller surface pressure spectra peak frequency to occur with the fences. Different frequencies could be used for the source term to see if the fences shield only certain ranges of frequencies.

Another approach that could be used is applying the Mean Flow Perturbation (MFP) method [70] to the base flow of the baseline and fence simulations. The MFP technique is a linear stability analysis that can be used to understand the receptivity of base flows to a small perturbation [70]. The MFP method, in conjunction with the dynamic mode decomposition (DMD) analysis, is used to find relevant instability modes, their growth rates and associated frequencies [70]. This technique can be used to see how a perturbation evolves within the fence region. By analyzing the decay rates of the different DMD modes, it may be found that the fences cause certain frequency modes to decay more than others, thereby shielding those frequency modes from scattering at the trailing edge.

The finlet rails are another area of research that should be explored. Based off of the experiments, they appear to manipulate the boundary layer turbulence differently than the finlet fences. For example, increasing the finlet rail height has the opposite effect on farfield noise than the finlet fences. Therefore, more insight into the noise reduction mechanisms of the finlet rails will be important for developing a comprehensive understanding of how the boundary layer turbulence can be manipulated to reduce trailing edge noise.

Furthermore, it will be useful to understand how effective the finlets are at reducing farfield noise when combined with other noise reduction designs such as trailing edge serrations. Since these designs are known to reduce noise by distinctly different mechanisms, it will be interesting to see what their net effect is on the farfield noise.

Finally, more research needs to be done to understand how we can minimize the adverse impact on the aerodynamic performance of the airfoil due to finlets. Perhaps completely different designs, that do not resemble the current finlet design but still maintain the same noise reduction mechanisms, can be created that improve the aerodynamic performance of the finlets.

BIBLIOGRAPHY

- [1] Ian A. Clark. *Bio-Inspired Control of Roughness and Trailing Edge Noise*. PhD thesis, Virginia Polytechnic Institute and State University, 2017.
- [2] Richard A. Kroeger, Heinz D. Grushka, and Tibor C. Helvey. Low speed aerodynamics for ultra-quiet flight. Technical report, Wright-Patterson Air Force Base, 1972.
- [3] Ian A. Clark, William Devenport, Justin W. Jaworski, Conor Daly, Nigel Peake, and Stewart Glegg. Noise generating and suppressing characteristics of bio-inspired rough surfaces. In *20th AIAA/CEAS Aeroacoustics Meeting*. American Institute of Aeronautics and Astronautics, 2014.
- [4] Ian A. Clark, Nathan W. Alexander, William Devenport, Stewart Glegg, Justin W. Jaworski, Conor Daly, and Nigel Peake. Bioinspired trailing-edge noise control. *AIAA Journal*, 55(3):740–754, 2017.
- [5] H. Lee and S. H. Kang. Flow characteristics of transitional boundary layers on an airfoil in wakes. *ASME Journal of Fluids Engineering*, 122:522–532, 2000.
- [6] PR Spalart and J. H. Watmuff. Experimental and numerical study of a turbulent boundary layer with pressure gradient. *Journal of Fluid Mechanics*, 249:337–371, 1993.
- [7] William R Wolf and Sanjiva K Lele. Trailing edge noise predictions using compressible les and acoustic analogy. In *17th AIAA/CEAS Aeroacoustics Conference*. American Institute of Aeronautics and Astronautics, 2011.
- [8] Ana G. Sagrado and Tom Hynes. Wall pressure sources near an airfoil trailing edge under turbulent boundary layers. *Journal of Fluids and Structures*, 30:3–34, 2012.

- [9] Abbas Afshari, Mahdi Azarpeyvand, Ali A. Dehghan, and Máté Szőke. Trailing edge noise reduction using novel surface treatments. In *22nd AIAA/CEAS Aeroacoustics Conference*. American Institute of Aeronautics and Astronautics, 2016.
- [10] Andrew Bodling and Anupam Sharma. Numerical investigation of low-noise airfoils inspired by the down coat of owls. *Bioinspiration and Biomimetics*, 14(1), 2018.
- [11] Anthony J. Millican. Bio-inspired trailing edge noise control: Acoustic and flow measurements. Master's thesis, Virginia Polytechnic Institute and State University, 2017.
- [12] E. A. M. Franssen, C. M. A. G. van Wiechen, N. J. D. Nagelkerke, and E. Lebret. Aircraft noise around a large international airport and its impact on general health and medication use. *Occup Environ Med*, 61(5):405–413, 2004.
- [13] S. Morrell, R. Taylor, and D. Lyle. A review of health effects of aircraft noise. *Australian and New Zealand Journal of Public Health*, 21(2):221–36, 1997.
- [14] A. Farboud, R. Crunkhorn, and A. Trinidade. 'wind turbine syndrome': fact or fiction? *JLaryngol Otol*, 127(3):222–226, 2013.
- [15] Ejia Pedersen and Kerstin Persson Waye. Perception and annoyance due to wind turbine noise—a dose-response relationship. *Journal of the Acoustical Society of America*, 116(6):3460–3470, 2004.
- [16] T. F. Brooks, D. S. Pope, and M. A. Marcolini. Airfoil self-noise and prediction. Technical Report NASA RP 1218, NASA Langley Research Center, 1989.
- [17] C. J. Doolan. A review of airfoil trailing edge noise and its prediction. *Acoustics Australia*, 36 (1-7), 2008.
- [18] D. P. Lockard and G. M. Lilley. The airframe noise reduction challenge. Technical Report NASA/TM-2004-213013, NASA Langley Research Center, 2004.
- [19] W. K. Blake. *Modelling and measurements of wakes in large wind farms*. Academic Press, 1986.

- [20] S. T. Chou and A. R. George. Effect of blunt trailing edge on rotor broadband noise. *AIAA Journal*, 24(8):1380–1382, 1986.
- [21] S. Oerlemans, P. Sijtsma, and B. Mendez Lopez. Location and quantification of noise sources on a wind turbine. *Journal of Sound and Vibration*, 299(4-5):869–883, 2007.
- [22] J. M. Benyus. *Biomimicry: Innovation inspired by nature*. William Morrow Paperbacks, 2002.
- [23] J. Korb. Thermoregulation and ventilation of termite mounds. *Naturwissenschaften*, 90(5):212–9, 2003. doi: 10.1007/s00114-002-0401-4.
- [24] A. Solga, Z. Cerman, B. F. Striffler, M. Spaeth, and W. Barthlott. The dream of staying clean: Lotus and biomimetic surfaces. *Bioinspir Biomim*, 2(4):S126–34, 2007. doi: 10.1088/1748-3182/2/4/S02.
- [25] Geoffrey M. Lilley. A study of the silent flight of the owl. In *4th AIAA/CEAS Aeroacoustics Conference*, volume 2340, pages 1–6. American Institute of Aeronautics and Astronautics, 1998.
- [26] R. R. Graham. The silent flight of owls. *Journal of the Royal Aeronautical Society*, 38:837–843, 1934.
- [27] Thomas Bachmann, S. Blazek, T. Erlinghagen, W. Baumgartner, and H. Wagner. *Barn Owl Flight*, pages 101–117. Springer, 2012. ISBN 3642283012.
- [28] Bharat Raj Agrawal and Anupam Sharma. Numerical investigations of bio-inspired blade designs to reduce broadband noise in aircraft engines and wind turbines. 2016 AIAA SciTech Meeting. American Institute of Aeronautics and Astronautics, 2016.
- [29] R. D. Sandberg and L. E. Jones. Direct numerical simulations of low reynolds number flow over airfoils with trailing-edge serrations. *Journal of Sound and Vibration*, 330(16):3818–3831, 2011.
- [30] Michel Roger, Christophe Schram, and Leandro De Santana. Reduction of airfoil turbulence-impingement noise by means of leading-edge serrations and/or porous material. In *19th AIAA/CEAS Aeroacoustics Conference*. American Institute of Aeronautics and Astronautics, 2013.

- [31] Bharat Raj Agrawal and Anupam Sharma. Numerical analysis of aerodynamic noise mitigation via leading edge serrations for a rod-airfoil configuration. *International Journal of Aeroacoustics*, 15(8):734–756, 2016.
- [32] Stefan Oerlemans, Murray Fisher, Thierry Maeder, and Klaus Kögler. Reduction of wind turbine noise using optimized airfoils and trailing-edge serrations. *AIAA Journal*, 47(6):1470–1481, 2009.
- [33] T. Geyer, E. Sarradj, and C. Fritzsche. Measurement of the noise generation at the trailing edge of porous airfoils. *Experiments in Fluids*, 48(2):291–308, 2010.
- [34] Justin W. Jaworski and N. Peake. Aerodynamic noise from a poroelastic edge with implications for the silent flight of owls. *Journal of Fluid Mechanics*, 723:456–479, 2013.
- [35] Justin W. Jaworski and N. Peake. Parametric guidance for turbulent noise reduction from poroelastic trailing edges and owls. In *19th AIAA/CEAS Aeroacoustics Conference*. American Institute of Aeronautics and Astronautics, 2013.
- [36] John Finnigan. Turbulence in plant canopies. *Annual Review of Fluid Mechanics*, 32(1):519–571, 2000.
- [37] M. J. Lighthill. On sound generated aerodynamically. i. general theory. *Proceedings of The Royal Society A Mathematical Physical and Engineering Sciences*, 211(1107):564–587, 1952.
- [38] JE Ffowcs Williams and LH Hall. Aerodynamic sound generation by turbulent flow in the vicinity of a scattering half plane. *Journal of fluid mechanics*, 40(4):657–670, 1970.
- [39] N. Curle. The influence of solid boundaries upon aerodynamic sound. *Proceedings of The Royal Society A Mathematical Physical and Engineering Sciences*, 231(1187):505–514, 1955.
- [40] R. K. Amiet. Noise due to turbulent flow past a trailing edge. *Journal of Sound and Vibration*, 47(3):387–393, 1976.
- [41] Andrew Bodling and Anupam Sharma. Numerical investigation of noise reduction mechanisms in a bio-inspired airfoil. *Journal of Sound and Vibration*, 453:314–327, 2019.

- [42] André V. Cavalieri, William R. Wolf, and Justin Jaworski. Acoustic scattering by finite poroelastic plates. In *20th AIAA/CEAS Aeroacoustics Conference*, AIAA Aviation. American Institute of Aeronautics and Astronautics, 2014.
- [43] Robert Dougherty. Extensions of DAMAS and benefits and limitations of deconvolution in beamforming. In *11th AIAA/CEAS aeroacoustics conference*, page 2961, 2005.
- [44] Andrew Bodling, Bharat Raj Agrawal, Anupam Sharma, Ian A. Clark, Nathan W. Alexander, and William Devenport. Numerical investigations of bio-inspired blade designs to reduce broadband noise in aircraft engines and wind turbines. In *55th AIAA Aerospace Sciences Meeting*. American Institute of Aeronautics and Astronautics, 2017.
- [45] Andrew Bodling, Bharat Raj Agrawal, Anupam Sharma, Ian A. Clark, Nathan W. Alexander, and William Devenport. Numerical investigation of bio-inspired blade designs at high reynolds numbers for ultra-quiet aircraft and wind turbines. In *23rd AIAA/CEAS Aeroacoustics Conference*. American Institute of Aeronautics and Astronautics, 2017.
- [46] R. Miguel Visbal and V. Datta Gaitonde. On the use of higher-order finite-difference schemes on curvilinear and deforming meshes. *Journal of Computational Physics*, 181(1):155–185, 2002.
- [47] J. E. Ffowcs Williams and David L. Hawking. Sound generation by turbulence and surfaces in arbitrary motion. *Philosophical Transactions of the Royal Society of London. Series A, Mathematical and Physical Sciences*, 264(1151):321–342, 1969.
- [48] A. Sharma and H. Chen. Prediction of aerodynamic tonal noise from open rotors. *Journal of Sound and Vibration*, 332(6), 2013.
- [49] R. Miguel Visbal. Numerical exploration of flow control for delay of dynamic stall on a pitching airfoil. 32nd AIAA Applied Aerodynamics Conference. American Institute of Aeronautics and Astronautics, 2014.
- [50] N. J. Georgiadis, D. P. Rizetta, and C. Fureby. Large-eddy simulation: Current capabilities, recommended practices and future research. *AIAA Journal*, 48(8):1772–1784, 2010.

- [51] H. Choi and P. Moin. Effects of the computational time step on numerical solutions of turbulent flow. *Journal of Computational Physics*, 113:1–4, 1994.
- [52] E. Norman Suhs, E. Stuart Rogers, and E. William Dietz. Pegasus 5: An automated pre-processor for overset-grid CFD. In *32nd AIAA fluid dynamics conference*. American Institute of Aeronautics and Astronautics, 2002.
- [53] Mark Drela. Xfoil: An analysis and design system for low reynolds number airfoils. In *Low Reynolds number aerodynamics*, pages 1–12. Springer, 1989.
- [54] N. Gregory and C. L. O'Reilly. Low-speed aerodynamic characteristics of naca 0012 aerofoil section, including the effects of upper-surface roughness simulating hoar frost. Technical Report NASA Reports and Memoranda 3726, 1970.
- [55] Peter Welch. The use of fast fourier transform for the estimation of power spectra: a method based on time averaging over short, modified periodograms. *IEEE Transactions on audio and electroacoustics*, 15(2):70–73, 1967.
- [56] Chisachi Kato and Masahiro Ikegawa. Large eddy simulation of unsteady turbulent wake of a circular cylinder using the finite element method. In *Advances in Numerical Simulation of Turbulent Flows*, volume 1, pages 49–56, 1991.
- [57] Abbas Afshari, Mahdi Azarpeyvand, Ali A. Dehghan, and Máté Szőke. Effects of streamwise surface treatments on trailing edge noise reduction. In *23rd AIAA/CEAS Aeroacoustics Conference*. American Institute of Aeronautics and Astronautics, 2017.
- [58] M. S. Howe. A review of the theory of trailing edge noise. *Journal of Sound and Vibration*, 61(3):437–465, 1978.
- [59] W. K. Blake. *Mechanics of Flow-Induced Sound and Vibration*, volume 17. 1986.
- [60] Richard M. Beam and R. F. Warming. An implicit finite-difference algorithm for hyperbolic systems in conservation-law form. *Journal of Computational Physics*, 22(1):87–110, 1976.
- [61] Richard M. Beam and R. F. Warming. An implicit factored scheme for the compressible navier-stokes equations. *AIAA Journal*, 16(4):393–402, 1978.

- [62] S. P. Gravante, A. M. Naguib, C. E. Wark, and H. M. Nagib. Characterization of the pressure fluctuations under a fully developed turbulent boundary layer. *AIAA Journal*, 36(10):1808–1816, 1998.
- [63] Hassan M. Nagib and Kapil A. Chauhan. Variations of von kármán coefficient in canonical flows. *Physics of Fluids*, 20(10):101518, 2008. doi: 10.1063/1.3006423. URL <https://doi.org/10.1063/1.3006423>.
- [64] William R Wolf, J. L. F. Azevedo, and Sanjiva K Lele. Convective effects and the role of quadrupole sources for aerofoil aeroacoustics. *Journal of Fluid Mechanics*, 708:502–538, 2012.
- [65] J. E. Williams and L. H. Hall. Aerodynamic sound generation by turbulent flow in the vicinity of a scattering half plane. *Journal of Fluid Mechanics*, 40(04):657–670, 1970.
- [66] R. K. Amiet. Acoustic radiation from an airfoil in a turbulent stream. *Journal of Sound and Vibration*, 41(4):407–420, 1975.
- [67] Andrew Bodling. Numerical investigations of bio-inspired blade designs to reduce broadband noise in aircraft engines and wind turbines. Master's thesis, Iowa State University, 2017.
- [68] Ian A. Clark, David Baker, Nathan W. Alexander, William Devenport, Nigel Peake, Stewart Glegg, and Justin W. Jaworski. Experimental and theoretical analysis of bio-inspired trailing edge noise control devices. In *22nd AIAA/CEAS Aeroacoustics Conference*. American Institute of Aeronautics and Astronautics, 2016.
- [69] J. C. R. Hunt and P. A. Durbin. Perturbed vortical layers and shear sheltering. *Fluid Dynamics Research*, 24(6):375–404, 1999.
- [70] Rajesh Ranjan, S Unnikrishnan, and Datta V. Gaitonde. On the use of mean flow perturbation for global stability analysis. In *Fluid Dynamics Conference*. American Institute of Aeronautics and Astronautics, 06 2018. doi: 10.2514/6.2018-3378.
- [71] D. V. Gaitonde and M. R. Visbal. High-order schemes for navier stokes equations: Algorithm and implementation into fdl3di. Technical Report AFRL-VA-WP-TR-1998-3060, Air Force Research Laboratory, 1998.

ACKNOWLEDGEMENTS

I would like to take this opportunity to express my thanks to those who helped me with various aspects of conducting research and the writing of this dissertation. First and foremost, I would like to thank my adviser, Dr. Anupam Sharma, for being an outstanding adviser. I have learned so much over the past three and a half years while working under your guidance. I could always count on your guidance any time of the day. You made getting a PhD enjoyable. You always embraced questions and made learning fun. I not only learned about aeroacoustics and CFD from you, I also learned how to think critically, use good engineering judgement and do research independently.

I would also like to thank my Ph.D. committee members Dr. Rothmayer, Dr. Leifsson, Dr. Pasalacqua, and Dr. Sarkar for your helpful feedback during my oral exams.

While working as a pathways intern at the Air Force Research Laboratory (AFRL), I learned a great deal from the researchers there. In particular, I would like to thank Dr. Miguel Visbal, Dr. Daniel Garmann, Dr. Caleb Barnes, Dr. Donald Rizetta, and Dr. Stuart Benton for really helping me learn about their CFD code FDL3DI. Because of all your insightful discussions, I have gained a deep understanding of high-fidelity simulations.

I would also like to thank my fellow research staff at Iowa State University including Dr. Aaron Rosenberg, Suganthi, Ang Li, Xingeng Wu, Bharat Agrawal and Sarasija Sudharsan for all of your feedback during our group meetings.

This research was funded by the National Science Foundation under grant number NSF/ CBET-1554196 and the Iowa Space Grants Consortium (Grant #475-20-5). Computational resources used for this research are provided by NSF XSEDE (Grant # TG-CTS130004) and the Argonne Leadership Computing Facility, which is a DOE Office of Science User Facility supported under Contract DE-AC02-06CH11357.

APPENDIX A. HIGH ORDER FILTERING AND COMPACT FINITE DIFFERENCING IN **FDL3DI**

A.1 Theory and Implementation of Filtering Schemes

A.1.1 Spectral Function of the Interior Filters

The FDL3DI code uses a low pass filter to remove the energy in the sub-grid scales. For the interior nodes, it uses the following stencil,

$$\alpha_f \hat{\phi}_{i-1} + \hat{\phi}_i + \alpha_f \hat{\phi}_{i+1} = \sum_{n=0}^N \frac{a_n(\phi_{i-n} + \phi_{i+n})}{2}, \quad (\text{A.1})$$

where α_f is the free parameter that provides some control on the "degree" of filtering, ϕ is the solution before filtering, $\hat{\phi}$ is the filtered solution, a_n is the set of coefficients for a given order of accuracy filter and $2N$ is the order of accuracy of the filter which has a stencil of $2N + 1$ points. In practice, $0.3 < \alpha_f < 0.5$ and for a low quality mesh $\alpha_f \approx 0.1$. To get the spectral function, the following Fourier transform identity relating the shift in the spatial domain to the shift in the frequency domain is used:

$$F\{f(x_i + m\Delta x)\} = F(w) e^{jwm\Delta x}, \quad (\text{A.2})$$

where m is the shift in the spatial domain and w is the reduced wave number defined as,

$$w = \frac{2\pi k}{N},$$

where k is the physical wave number, and N is the number of intervals. In applying the fourier transform identity in equation (A.2) to the stencil in equation (A.1), m is either $\pm n$ or ± 1 , $f(x_i)$ is

$\hat{\phi}_i$ and ϕ_i and for a computational domain, $\Delta x = 1$. Taking the Fourier transform of the stencil in equation (A.1) we get,

$$\alpha_f F_O(w)e^{-jw} + F_O(w) + \alpha_f F_O(w)e^{jw} = \frac{F_I(w)}{2} \sum_{n=0}^N a_n(e^{-jwn} + e^{jwn}).$$

Factoring out F_O in the left hand side we get,

$$F_O(w)[1 + \alpha_f(e^{-jw} + e^{jw})] = \frac{F_I(w)}{2} \sum_{n=0}^N a_n(e^{-jwn} + e^{jwn}). \quad (\text{A.3})$$

Now using the following identity,

$$2\cos(x) = e^{-jx} + e^{jx}, \quad (\text{A.4})$$

where $x = w$ on the left hand side, and $x = wn$ on the right hand side, this can be used in equation (A.3) to arrive at,

$$F_O(w)[1 + 2\alpha_f \cos(w)] = F_I(w) \sum_{n=0}^N a_n \cos(wn).$$

Using the definition of the spectral function

$$SF(w) = \frac{F_O(w)}{F_I(w)}, \quad (\text{A.5})$$

the spectral function becomes,

$$SF(w) = \frac{\sum_{n=0}^N a_n \cos(wn)}{1 + 2\alpha_f \cos(w)}. \quad (\text{A.6})$$

Because of the centered nature of the stencil in equation (A.1), $SF(w)$ is real and the filter is purely dissipative i.e., it alters only the magnitude of the input signal without introducing additional dispersion errors.

A.1.2 Derivation of the Coefficients of the Interior Filters

Equation (A.1) has $N + 2$ unknowns $\alpha_f, a_0, a_1, \dots, a_N$. To derive the coefficients, we first insist that the highest frequency mode be eliminated by enforcing $SF(\pi) = 0$. Imposing this on the spectral function eliminates any odd-even decoupling. Using this in equation (A.6) for $N = 2$ (4th order filter), the following equation results,

$$a_0 - a_1 + a_2 = 0. \quad (\text{A.7})$$

The remaining $N + 1$ additional equations are derived by using the filter stencil, equation (A.1), with $N = 2$, expanding ϕ and $\hat{\phi}$ about point "i" using a Taylor series, and then matching the Taylor series coefficients of equal order terms in the left and right sides. This results in,

$$\begin{aligned} \hat{\phi}_i(2\alpha_f + 1) + \hat{\phi}_i''\alpha_f\Delta x^2 + \hat{\phi}_i^{'''}\frac{2}{4!}\alpha_f\Delta x^4 + O(\Delta x^6) \\ = \phi_i(a_0 + a_1 + a_2) + \phi_i''\left(\frac{a_1}{2!} + \frac{2^2 a_2}{2!}\right)\Delta x^2 + \phi_i^{'''}\left(\frac{a_1}{4!} + \frac{2^4 a_2}{4!}\right)\Delta x^4 + O(\Delta x^6). \end{aligned}$$

We can achieve 4th order accuracy by neglecting $\Delta x \geq \Delta x^4$ terms. This results in,

$$\hat{\phi}_i(2\alpha_f + 1) + \hat{\phi}_i''\alpha_f\Delta x^2 = \phi_i(a_0 + a_1 + a_2) + \phi_i''\left(\frac{a_1}{2!} + \frac{2^2 a_2}{2!}\right)\Delta x^2.$$

Now matching the taylor series coefficients of equal order terms on the left and right hand side, we get the following N additional equations,

$$2\alpha_f + 1 = a_0 + a_1 + a_2 \quad (\text{A.8})$$

$$\alpha_f = \frac{a_1}{2} + 2a_2. \quad (\text{A.9})$$

These N additional equations above as well as equation (A.7) allow a_0, a_1, \dots, a_N to be solved in terms of the free parameter α_f . For a 4th order interior filter, $a_0 = \frac{5}{8} + \frac{3\alpha_f}{4}$, $a_1 = \frac{1}{2} + \alpha_f$, $a_2 = \frac{\alpha_f}{4} - \frac{1}{8}$. A table including interior filter coefficients for orders of accuracy 2, 4, 6, 8, and 10 can be found in Ref. [71].

A.1.3 Spectral Response of the Interior Filters

The ideal case for a filter is to have it attenuate the signal as least as possible so that the highest accuracy can be achieved. However there is some attenuation needed to remove the energy from the sub-grid scales and suppress any instabilities in the solution. Therefore, when choosing the correct filter for a problem, there is a balance between accuracy and stability.

The spectral responses of the interior filters are given in Figures A.1 – A.5. These figures give much insight into how the filter responds across all reduced wave numbers and α values given a step input. It is apparent that for a given value of α , as the order of the interior filter and/or α is increased, the filter attenuates the input signal less. Since there is only a real term in the spectral function, the response never causes any amplification of the input signal.

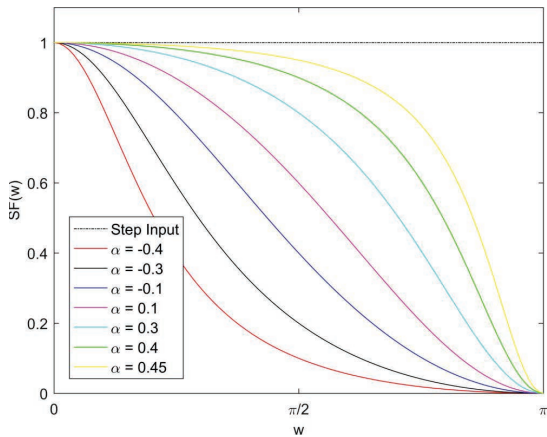


Figure A.1: 2nd Order Interior Filter

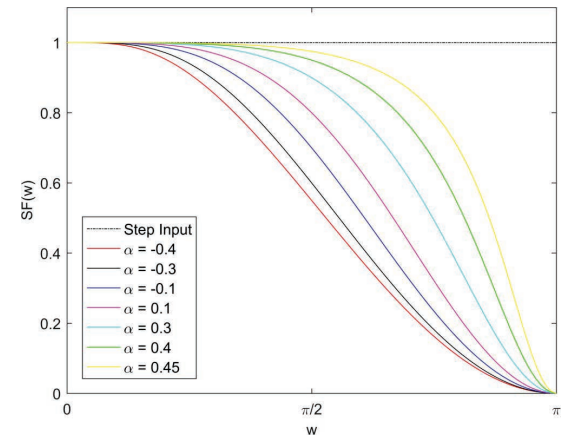


Figure A.2: 4th Order Interior Filter

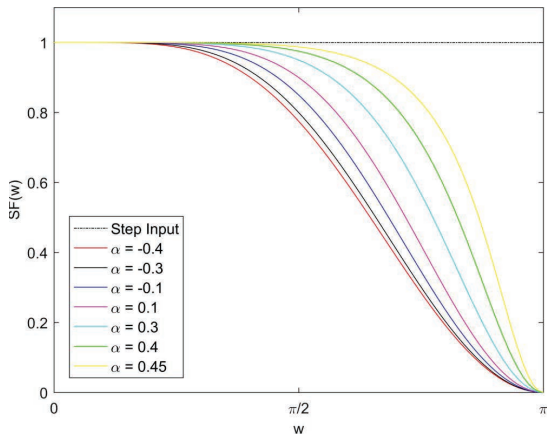


Figure A.3: 6th Order Interior Filter

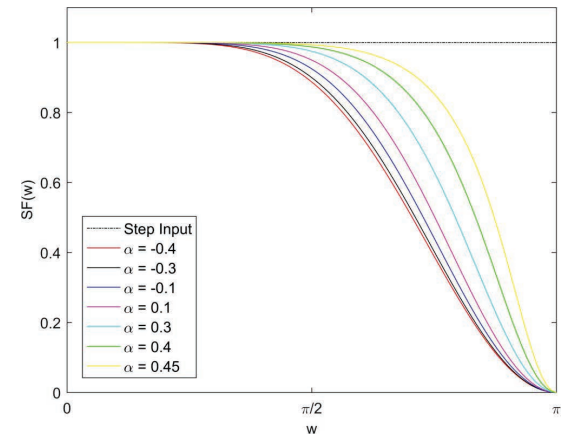


Figure A.4: 8th Order Interior Filter

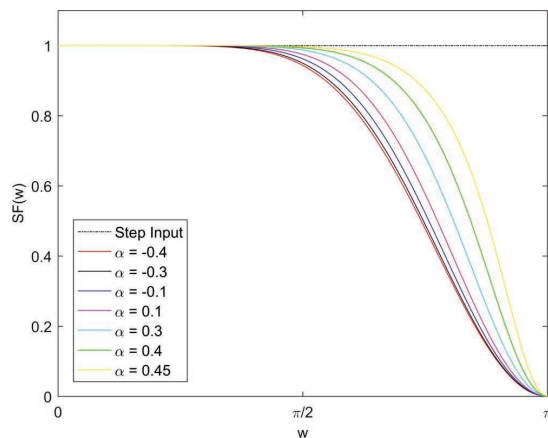


Figure A.5: 10th Order Interior Filter

A.1.4 Spectral Function of the Boundary Filters

For the points near the boundary, the FDL3DI code uses different stencils than in the interior nodes. Near the boundary it uses the following stencil,

$$\alpha_f \hat{\phi}_{i-1} + \hat{\phi}_i + \alpha_f \hat{\phi}_{i+1} = \sum_{n=1}^{n=N+1} a_n \phi_n, \quad (\text{A.10})$$

where N is the order of the filter and is a $N+1$ point stencil. Note here that i is the node number that the filter is based on. For $i = 1$ the $\hat{\phi}_{i-1}$ term is not used. Writing out the summation on the right hand side for $N = 2$,

$$RHS = a_1 \phi_1 + a_2 \phi_2 + a_3 \phi_3,$$

we can see that each ϕ term is shifted from point $i = 1$ by a different amount than the other ϕ terms. ϕ_1 has a $m = (n - i) = (1 - 1)\Delta x = 0$ shift from point $i = 1$, ϕ_2 has a $m = (n - i)\Delta x = (2 - 1)\Delta x = \Delta x$ shift from point $i = 1$ and ϕ_3 has a $m = (n - i)\Delta x = (3 - 1)\Delta x = 2\Delta x$ shift from point $i = 1$. Therefore the shift in ϕ from point i can be written in a form applicable to all ϕ terms in the summation using $(n - i)\Delta x = m\Delta x$. Using $n = i + m$ we can rewrite both sides of the near-boundary stencil equation (A.10) in terms of i ,

$$\alpha_f \hat{\phi}_{i-1} + \hat{\phi}_i + \alpha_f \hat{\phi}_{i+1} = \sum_{i+m=1}^{i+m=N+1} a_{i+m} \phi_{i+m}.$$

Seeing that the left hand side is identical to the interior coefficients case, we can directly write,

$$F_O(w)(1 + 2\alpha_f \cos(w)) = \sum_{i+m=1}^{i+m=N+1} a_{i+m} \phi_{i+m}. \quad (\text{A.11})$$

The Fourier identity relating the shift in the spatial domain to the shift in the frequency domain is repeated below for convenience:

$$F\{f(x_i + m\Delta x)\} = F(w)e^{jwm\Delta x}.$$

We can apply this Fourier identity to the right side of (A.11), where $f(x_i)$ is ϕ_i and for a computational domain, $\Delta x = 1$ to get the following,

$$F_O(w)(1 + 2\alpha_f \cos(w)) = F_I(w) \sum_{i+m=1}^{i+m=N+1} a_{i+m} e^{jwm}. \quad (\text{A.12})$$

Now using Euler's formula below,

$$e^{jwm} = \cos(wm) + j \sin(wm),$$

equation (A.12) becomes,

$$F_O(w)(1 + 2\alpha_f \cos(w)) = F_I(w) \sum_{i+m=1}^{i+m=N+1} a_{i+m} [\cos(mw) + j \sin(mw)].$$

Inserting back in the relation $m = n - i$ the equation above becomes,

$$F_O(w)(1 + 2\alpha_f \cos(w)) = F_I(w) \sum_{n=1}^{n=N+1} a_n [\cos((n-i)w) + j \sin((n-i)w)].$$

Using the previous definition for the spectral function from equation (A.5),

$$SF(w) = \frac{F_O(w)}{F_I(w)},$$

we get,

$$SF(w) = \frac{\sum_{n=1}^{n=N+1} a_n [\cos((n-i)w) + j \sin((n-i)w)]}{1 + 2\alpha_f \cos(w)}. \quad (\text{A.13})$$

A.1.5 Derivation of the Boundary Filter Coefficients

The method for obtaining the near-boundary filter coefficient is very similar to the way the interior filter coefficients were found. For a 2nd order filter ($N = 2$) at point $i = 1$, again we force $SF(\pi) = 0$ to get the following equation,

$$a_0 - a_1 + a_2 = 0. \quad (\text{A.14})$$

It can be shown that you will always arrive at the equation above independent of what node number the filter is based on. Similar to the interior filter, we can again expand ϕ and $\hat{\phi}$ about point "i" using a Taylor series, and then match the Taylor series coefficients of equal order terms on the left and right sides. First expanding ϕ and $\hat{\phi}$ about point $i = 1$ results in,

$$\hat{\phi}_1(1 + \alpha) + \hat{\phi}'_1 \alpha \Delta x + \hat{\phi}''_1 \alpha \frac{\Delta x^2}{2!} = \phi_1(a_1 + a_2 + a_3) + \phi'_1(a_2 + 2a_3)\Delta x + \phi''_1(a_2 + 2^2 a_3) \frac{\Delta x^2}{2!} + O(\Delta x^3).$$

We can achieve 2nd order accuracy by neglecting $\Delta x \geq \Delta x^2$ terms. This results in,

$$\hat{\phi}_1(1 + \alpha) + \hat{\phi}'_1 \alpha \Delta x = \phi_1(a_1 + a_2 + a_3) + \phi'_1(a_2 + 2a_3)\Delta x.$$

Now matching the taylor series coefficients of equal order terms on the left and right hand side, we get the following N additional equations,

$$1 + \alpha_f = a_1 + a_2 + a_3 \quad (\text{A.15})$$

$$\alpha_f = a_2 + 2a_3. \quad (\text{A.16})$$

These N additional equations above as well as equation (A.14) allow a_1, a_2, \dots, a_{N+1} to be solved in terms of the free parameter α_f . For a near-boundary point filter at the first node with 2nd order accuracy, $a_1 = \frac{3}{4} + \frac{\alpha_f}{4}$, $a_2 = \frac{1}{2} + \frac{\alpha_f}{2}$, $a_3 = \frac{\alpha_f}{4} - \frac{1}{4}$. A table including near-boundary point filter coefficients for nodes 1 – 5 at orders of accuracy 1 – 10 can be found in Gaitonde (1998).

A.1.6 Spectral Response of the Near-Boundary Filters

For this discussion, the spectral responses of the near-boundary filter at point $i = 1$ is not shown since the values of ϕ are explicitly specified through the boundary conditions and is not filtered.

The spectral responses of the near-boundary filter at point $i = 2$ is given in Figures A.6 – A.10. In these figures, α_r and α_i corresponds to only the real component and imaginary component, respectively. When interpreting the plots, note that to ensure stability, $\text{Real}(SF) \leq 1$ and $\text{Im}(SF) = 0$ is desirable. Having a $\text{Real}(SF) \leq 1$ means there is no amplification in the input signal. Having

a $Im(SF) = 0$ means that there is no dispersion error. This means that all disturbances, including localized ones, propagate without change of shape. Numerical dispersion often takes the form of so-called 'spurious oscillations'. This is usually depicted using an exact and computed step input. In the computed step input, there will be small oscillations near the step input. These spurious oscillations can cause problems in the CFD simulations. For example, if the step change was in a variable that can only be between 0 and 1, these oscillations can lead to unphysical values.

We can notice some important things about the near-boundary filter at this point. The effect of increasing α and the order of accuracy on the output signal are opposite. As α is increased, the amount of amplification in the real and imaginary components decrease. As the order of accuracy of the filter is increased, the amount of amplification in the input signal is increased. Therefore, as higher order filters are used, a higher value of α is needed to still have a stable output signal. According to the spectral responses for the near-boundary point filter at this node number, to ensure stability of the output a filter of order four with a α value of at least $\alpha \approx 0.4$ is recommended.

The spectral responses of the near-boundary filter at point $i = 3$ is given in Figures A.11 – A.14. Once again, changing α and the order of accuracy have opposite effects. Comparing to the filter at $i = 2$, we see that the filter at $i = 3$ is more stable. This allows a higher order filter to be used. According to the spectral responses for the near-boundary point filter at this node number, to ensure stability of the output a filter of order five or six with a α value of at least $\alpha \approx 0.4$ is recommended. Note that although increasing α past 0.4 will make the filter more accurate, it will also start to reach a point where the input is not attenuated enough and the output becomes unstable. This is why α is interpreted as a tuning parameter that can be optimized for the particular flow field that is being solved.

The spectral responses of the near-boundary filter at point $i = 4$ is given in Figures A.15 – A.16. Looking at the plots, it is clear now that as the filter node moves farther away from the boundary node, the filter becomes more stable and thus, higher order filters can be safely used. Even at low α values of 0.1, there is still no amplification in the output signal. For the filter at node $i = 4$, a filter of order 8 with a α value of at least $\alpha \approx 0.4$ is recommended.

The spectral responses of the near-boundary filter at point $i = 5$ is given in Figures A.17 – A.18. For the filter at node $i = 5$ a filter of order at least 8 with a α value of at least $\alpha \approx 0.4$ is recommended.

In summary, higher values of α causes a more stable output, higher orders of filter accuracy cause a less stable output and as the filter node moves away from the boundary the output is more stable. When choosing the order of accuracy and α value for a certain near-boundary filter, it is recommended that you start with a 0-4-6-8-8 order filter for points 1-2-3-4-5 with a $\alpha \approx 0.4$ and fine tune your filters by increasing/decreasing α and the order of accuracy at each near-boundary point. Note that this is only a general guideline since the spectral functions plotted have been obtained under the implicit assumption that the filter formulas will be applied at each point in the domain. However, in practice they are only applied at a limited number of points.

A.2 Compact Finite Differencing Derivations

A.2.1 Boundary Point Finite Difference Scheme

This section will explain how the coefficients are derived for the implicit compact finite difference formulations at different boundary nodes and of different orders of accuracy. We will first start with the formulations for boundary point 1. The general formula for the second order derivative at boundary point 1 is:

$$\phi_1' = \frac{a\phi_1 + b\phi_2}{\Delta x} - \alpha\phi_2' + O(\Delta x^2). \quad (\text{A.17})$$

Note that the derivative is on both the left and right hand side. This is why it is called *implicit* compact finite differencing. When $\alpha = 0$, it is called *explicit*. Upon inserting Taylor series approximations about point 1, and matching coefficients of equal order terms, a sequence of equations is obtained whose solution yields the coefficients listed in Table 2.2 of [71]. To show this procedure, we will expand the Taylor series about boundary points 2 for both ϕ and ϕ' . This is shown below,

$$b\phi_2 = b(\phi_1 + \Delta x\phi_1' + \frac{\phi_1''\Delta x^2}{2!} + \frac{\phi_1'''\Delta x^3}{3!} + O(\Delta x^4)), \quad (\text{A.18})$$

$$\alpha\phi_2' \Delta x = \alpha(\phi_1' + \Delta x\phi_1'' + \frac{\phi_1''' \Delta x^2}{2!} + \frac{\phi_1'''' \Delta x^3}{3!} + O(\Delta x^4)), \quad (\text{A.19})$$

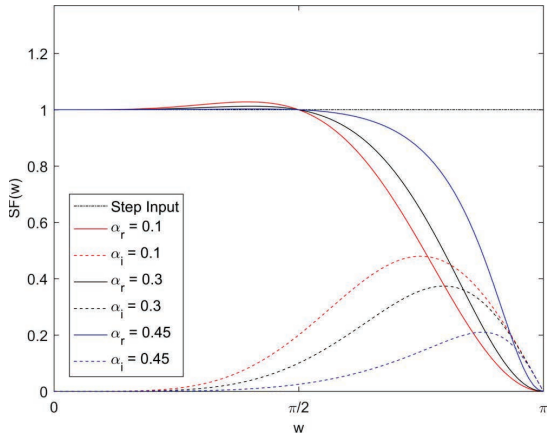


Figure A.6: 4th Order Near-Boundary Filter at Node 2

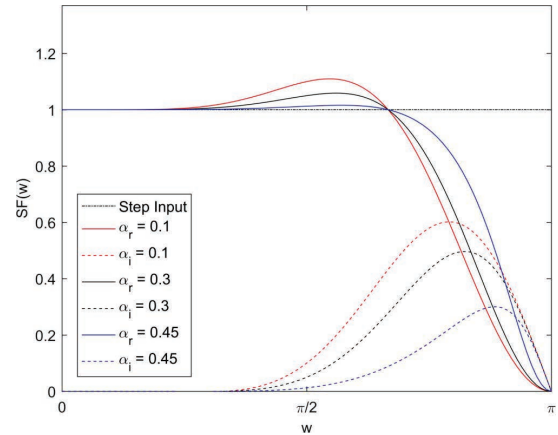


Figure A.7: 5th Order Near-Boundary Filter at Node 2

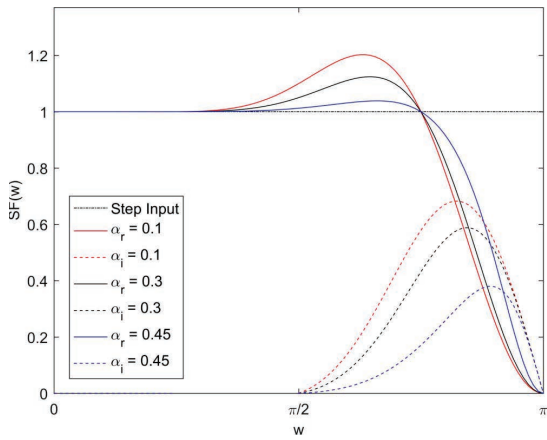


Figure A.8: 6th Order Near-Boundary Filter at Node 2

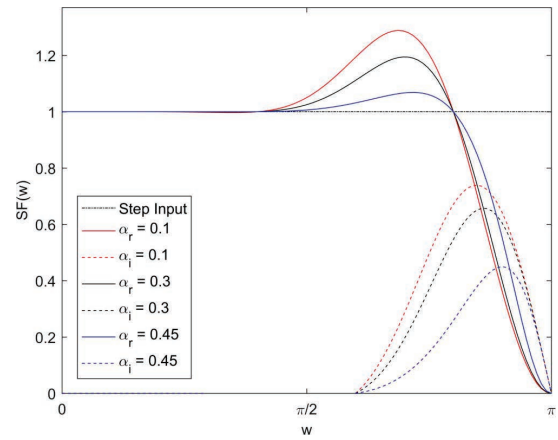


Figure A.9: 7th Order Near-Boundary Filter at Node 2

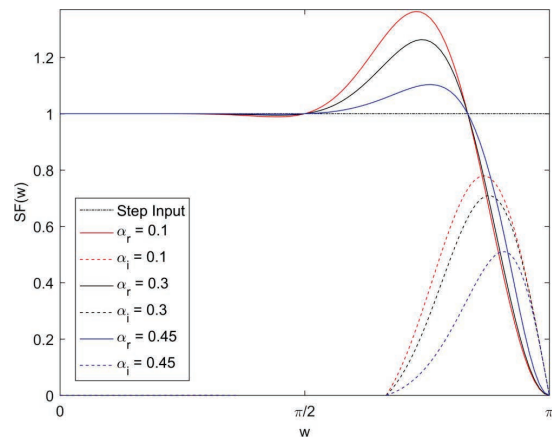


Figure A.10: 8th Order Near-Boundary Filter at Node 2

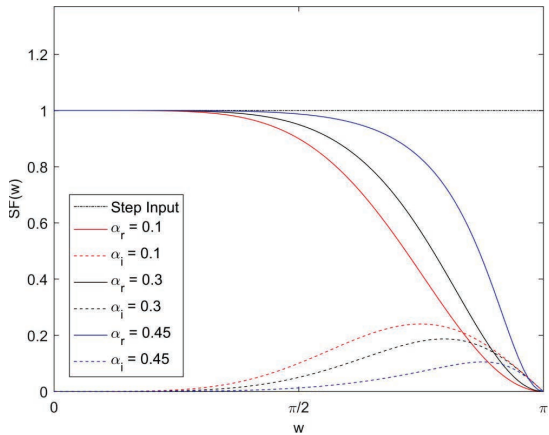


Figure A.11: 5th Order Near-Boundary Filter at Node 3

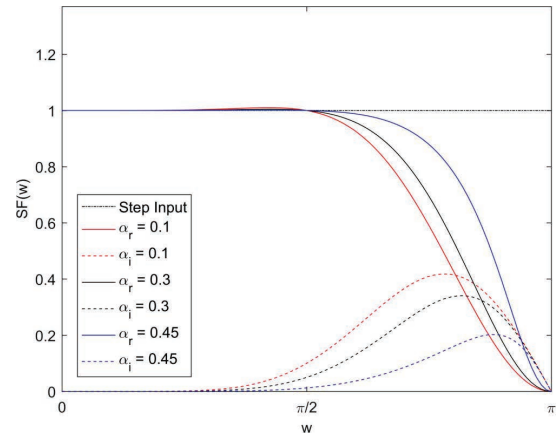


Figure A.12: 6th Order Near-Boundary Filter at Node 3

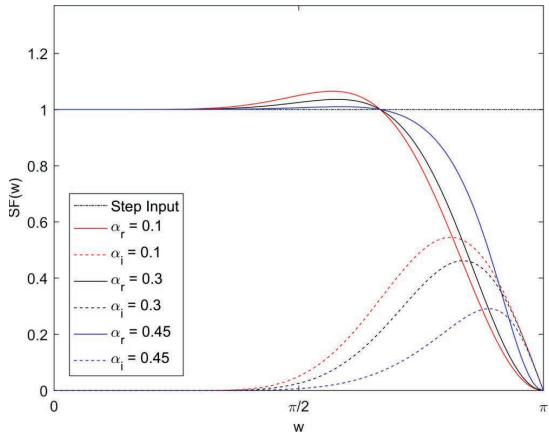


Figure A.13: 7th Order Near-Boundary Filter at Node 3

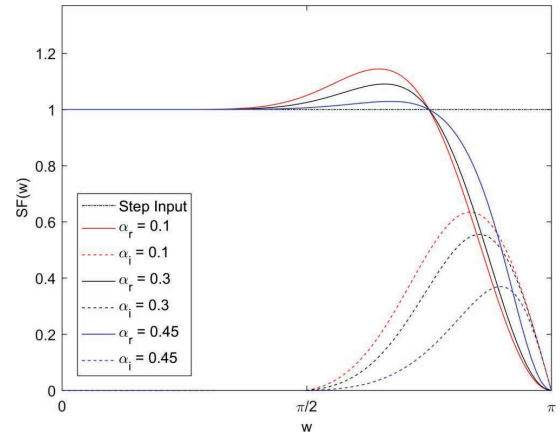


Figure A.14: 8th Order Near-Boundary Filter at Node 3

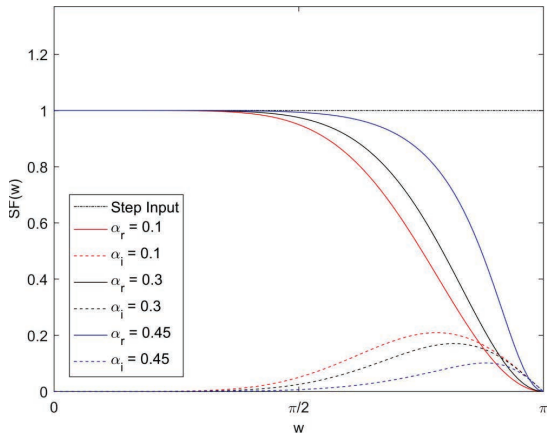


Figure A.15: 7th Order Near-Boundary Filter at Node 4

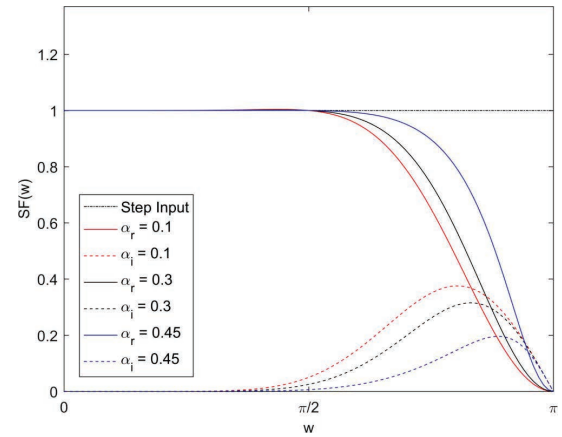


Figure A.16: 8th Order Near-Boundary Filter at Node 4

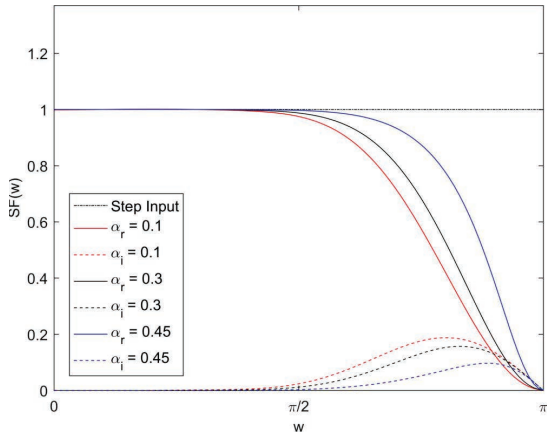


Figure A.17: 9th Order Near-Boundary Filter at Node 5

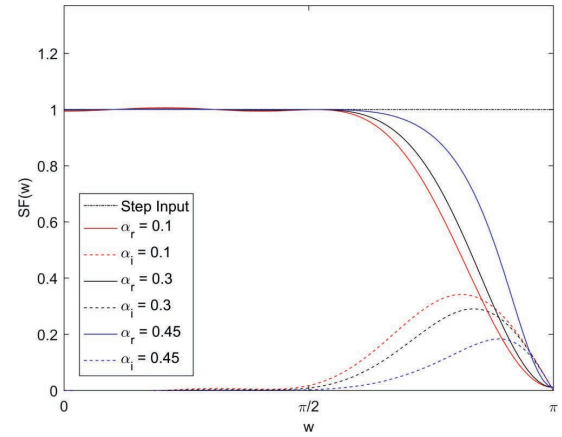


Figure A.18: 10th Order Near-Boundary Filter at Node 5

Using $a\phi_1 + \text{Eq. A.18} - \text{Eq. A.19}$

$$a\phi_1 + b\phi_2 - \alpha\Delta x\phi_2' = \phi_1(a+b) + \Delta x(b-\alpha)\phi' + \frac{\phi_1''\Delta x^2(b-2\alpha)}{2!} + O(\Delta x^3). \quad (\text{A.20})$$

Dividing by Δx ,

$$\frac{a\phi_1 + b\phi_2}{\Delta x} - \alpha\phi_2' = \frac{\phi_1(a+b)}{\Delta x} + \Delta x(b-\alpha)\phi' + \frac{\phi_1''\Delta x(b-2\alpha)}{2!} + O(\Delta x^2). \quad (\text{A.21})$$

To get into form of Eq. A.17,

$$0 + a + b = 0, \quad (\text{A.22})$$

$$-\alpha + 0 + b = 1, \quad (\text{A.23})$$

$$-2\alpha + 0 + b = 0, \quad (\text{A.24})$$

Solving these series of equations arrives at the values for a , b and α .

To arrive at the coefficient for third order accuracy at boundary node 1 a similar procedure is followed where we start at the general derivative formulation below,

$$\phi_1' = \frac{a\phi_1 + b\phi_2 + c\phi_3}{\Delta x} - \alpha\phi_2' + O(\Delta x^3). \quad (\text{A.25})$$

If we expand about node 3 we get,

$$c\phi_3 = c(\phi_1 + 2\Delta x\phi_1' + \frac{2^2\phi_1''\Delta x^2}{2!} + \frac{2^3\phi_1'''\Delta x^3}{3!} + O(\Delta x^4)). \quad (\text{A.26})$$

Using $a\phi_1 + \text{Eq. A.18} + \text{Eq. A.26} - \text{Eq. A.19}$ we arrive at,

$$a\phi_1 + b\phi_2 + c\phi_3 - \alpha\Delta x\phi_2' = \phi_1(a+b+c) + \Delta x(b+2c-\alpha)\phi' + \frac{\phi_1''\Delta x^2(b+2^2c-2\alpha)}{2!} + \frac{\phi_1'''\Delta x^3(b+2^3c-3\alpha)}{3!} + O(\Delta x^4).$$

(A.27)

We need to divide by Δx to get Eq. A.25,

$$\frac{a\phi_1 + b\phi_2 + c\phi_3}{\Delta x} - \alpha\phi'_2 = \frac{\phi_1(a+b+c)}{\Delta x} + (b+2c-\alpha)\phi' + \frac{\phi''\Delta x(b+2^2c-2\alpha)}{2!} + \frac{\phi'''\Delta x^2(b+2^3c-3\alpha)}{3!} + O(\Delta x^3). \quad (\text{A.28})$$

For third order accuracy we neglect the third order terms. To get into form of Eq. A.25 the following constraints must be made,

$$0 + a + b + c = 0, \quad (\text{A.29})$$

$$-\alpha + 0 + b + 2c = 1, \quad (\text{A.30})$$

$$-2\alpha + 0 + b + 4c = 0, \quad (\text{A.31})$$

$$-3\alpha + 0 + b + 8c = 0. \quad (\text{A.32})$$

Solving these series of equations arrives at the values for a , b , c and α . This procedure is followed for orders of accuracy up to 6th order and for boundary points 2, $N-1$ and N . Note that the reason it is called a "compact" finite difference schemes is because it allows us to use the values at one less node than "non-compact" formulations. The result of this is a more efficient algorithm.

A.2.2 Interior Point Finite Difference Scheme

For interior points, a centered formula is employed:

$$\alpha\phi'_{i-1} + \phi'_i + \alpha\phi'_{i+1} = b\frac{\phi_{i+2} - \phi_{i-2}}{4} + a\frac{\phi_{i+1} - \phi_{i-1}}{2}, \quad (\text{A.33})$$

where α , a , and b are constants which determine the spatial properties of the algorithm. By choosing certain coefficients, up to sixth order accuracy can be achieved. Following the same procedure as the previous section where Taylor series approximations are made about point i and inserted in Eq. A.33, the following equations result,

$$-2\alpha + a + b = 1, \quad (\text{A.34})$$

$$-6\alpha + a + 4b = 0, \quad (\text{A.35})$$

$$-10\alpha + a + 16b = 0, \quad (\text{A.36})$$

where only the first equation is solved for second order accuracy, the first and second equations are solved for fourth order accuracy and all three equations are solved for sixth order accuracy. Note that the "compact" finite difference formulation here allows us to use one less node than would be required for a "noncompact" formulation.

APPENDIX B. VERIFICATION OF ACOUSTICS SOLVER

In this appendix, the FW-H solver is verified against computational results for canonical problems. The FDL3DI solver is used to obtain the acoustic radiation field for point monopole, dipole, and quadrupole sources in a moving medium. Single-frequency, harmonic sources are considered. The acoustic sources are specified using a vector source term $\mathbf{S} = \{0, 0, 0, 0, S_5\}$, which is added to the governing equations. The sources are centered at the origin and defined for monopole, dipole and quadrupole respectively as:

$$S_5(x, y, t) = \exp\left(-\ln(2) \frac{(x)^2 + (y)^2}{b^2}\right) \sin(\omega t) f(t),$$

$$\begin{aligned} S_5(x, y, t) = & \exp\left(-\ln(2) \frac{(x - x_c)^2 + (y)^2}{b^2}\right) \sin(\omega t) f(t) + \\ & \exp\left(-\ln(2) \frac{(x + x_c)^2 + (y)^2}{b^2}\right) \sin(\omega t + \pi) f(t), \end{aligned}$$

$$\begin{aligned} S_5(x, y, t) = & \exp\left(-\ln(2) \frac{(x - x_c)^2 + (y - y_c)^2}{b^2}\right) \sin(\omega t) f(t) + \\ & \exp\left(-\ln(2) \frac{(x - x_c)^2 + (y + y_c)^2}{b^2}\right) \sin(\omega t + \pi) f(t) + \\ & \exp\left(-\ln(2) \frac{(x + x_c)^2 + (y + y_c)^2}{b^2}\right) \sin(\omega t) f(t) + \\ & \exp\left(-\ln(2) \frac{(x + x_c)^2 + (y - y_c)^2}{b^2}\right) \sin(\omega t + \pi) f(t), \end{aligned}$$

where,

$$f(t) = \min\left(1.0, \left(\frac{t}{t_0}\right)^3\right), \quad (\text{B.1})$$

and x_c and y_c are the center of the poles, ω is the angular frequency of the harmonic source, b is the scaling parameter, t_0 is the ramp parameter, and $f(t)$ is the function used to ramp the source at

the beginning of the simulation. For the simulations, the following parameters are used: $x_c = y_c = 0.01$, $b = 0.2$, $\omega = 10\pi$, $t_0 = 3$. The distance between the poles ($2x_c$) is equal to 1% of the acoustic wavelength to ensure source compactness.

The mesh used for the simulation, shown in Fig. B.1, is a structured 2-D grid extending from $-100 \leq \{x, y\} \leq 100$. The red inner circle in the figure is the “porous” surface that was used to predict the far field power spectral density (PSD) located at the blue outer circle. The radius of the “porous” surface is made large enough that the predicted value no longer changes as the radius is increased. The far field location is chosen so that it is at least 10 acoustic wavelengths away from the source. The domain is chosen large enough so that the outer boundaries do not influence the pressure fluctuations at the far field location. At the center of the sources the minimum mesh spacing is $\Delta x = \Delta y = 0.01$. The mesh is stretched with a hyperbolic tangent distribution that has a maximum mesh spacing rate of change of 0.6% at the outer boundaries. This slow growth rate is chosen to minimize any numerical dissipation at the acoustic far field location.

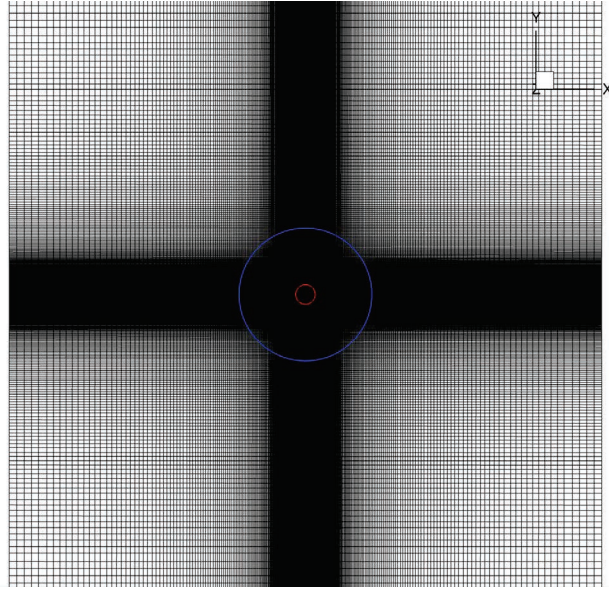


Figure B.1: Structured grid used for validation of the FW-H solver; every 4th grid line is shown for clarity. The red inner circle is the FW-H integration surface; noise is predicted at the observer locations shown with the blue outer circle.

Since the FDL3DI solution for this case is 2-D due to the 2-D grid used, and the FW-H code is three dimensional (solves the convected wave equation in 3-D), the following approach is used to

essentially predict noise from a source that is effectively infinite along the axis (z) not simulated. For any given (x, y) source location and observer azimuth angle, noise is predicted at additional observer locations in the z direction and summed up in the frequency domain until additional observer locations no longer change the solution. This process is explained with the schematic in Fig. B.2. Note that complex pressures are added during this summation to account for interference effects. This approach is equivalent to replicating sources along the z direction (simulating an infinitely long line source) and predicting noise at the original observer locations. The 3-D FW-H solution processed in this manner can then be directly compared with the 2-D FDL3DI solution.

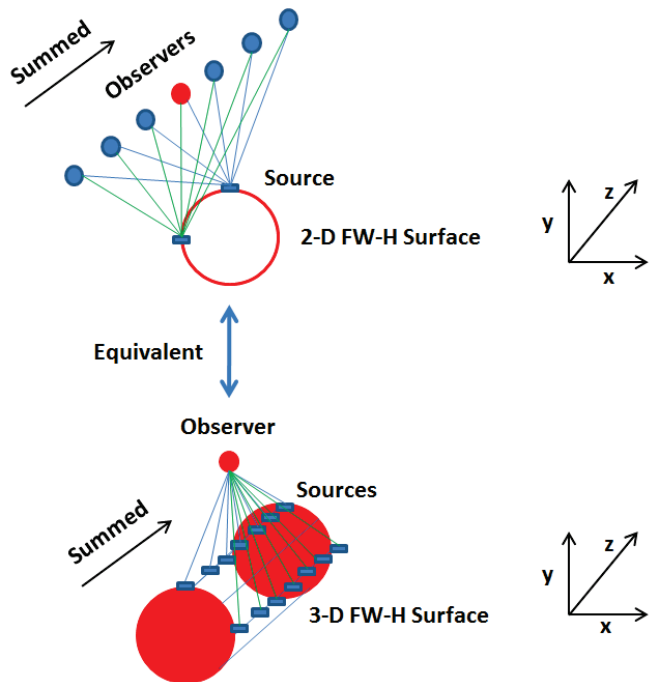


Figure B.2: The process by which the 3-D FW-H solver is used on the 2-D grid.

Figure B.3 shows the instantaneous dilatation fields for the monopole, dipole and quadrupole sources. The comparison of the predicted far field PSD from the FW-H solver to the actual PSD values in the far field is shown in Fig. B.4. All polar plots are shown at the frequency of the harmonic source. From the plots, we can see excellent agreement of the predicted and actual PSD values for all three sources. From the plots, we can also see that the convective amplitude is well captured by the FW-H solver.

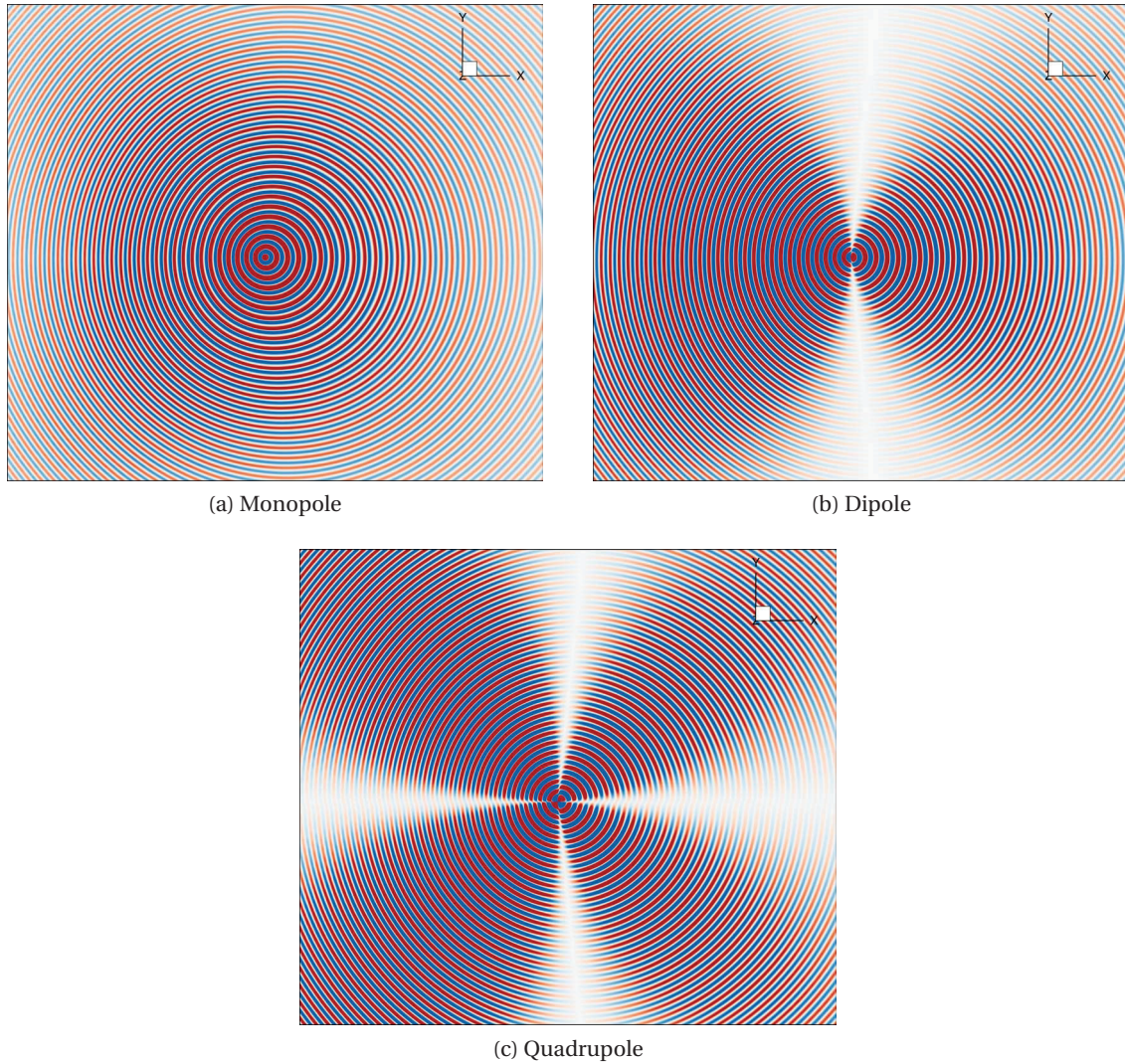


Figure B.3: Dilatation fields for the monopole, dipole and quadrupole sources that are used for verification of the FW-H solver.

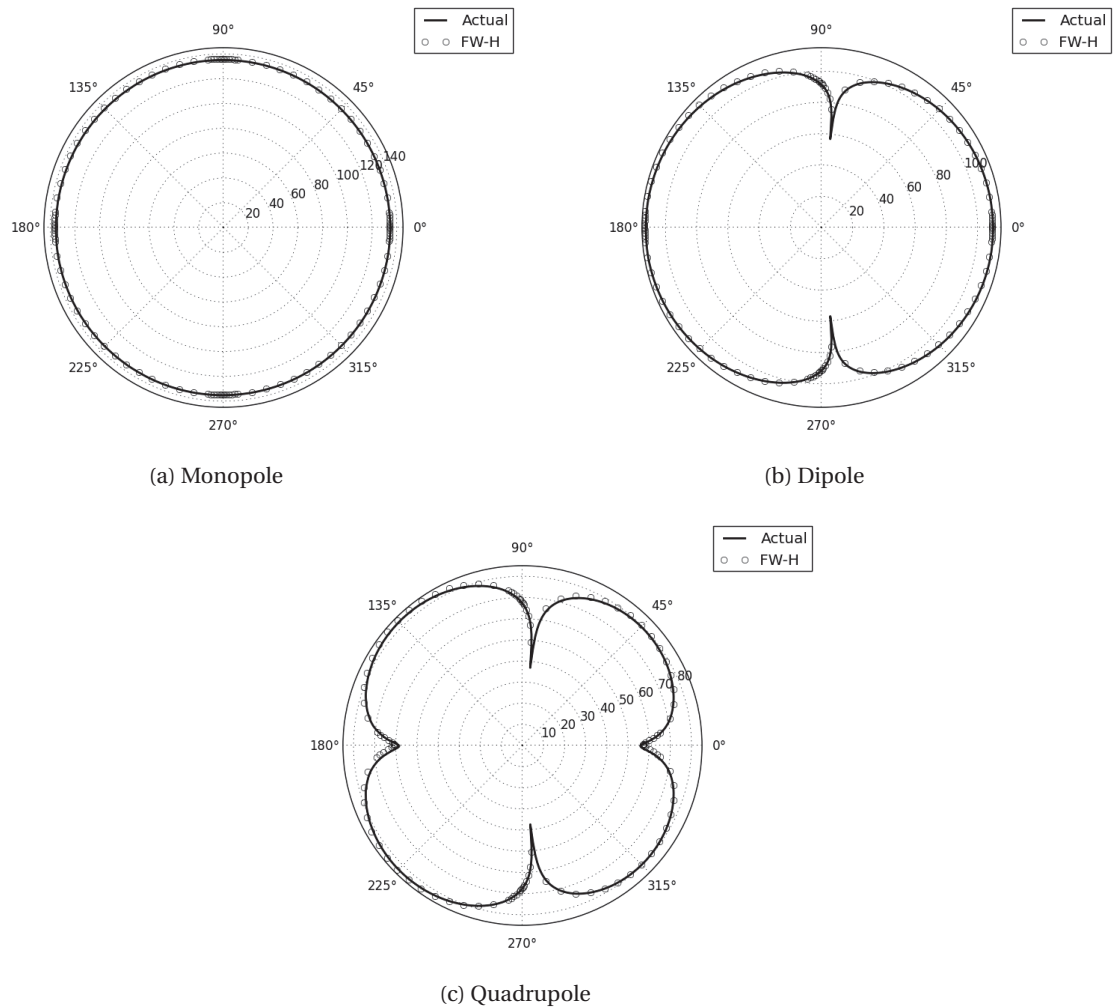


Figure B.4: Directivity comparisons of PSD for a point source radiating in a moving medium between the FDL3DI predicted value (solid black lines) in the far field and the FW-H predicted value (open circles). All polar plots are shown at the frequency of the harmonic source.

APPENDIX C. FILTERING ALGORITHM NEAR FENCE BOUDNARIES

The FDL3DI code uses a low pass filter to dissipate the energy in the sub-grid scales. Generally, as the order of the filter increases, less energy is dissipated. If the grid used does not resolve the scales of the small eddies and the energy in the eddies is not dissipated, this can lead to numerical instabilities in the solution. In the simulations, a central filter is used at boundary nodes 3, 4 and 5. To achieve higher accuracy at boundary node 2 (higher than what the 2nd order central filter would give), a one-sided filter is used at boundary node 2. An illustration of the filters used at the boundaries and their corresponding stencils is shown in Fig. C.1.

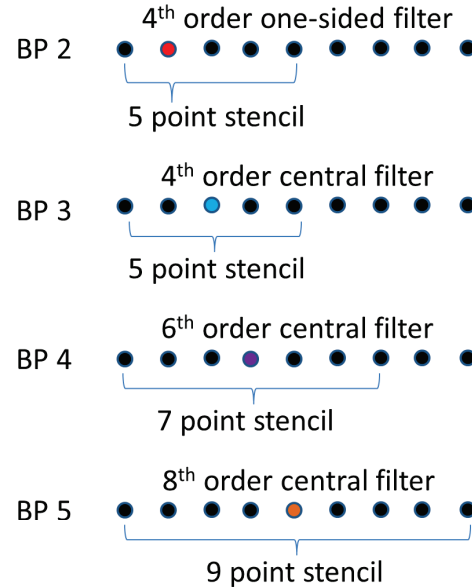


Figure C.1: Filters used at boundary points (BP) 2-5

The FDL3DI code is not designed to have interior boundaries that are adjacent to hole points. The code assumes that the solution in nodes adjacent to hole points are updated through interpolation from another grid. Because of this, it does not apply the filters correctly at the fence bound-

aries that are adjacent to holes. This section will explain how the filter was corrected near the fence boundaries so that consistent filters were used near the airfoil and fence boundaries.

Figure C.2 shows a $\hat{e}_\eta \times \hat{e}_\zeta$ slice taken at an arbitrary location along the fence height. All nodes along this slice are interior nodes before holes are accounted for, and have 8th order central filters applied (see Fig. C.3). To model the fences, as shown in Fig. C.4, points that are inside the fence are blanked out and not solved by FDL3DI. The adjacent nodes to these holes are assigned a no-slip boundary condition. Illustrated in Fig. C.5, the FDL3DI filtering routine applies boundary filters at the nodes before and after the holes in all directions. This implementation leaves 8th order filters near the corners of the fences as shown by the red boxes in Fig. C.6. Because of this, very little energy is dissipated in these regions and numerical instabilities occur. The code was modified so that the boundary filters were applied to the corners of the fences as shown in Fig. C.7.

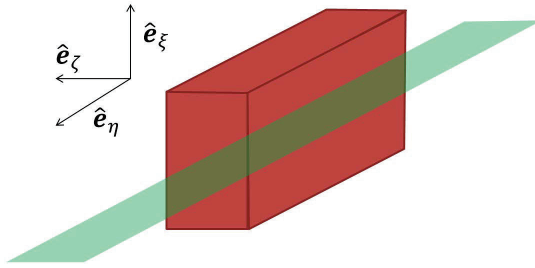


Figure C.2: $\hat{e}_\eta \times \hat{e}_\zeta$ slice taken at an arbitrary location along the fence height.

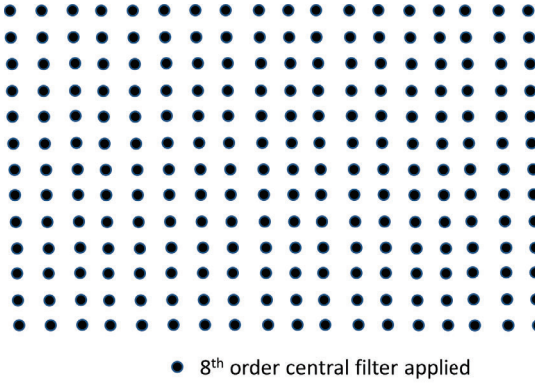


Figure C.3: The points where the fences are located are first treated as interior points and are assigned 8th order central filters.

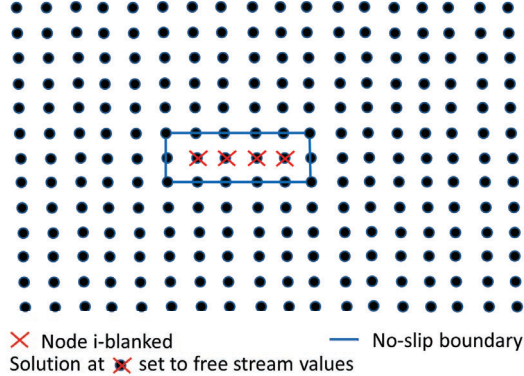


Figure C.4: I-blanking and boundary condition procedure for modeling fences

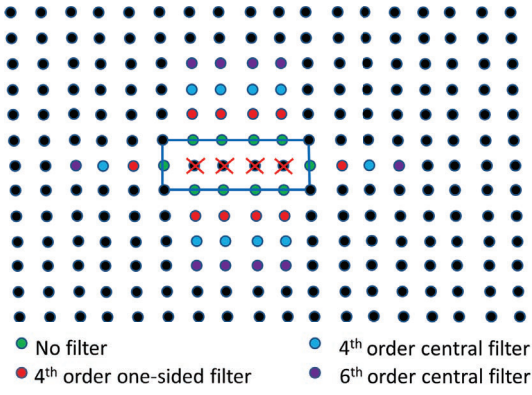


Figure C.5: The plot shows how the solutions are filtered near the holes in the original FDL3DI code. The solution is given a boundary filter before and after the start of the holes in all directions.

A $\hat{e}_\eta \times \hat{e}_\zeta$ slice taken at the top of a fence step is shown in Fig. C.8. At this plane, there are no holes so no boundary filters are applied in the \hat{e}_η and \hat{e}_ζ directions. This leads to very large instabilities around the edges of the fence due to the 8th order central filters applied around the edges of the fence, as shown with the red boxes in Fig. C.9. The FDL3DI code was modified so that the boundary filters are correctly applied around the fence edges as shown in Fig. C.10.

This methodology is used to correct the boundary filters near the fence walls in the $\hat{e}_\xi \times \hat{e}_\zeta$ and $\hat{e}_\xi \times \hat{e}_\eta$ planes as well. By making these code modifications, the boundary filters applied near the fence walls is the same as the filters applied near the airfoil surface.

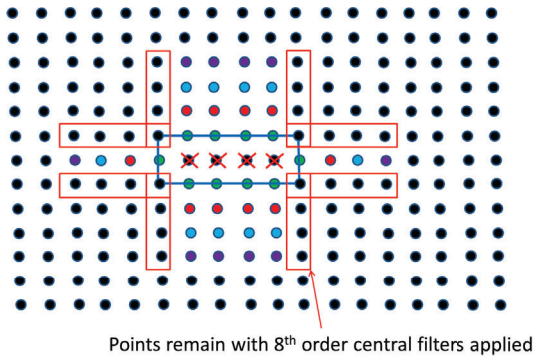


Figure C.6: The figure shows the problem that arises with the original FDL3DI code at planes throughout the fence height. The filter is not applied correctly near the corners of the fence, which leads to instabilities.

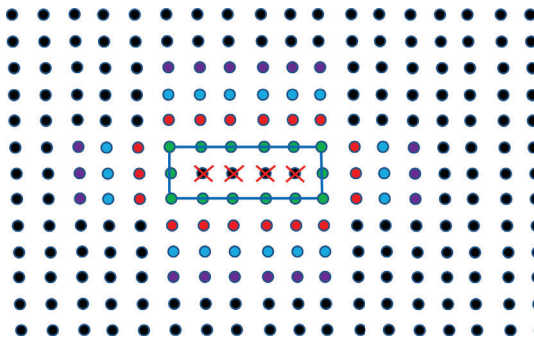


Figure C.7: Filter implementation corrected for planes throughout the height of the fences.

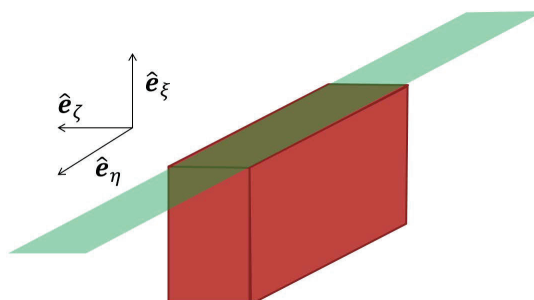


Figure C.8: $\hat{e}_\eta \times \hat{e}_\zeta$ slice taken at the top of a fence step.

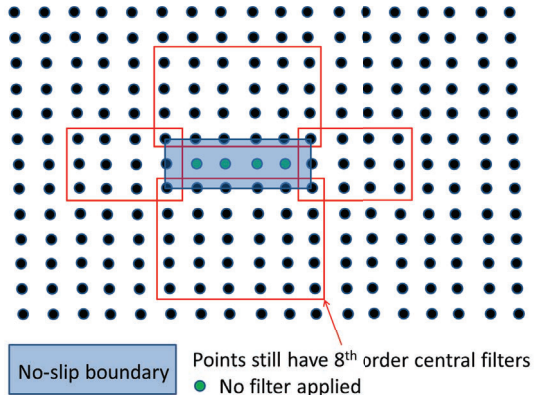


Figure C.9: The figure shows the problem that arises with the original FDL3DI code at planes at the top of a fence step. The filter is not applied correctly near all four walls, which leads to large instabilities.

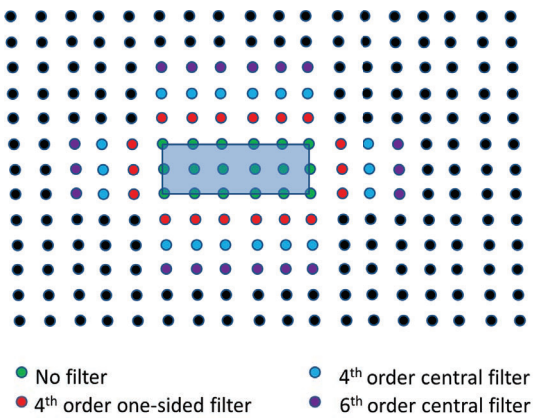


Figure C.10: Filter implementation corrected for planes at the top of a fence step.